THE INFLUENCE OF PROCESS PARAMETERS ON MECHANICAL PROPERTIES AND CORROSION BEHAVIOR OF FRICTION STIR WELDED ALUMINUM JOINTS

Sara BOCCHI[1], Marina CABRINI[2], Gianluca D'URSO[1], Claudio GIARDINI[1], Sergio LORENZI[2], Tommaso PASTORE[2]

[1]University of Bergamo - Department of Management, Information and Production Engineering, Dalmine (BG), Italy, sara.bocchi@unibg.it, gianluca.d-urso@unibg.it, claudio.giardini@unibg.it

[2]University of Bergamo - Department of Engineering and Applied Science, Dalmine (BG) Italy, INSTM, CSGI, marina.cabrini@unibg.it, sergio.lorenzi@unibg.it, tommaso.pastore@unibg.it

Abstract

Aim of the present paper is to analyze if and how the process parameters (namely rotational speed S and feed rate f) affect both the mechanical properties and the corrosion behavior of friction stir welded (FSWed) butt joints made of AA7075 and AA2024 alloys and their combination. Tensile tests were performed orthogonally to the welding direction on specimens having the welding nugget placed in the middle of gage length. Rockwell tests were carried out on each specimen moving from the joint axis until the hardness of the base material was reached. A clear dependence of the Ultimate Tensile Strength (UTS) from the process parameters were observed when the joints are obtained using the same material while the effect is not so evident when two different materials are concerned. In almost all cases, the best conditions, in terms of mechanical resistance, were obtained for intermediate values of rotational speed and feed rate. Further tests were performed for evaluating the corrosion behavior and the stress corrosion cracking susceptibility of FSWed joints. In particular, local corrosion potential measurements were executed and longtime immersion tests were carried on four points bending specimens loaded up to 80% of the Yield Strength (TYS), in 35g/L sodium chloride solution. The same tests were replicated on unloaded specimens. The potential trends are always well defined and much higher for the AA2024 alloy, since it is more noble than the AA7075 alloy. Mixed welding allows to identify the AA7075 alloy as an anode part, having a lower copper concentration and a high concentration of zinc. A correlation of some corrosion behaviors to the mechanical characteristics was evidenced, in particular for the AA2024 alloy.

Keywords

Friction Stir Welding; Mechanical properties; Corrosion behavior; AA2024-T3 alloy; AA7075-T6 alloy.

1. Introduction

Friction Stir Welding (FSW) technology, patented by TWI in 1991 [1,2] has been successfully used to join different aluminum alloys (e.g. 2024-T3 [3], 6082 AA-T651 [4]) and other materials that are difficult to be welded, such as Ti-alloys [5] and Mg-alloys [6] but also advanced high-strength steel [7] and metal-matrix

composites [8]. The technique is now widely used in naval [9], aerospace [10], automotive and railway applications [11]. The rotation of the tool and the movement along the joint axis cause an increase in temperature because of friction between tool and workpiece and within the stirred material [12]. In such conditions, the plasticization of the material occurs due to the combination of the mixing effect of the tool pin and the pressure applied by the tool shoulder, that cause the formation of a solid bonded region [13,14]. This technology permits the solid-state welding in several configurations and also the joining of dissimilar alloys [15]. The FSW technology has a large interest especially for high resistance aluminum alloys (e.g. 2000 and 7000 aluminum alloys series, because of their aeronautical use), which are difficult to be joined with traditional techniques because of the microstructure alteration during age hardening. The high plastic flow and the heat generated by FSW may result in remarkable local microstructural modifications and local changes of material characteristics [16].

When considering the behavior of Friction Stir Welded joints, it is normal practice to focus the attention on the mechanical characteristics of the welds through the execution of tensile tests and the analysis of the hardness distributions inside the joined materials. For these reasons, it is very important to understand the effects of process parameters and process setup on the weld quality. Several Authors studied these aspects with particular attention to the quality of FSW joints in terms of mechanical properties (UTS, fatigue resistance etc.) [17-19]. For example, in [20] the Authors evidenced how some very important issues related to the mechanical properties of aluminum friction stir welded joints are process parameters such as feed rate, rotational speed, tool geometry and pin axis inclination. Tool rotational speed was considered as one of the most important process variable: high rotational speeds may raise the strain rate, so affecting the re-crystallization process. Moreover, some authors showed how high welding speeds are related to low heat inputs, which gives rise to faster cooling rates of the joint. This can reduce the extent of metallurgical transformations taking place during welding (such as solubilization, re-precipitation and coarsening of precipitates) and hence the local strength of individual regions across the weld zone. Based on these considerations, the ratio between the tool feed rate and the rotating speed can be considered as a relevant parameter in determining the mechanical strength of the joints [21]. In [22] empirical relationships were developed to predict the tensile strengths of friction stir welded AA1100, AA2219-T87, AA2024-T3, AA6061-T6, AA7039-T4 and AA7075-T6 aluminum alloy joints. Other authors found that there is an optimal tool rotational speed range and that too low or too high speeds correspond to a low quality of the joints [23], demonstrating that these parameters can be optimized for obtaining sound parts.

On the other hand, these local microstructural modifications and local changes of material characteristics may affect the corrosion behavior [24]. Several literature works pointed out the corrosion behavior of FSW joints [25-29], but the effects on stress corrosion cracking are not yet completely understood. In addition, particular attention has to be paid to the well-known susceptibility of the copper-aluminum and zinc-aluminum alloys to stress corrosion cracking. Despite the enhanced properties, the added elements introduce higher degree of heterogeneity due to the presence of secondary phases or termed constituent particles [30]. Corrosion behavior can be mainly affected by the presence – size and distribution – of such phases, modifying the anodic and cathodic behavior of the zones of joining [27,31,32]. Several works describing corrosion morphologies that can occur also concomitantly in form of localized corrosion, e.g., galvanic corrosion, pitting, dealloying or intergranular attack [28] were found, but very few data regarding the combination of different alloys and the systematic correlation between mechanical properties and corrosion behavior can be noticed. Under such considerations, the corrosion behavior can be significantly influenced by welding parameters and a strict correlation between them and alloy macro and microstructure has to be further investigated [25].

Aim of this study is to analyze how the process parameters affect both the mechanical properties and the corrosion behavior of butt joints obtained on different aluminum alloys by FSW. The experimental study was performed by the friction stir welding of sheets made of two different commercial aluminum alloys, namely

AA2024-T3 and AA7075-T6; the combination among these materials was also considered. Tensile tests were performed orthogonally to the welding direction on specimens having the welding nugget placed in the middle of gage length. Rockwell tests were carried out on each specimen moving from the joint axis to the base material. Four-point bending tests (4PBB) at 80% TYS were performed in aerated 0.6 M NaCl solution for about 1400 hours. Free corrosion potential measurements were carried out on both loaded and unloaded specimens for comparison. Corrosion morphology was observed by means of optical and Scanning Electron Microscope (SEM) equipped with Energy Dispersive Spectroscopy (EDS). Data are discussed as a function of the welding parameters.

2. Experimental procedure

2.1 Characteristics of the base materials

The chemical composition and the mechanical properties of the AA2024-T3 alloy are reported in Table 1. The alloy is a commercial product, provided solubilized and then naturally aged. The alloy shown α-Al grains oriented along the rolling direction (mean grain size 100 μm). As well known, the matrix contains homogeneous coherent precipitates, denoted as GPB zones that are not visible at the optical microscope and at the SEM. Several intermetallic macro-precipitates are present. The EDS analysis evidenced coarse round shaped S-phase (Al_2CuMg) particles (Figure 1) and irregularly shaped Al-Cu-Fe-Mn particles (Figure 2).

Table 1: Chemical composition (%w) and mechanical properties of the AA2024-T3 alloy.

Cu	Mg	Si	Fe	Mn	Zn	Ti	Yield Strength (MPa)	UTS base material (MPa)	Elongation %
4.4	1.6	0.08	0.10	0.48	0.1	0.04	345	459	17

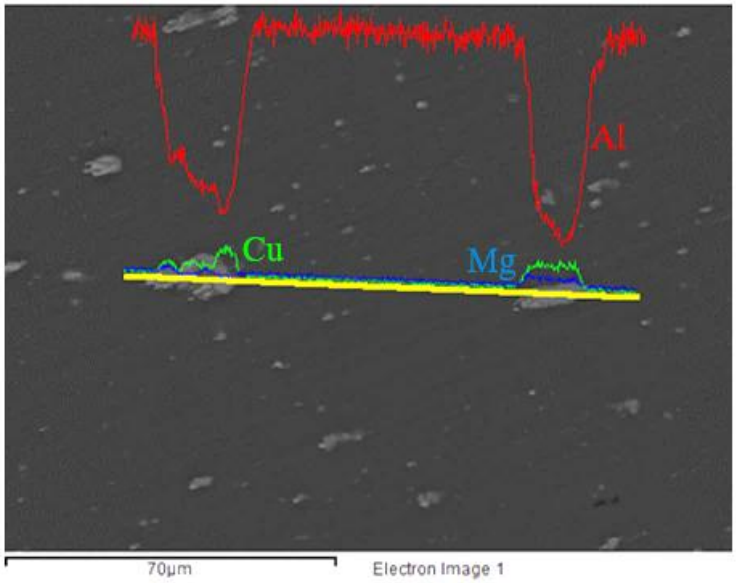

Figure 1: EDS maps of the AA2024-T3 base alloy Al_2CuMg intermetallic precipitates.

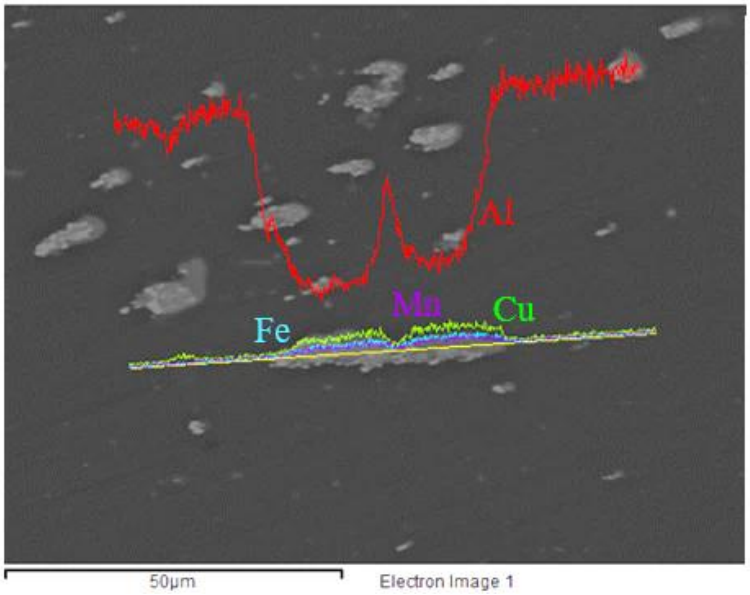

Figure 2: EDS maps of the AA2024-T3 base alloy Al-Cu-Fe-Mn intermetallic precipitates.

The chemical composition and mechanical properties of the AA7075-T6 alloy are reported in Table 2. The alloy, provided solubilized and artificially aged, presents α-Al grains oriented along the rolling direction; the strengthening particles have $MgZn_2$ composition (η-phase) and size in the nanometer range, then not visible thorough optical and SEM analysis. Several macro-precipitates of intermetallic phases are present. The EDS analysis evidenced elongated shaped Al_7Cu_2Fe particles and coarse round shaped $MgZn_2$ and MgSi particles (Figure 3).

Table 2: Chemical composition (%w) and mechanical properties of the AA7075-T6 alloy.

Zn	Mg	Cu	Fe	Mn	Si	Cr	Ti	Yield StrengthYS (MPa)	UTS base material (MPa)	Elongation %
5.9	2.7	1.5	0.12	0.02	0.06	0.19	0.05	511	578	11

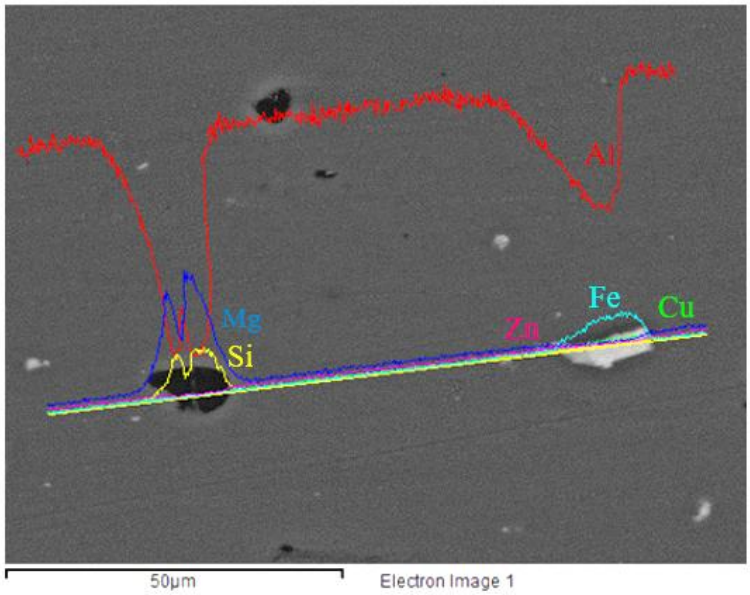

Figure 3: EDS maps of the AA7075-T6 base alloy intermetallic precipitates.

2.2 FSW experimental set up

FSW joints were carried out on sheets having a thickness equal to 4 mm by means of a CNC machine tool. Sheets of 200 x 80 mm were welded by using tools with smooth plane shoulder (16 mm diameter) and a frustum of cone pin shape (pin maximum and minimum diameters equal to 6 and 4 mm, pin height equal to 3.8 mm). Three different series of weldings were performed: AA2024-AA2024 joints, AA7075-AA7075 joints and mixed joints AA2024-AA7075 (figure 4). The tests were carried out (based on a general full factorial 3^2 design) using three different rotational speeds (S=1000, 1500 and 2000 rpm) and feed rates (f=10, 35 and 60 mm/min) considering all the combinations of these parameters. Three repetitions were performed for each combination for evaluating the process repeatability.

Figure 4: Weld sample.

2.3 Mechanical testing of the joints

The mechanical properties of the joints were evaluated by means of tensile tests executed orthogonally to the welding direction, according to UNI EN ISO 6892-1:2016. The specimens, having the welding nugget placed in the middle of gage length, were tested using a testing machine Galdabini with a load cell of 50 kN. The tests were carried out under speed control (7.6 mm/min) and a pre-load equal to 0.5 kN. The joint tensile resistance was evaluated as a function of the different process parameters. The influence of process parameters on both the material structure and the joint strain hardening was evaluated by measuring the hardness distribution in the welded sections for all the tested conditions. A hardness tests map (HRb) was carried out on the top side of the joint region through a grid of indentations (3 lines of indentations, 5 mm spaced). On each line, the tests were executed moving from the joint axis to the base material.

2.4 Corrosion Potential profile measure

The specimens were polished by emery papers up to 1000 grit, degreased in acetone in ultrasonic bath for 5 minutes and then stored in still air for 48 hours to allow the formation of the natural protective film. Free corrosion potential measurements were carried out by moving a 1 mm capillary equipped with a Standard Calomel Electrode (SCE) over the specimen length every 10 mm (figure 5). Before the measurements, the specimens were pre-soaked for 48 hours in distilled water to achieve stable potential values. The potential profile was measured on the top of the joint, in the central zone of the specimen, to avoid border effects. The specimens were covered by a thin layer of distilled water to permit the execution of the potential measurements.

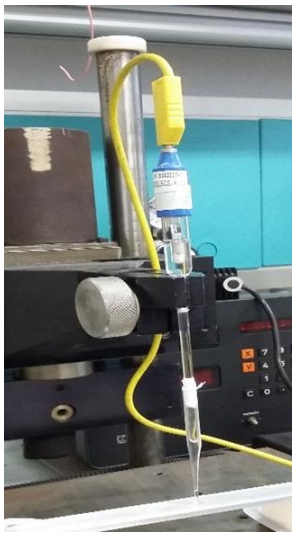

Figure 5:Corrosion tests device.

2.5 Longtime immersion tests

Four-point bending tests were performed according to ASTM G39. The specimens were loaded up to the 80% of the tensile strength of FSW joints, reached during tensile tests. The specimens were positioned into a bending device to attain uniform tensile strain distribution across the weld. Four glass cylinders were used to avoid galvanic coupling between the stainless-steel holder and the aluminum specimen (figure 6-a). The specimens were exposed in a cell filled with about 30L of water with 35 g/L sodium chloride for more than 1400 hours (figure 6-b). The same procedure was followed for unloaded specimens, obtained in the same welding conditions.

a)  b) 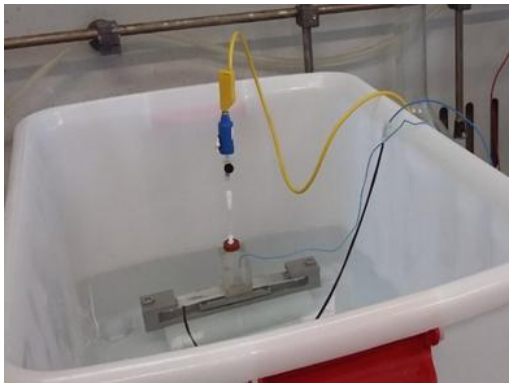

Figure 6:a) Load cell system; b) Longtime immersion tests set-up.

2.6 Fractographic analysis

After the exposure, all the specimens (loaded and unloaded) were rinsed in distilled water and degreased with acetone in ultrasonic bath. The surfaces were observed by means of an optical microscope and a scanning electron microscope (SEM) equipped with energy dispersive x-ray analysis (EDS). Metallographic sections were also taken by cutting the specimens along longitudinal direction.

3. Results and discussion

3.1 Mechanical properties

The average UTS data, their standard deviations and elongation [%], calculated for all the alloys and for all the tested conditions, are reported in Table 3.

Table 3: Average UTS data and standard deviations of all the tested conditions.

AA2024-AA2024					AA7075-AA7075					AA2024-AA7075				
S [rpm]	**f***	**UTS [MPa]**	**St. Dev.**	**E %**	**S [rpm]**	**f***	**UTS [MPa]**	**St. Dev.**	**E %**	**S [rpm]**	**f***	**UTS [MPa]**	**St. Dev.**	**E %**
1000	10	307.7	10.4	9.4	1000	10	378.3	8.8	14.0	1000	10	311.4	7.1	10.1
1000	35	325.8	33.4	5.3	1000	35	434.7	15.9	2.2	1000	35	345.2	12.4	4.0
1000	60	229.0	27.6	3.5	1000	60	322.1	28.8	4.0	1000	60	301.0	10.3	6.4
1500	10	317.0	3.0	10.7	1500	10	360.8	14.6	15.4	1500	10	271.3	20.0	10.8
1500	35	358.0	24.3	8.3	1500	35	426.0	10.6	7.6	1500	35	318.5	27.9	7.5
1500	60	304.9	4.5	4.1	1500	60	272.8	15.7	4.9	1500	60	282.5	34.0	4.7
2000	10	320.0	15.1	10.3	2000	10	296.4	13.3	13.2	2000	10	184.3	8.5	4.9
2000	35	142.3	18.3	2.8	2000	35	309.8	29.2	6.7	2000	35	195.1	10.7	5.8
2000	60	123.5	13.7	2.7	2000	60	133.5	28.8	2.4	2000	60	150.2	4.7	3.1

* f [mm/min]

A general full factorial 3^2 ANOVA analysis was carried out on the recorded UTS data. Table 4 reports the F-values and the P-values about the effects of speed, feed and their combination. In general, a factor was considered to have a relevant influence if its P value is lower than the cut off limit (in this case set equal to 0.05). A clear dependence of the UTS from the process parameters can be observed when the joints are obtained using the same material while the effect is not evident when the two different materials are concerned.

Table 4: ANOVA results.

	UTS AA2024-AA2024		UTS AA7075-AA7075		UTS AA2024-AA7075	
	F	**P**	**F**	**P**	**F**	**P**
speed	28.05	0.000	5.02	0.019	2.92	0.080
Feed	22.05	0.000	6.21	0.009	0.30	0.747
speed * feed	10.76	0.000	2.63	0.069	2.96	0.048

Figure 7 shows the contour plots of the UTS in all the tested conditions, expressed as a function of feed rate [mm/min] and rotational speed [rpm]. As a general remark, it is possible to observe that the best conditions in terms of UTS are always obtained for intermediate values of rotational speed and feed rate, except for the AA2024-AA7075 that shows the best properties for low values of speed. A decrease of the mechanical properties can be noticed moving towards the limits of the technological window. The failure of the joints after tensile tests usually occurred in TMAZ, for both homogenous and mixed joints. Moreover, the failure occurred in correspondence of the region having the lower hardness (see also paragraph 3.3).

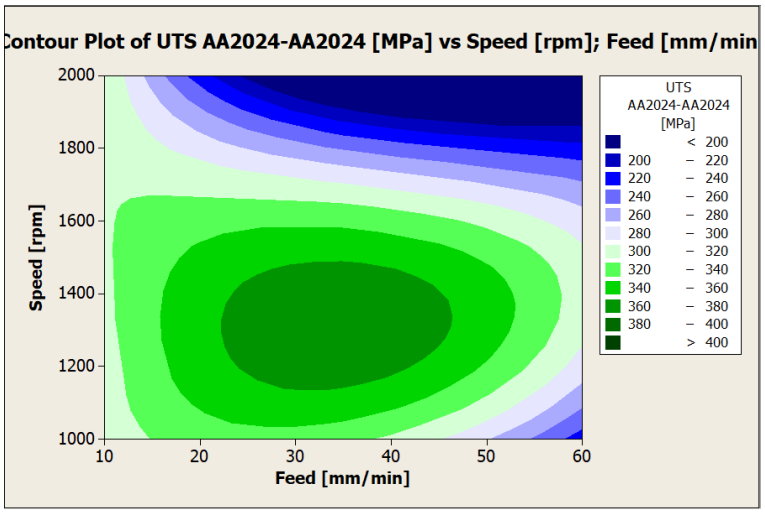

(a)

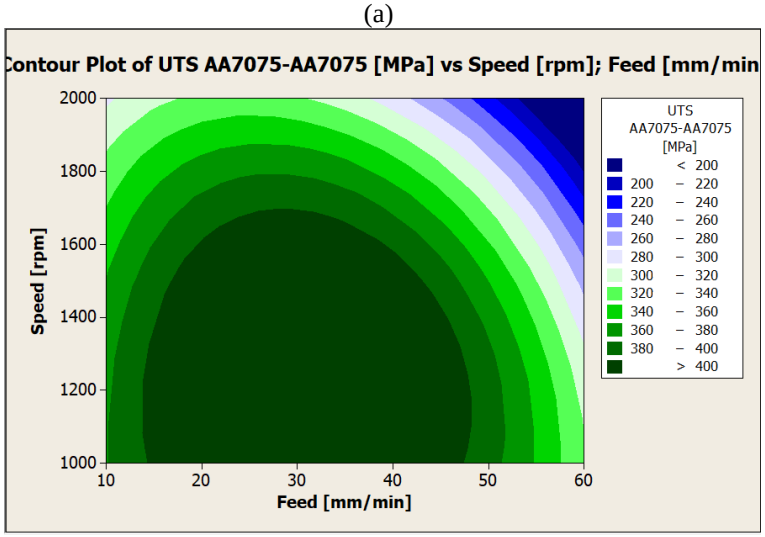

(b)

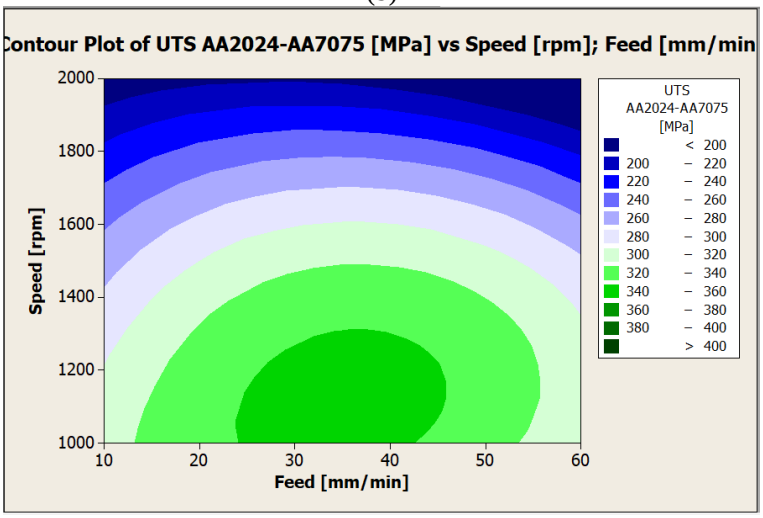

(c)

Figure 7: Tensile strength of the joints (UTS) as a function of feed rate [mm/min]and rotational speed [rpm], (a) AA2024-AA2024 (b) AA7075-AA7075 (c) AA2024-AA7075.

3.2 Microstructure of the welding

As demonstrated by the UTS data, the joints resistance for high values of feed (60 mm/min) and speed (2000 rpm) resulted to be lower with respect to the other welding conditions. In these conditions some defects were also observed in the joints section. Therefore, microstructural analysis and corrosion tests were executed only for the joints obtained using speed equal to 1000-1500 rpm and feed equal to 10-35 mm/min.

The common FSW structure was evidenced in all the considered conditions: the central zone, called "nugget" in which the fully recrystallization takes place, the Thermo-Mechanically Affected Zone (TMAZ) and the Heat Affected Zone (HAZ). No significant microstructural differences were noticed between the microstructure of the advancing and retreating side. Moreover, within the range of the adopted welding parameters, no significant differences about the width of the different zones can be observed.

For both the alloys, fine recrystallized grains (mean grain size 3-5 μm in AA2024-AA2024 joints and 5-7 μm in AA7075-AA7075 joints) were detected in the nugget, surrounded by small precipitates of secondary phases (Figure 8 and Figure 9).

AA2024-AA2024 S=1000 rpm; f=35 mm/min

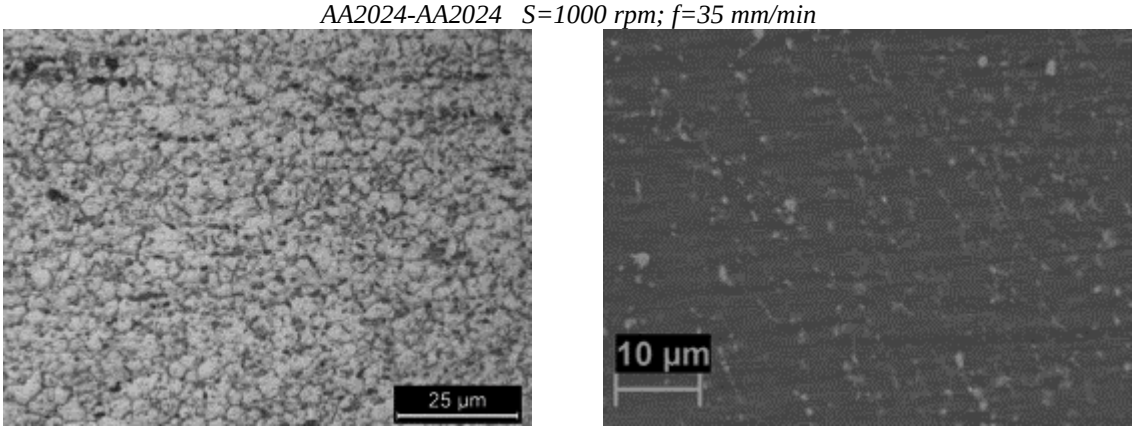

AA2024-AA2024 S=1500 rpm; F=10 mm/min

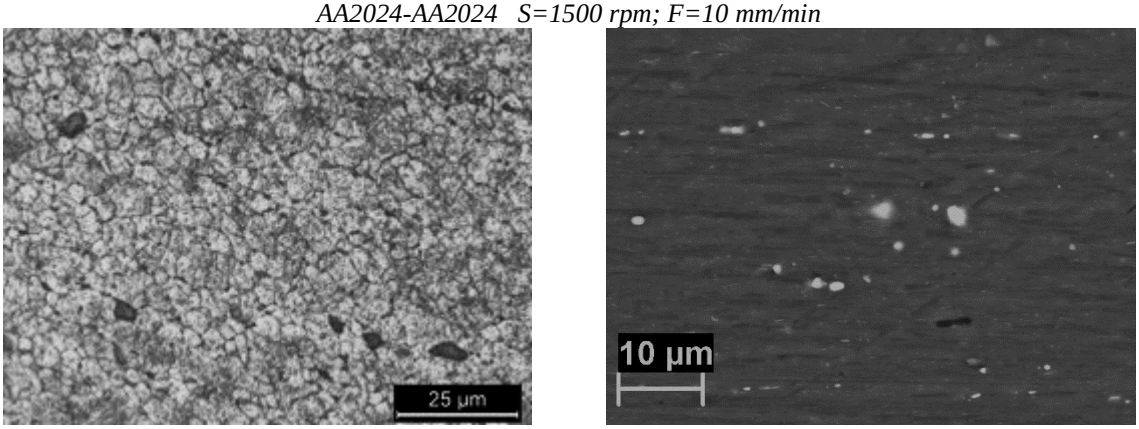

a) *b)*

Figure 8: Microstructure of the nugget of the AA2024-AA2024 joints welded using different parameters: a) optical images, b) SEM close up of the precipitates.

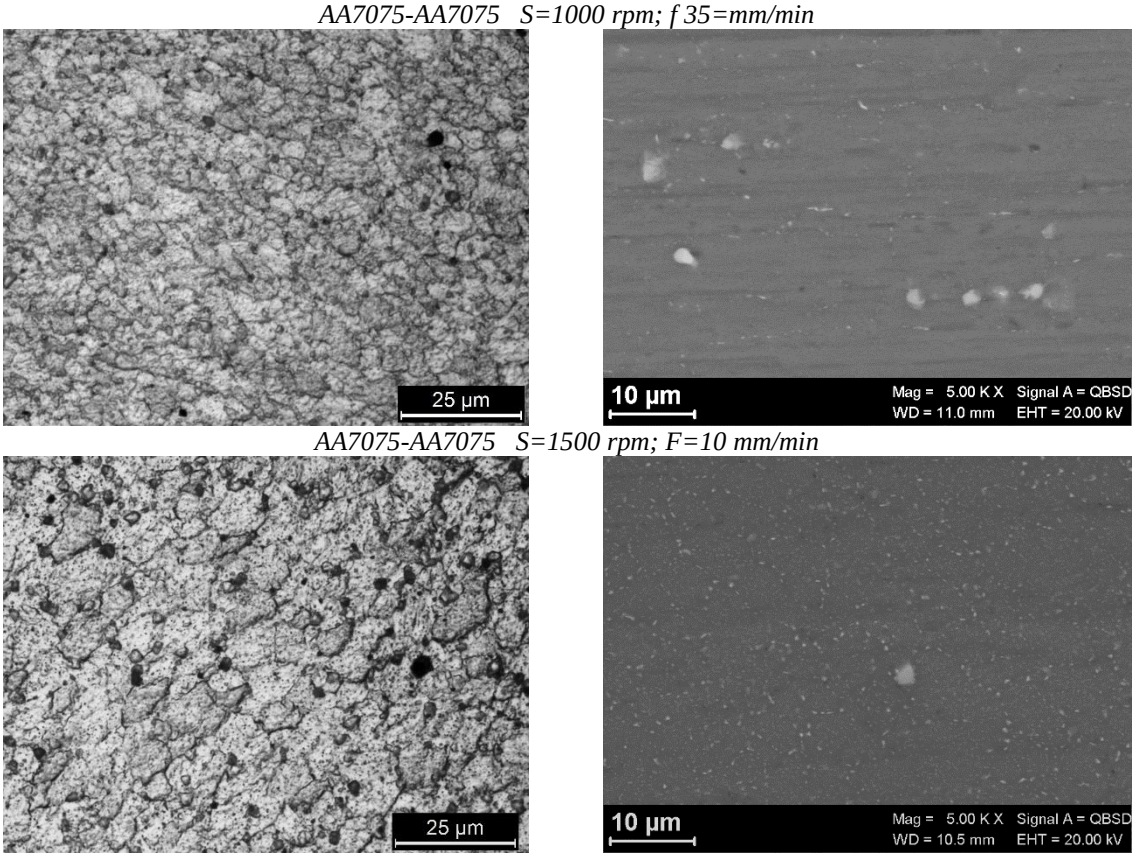

Figure 9: Microstructure of the nugget of the AA7075-AA7075 joints welded using different parameters: a) optical images, b) SEM close up of the precipitates.

Jariyaboon et al [25] and J.J. Pang et al. [33] reported that the precipitates particles of the 2024-T3 alloy are S-phase. The increase in thermal input does not affect the grain size in the nugget. However, the number of secondary phases decreases and their dimension increases [34-35]. A decrease of the number of precipitates at grain boundaries was observed increasing the rotational speed from 1000 to 1500 rpm, whereas the feed rate resulted not to have influence on the precipitates.

Severe plastic deformation was noticed in the zones between the nugget and TMAZ. The microstructure in the HAZ shows elongated grains similar to the base material and also the micrometric precipitates in these zones are similar to the base metal. The TMAZ and HAZ have similar microstructures characterized by elongated grains and several precipitates, with a mean grain size of 100 µm, comparable with the original grains dimensions. For both the alloys, shape and dimension are not altered by the welding parameters; Figure 10 and Figure 11 show an example for the two alloys.

AA2024-AA2024 S=1000 rpm; F=35 mm/min

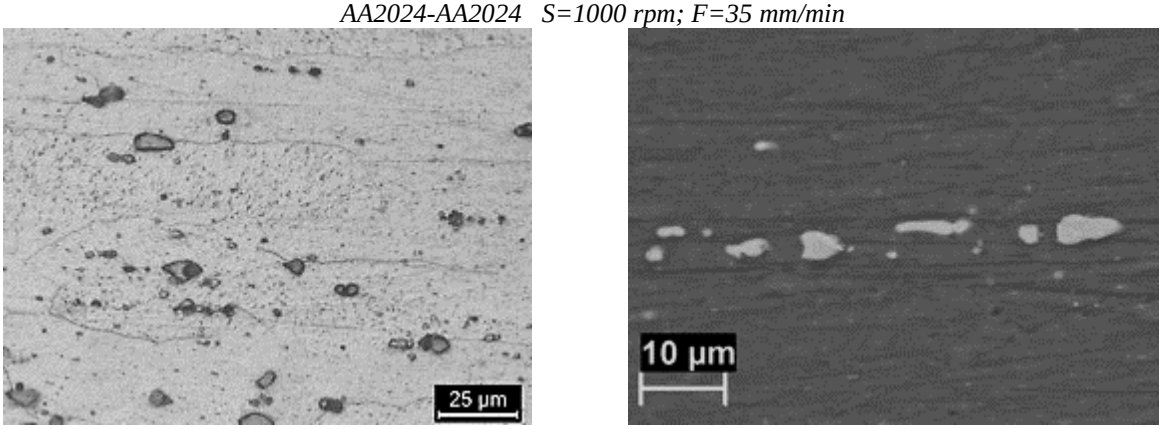

a) *b)*

Figure 10: Microstructure of the HAZ of the AA2024-AA2024 joints welded using different parameters; a) optical images, b) SEM close up of the precipitates phases.

AA7075-AA7075 S=1000 rpm; F=35 mm/min

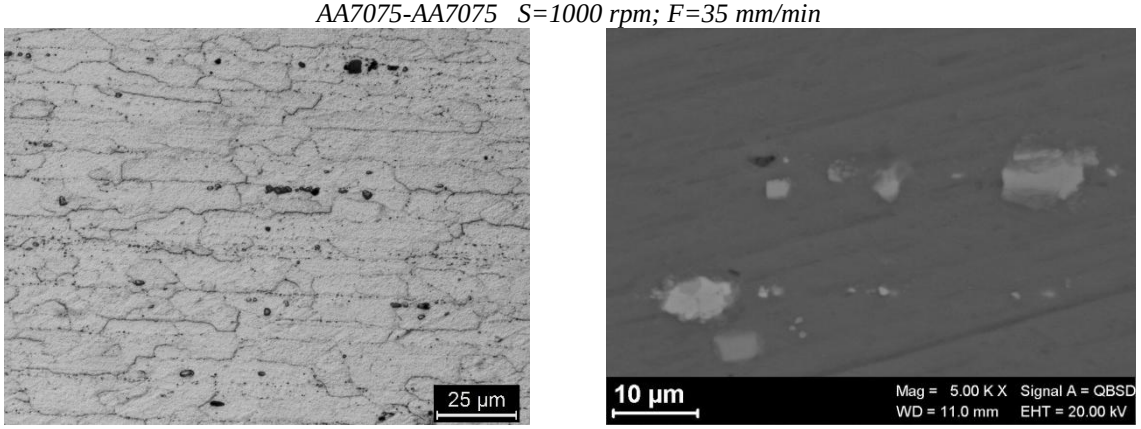

a) *b)*

Figure 11: Microstructure of the HAZ of the AA7075-AA7075 joints welded using different parameters; a) optical images, b) SEM close up of the precipitates phases.

As far as mixed welds are concerned, the welding process generates a microstructural variation for both the alloys. As in the cases previously studied, the thermal input generated by the pin, coupled with the strong plastic deformation, leads to a fine grain structure in the nugget, with a mean size of about 3 µm. Figure 12 shows a clear demarcation between the two alloys in correspondence of the junction where the precipitation of a continuous line of second phases can be observed.

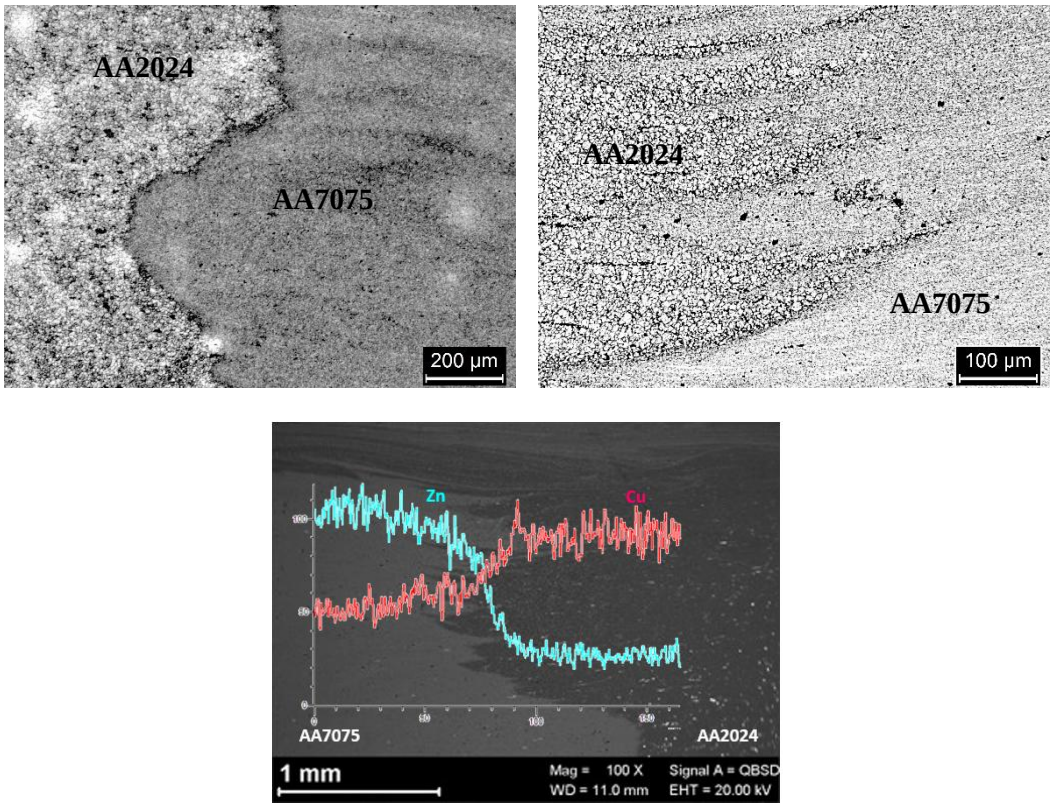

Figure 72: Microstructure and EDS analysis of the AA7075-AA2024 welded joint, S=1000 rpm; f=35 mm/min.

3.3 Hardness tests

Figures 13, 14 and 15 show the hardness as a function of the distance from the joint axis. Three profiles of indentations, 5 mm spaced, were executed on the top surface of the specimens. For each profile, the indentations were executed at a distance of 2.5 mm (until a distance of 20 mm from the joint axis). On each line, the tests were executed moving from the joint axis to the base material.

A symmetry is observed with respect to the center of the weld. No significant differences between advancing and retreating zone were noticed. The weld has lower hardness compared to base material. In all cases, the lowest hardness was found in the TMAZ for low values of feed rate per unit revolution (feed/speed [mm/rev]), which is an index of the thermal power transferred to the joint region during the process. In general, the softening occurred in the TMAZ is greater in the conditions that provide higher heat input. Nevertheless, no systemic effects between joint hardness and process parameters were found. A peak of hardness is observed in the HAZ of the AA2024 joints, ascribable to high density of fine intragranular precipitates.

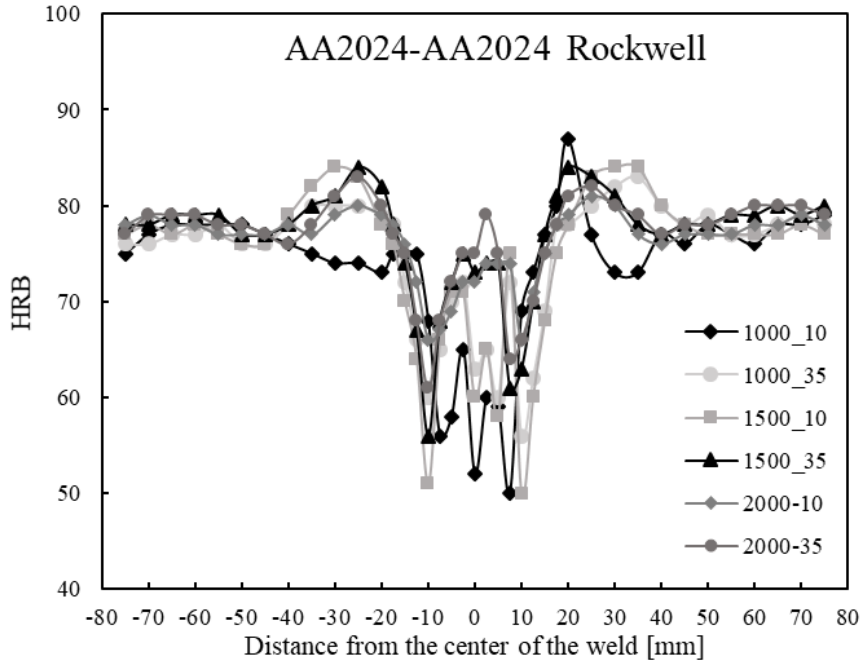

Figure 13: Hardness profile of the FSW AA2024-AA2024 joints as a function of different welding parameters.

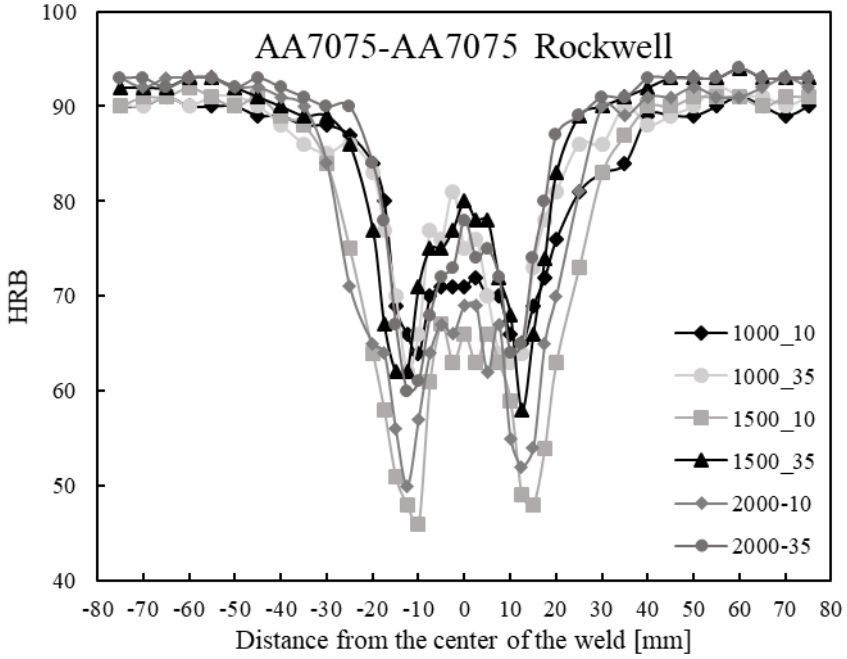

Figure 14: Hardness profile of the FSW AA7075-AA7075 joints as a function of different welding parameters.

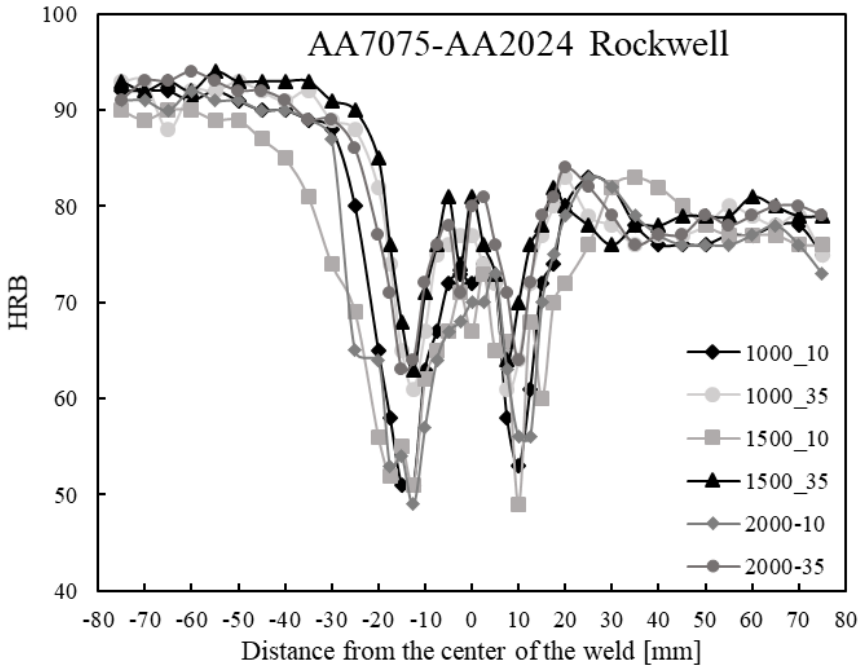

Figure 15: Hardness profile of the FSW AA7075-AA2024 joints as a function of different welding parameters.

The hardness profile is due to the microstructural modifications and to the distribution of precipitates owing to the thermo-mechanical action. The micrometric precipitates do not strongly influence the hardness of the alloy because the main effect on hardness is due to the presence of sub-micrometric precipitates in the GPB (Guinier Preston Bagaryatsky) zones.

In both cases the alloys were heat treated to solubilize the second phases and then naturally (AA2024) or artificially (AA7075) aged. The matrix of the AA2024 joints contains homogeneous coherent precipitates, denoted as GPB zones, as well as fine precipitates (S-phase). In the base material, the high value of microhardness is related to the high density of coherent GPB zones. Dissolution and coarsening of strengthening precipitates as well as the formation of wide precipitate-free zones take place in the weld region. In the HAZ, close to the base material, the decrease of hardness is attributed to the dissolution of GPB zones. In the center of the HAZ, the hardness is ascribable to high density of fine intragranular precipitates. In the nugget zone, the hardness is mainly determined by the balance between small grain size and high density of GPB zones; coarsening of S-phase precipitates can be noticed.

In the AA7075 alloy, the dynamic recrystallization in the nugget produces a re-dissolution of the precipitates obtained by the artificially ageing treatment, while these precipitates are coarsening in the HAZ, reducing the hardness. Similar to the AA2024 alloys, the reduction of grain size increases the hardness up to intermediate values between base material and HAZ. The mixed joints showed a hardness profile similar than the ones realized with the same alloy.

3.4 Corrosion potential

The measurement of the free corrosion potentials along the FSW joints, together with the hardness distributions, are reported in Figures 16-27 for AA2024, AA7075 and mixed joints. The images of the loaded and un-loaded specimens after 1400 hours of exposure in NaCl 0.6M are reported in the same figures.

The AA2024-2024 FSWed alloys (Figure 16-19) show the minimum of hardness in the center of the nugget whilst the AA7075-AA7075 (Figure 20-23) FSWed alloys show two well defined softened areas in the thermo-mechanically affected zone. The mixed joints (Figure 24-27), far from the nugget, show the same behaviors of the two different base alloys welded using the same parameters. Free corrosion potential of mixed joints is minimum in the zone of AA7075 base metal and it increases moving across the nugget to values typical of the AA2024 base metal. Such behavior is due to the metal partial mixing in the joint and to the precipitates distribution.

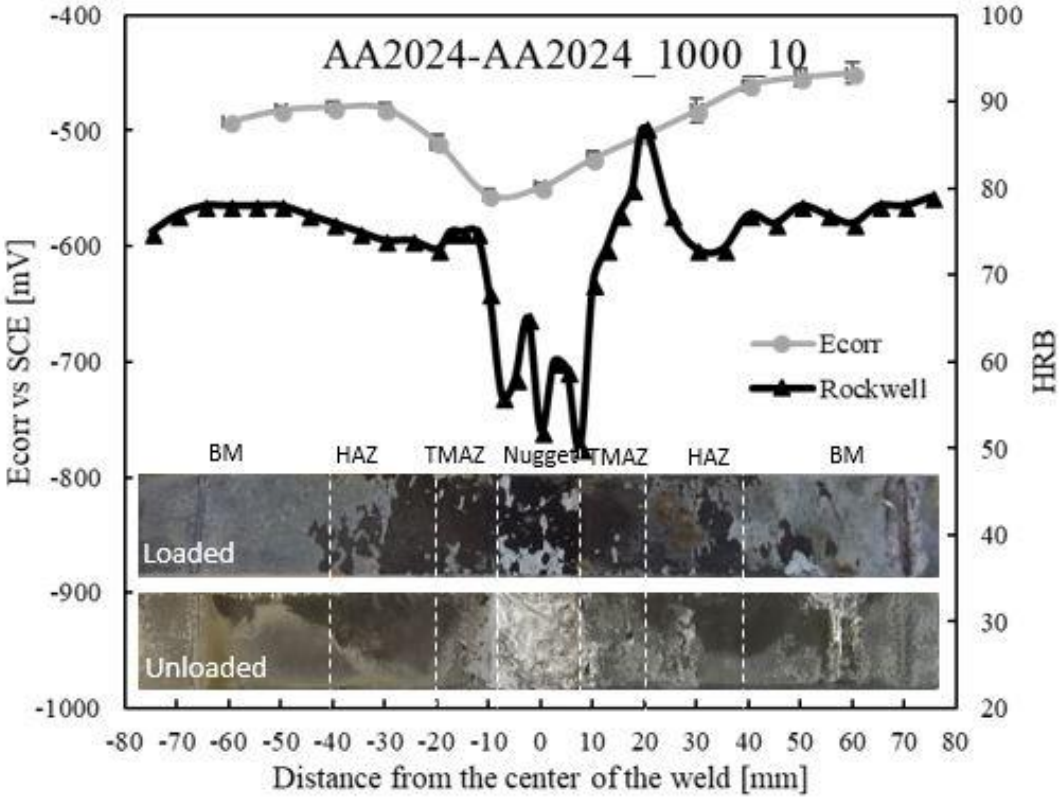

Figure 16: Profile of local corrosion potential for the AA2024-AA2024 unloaded specimen welded with speed=1000 rpm and feed=10 mm/min.

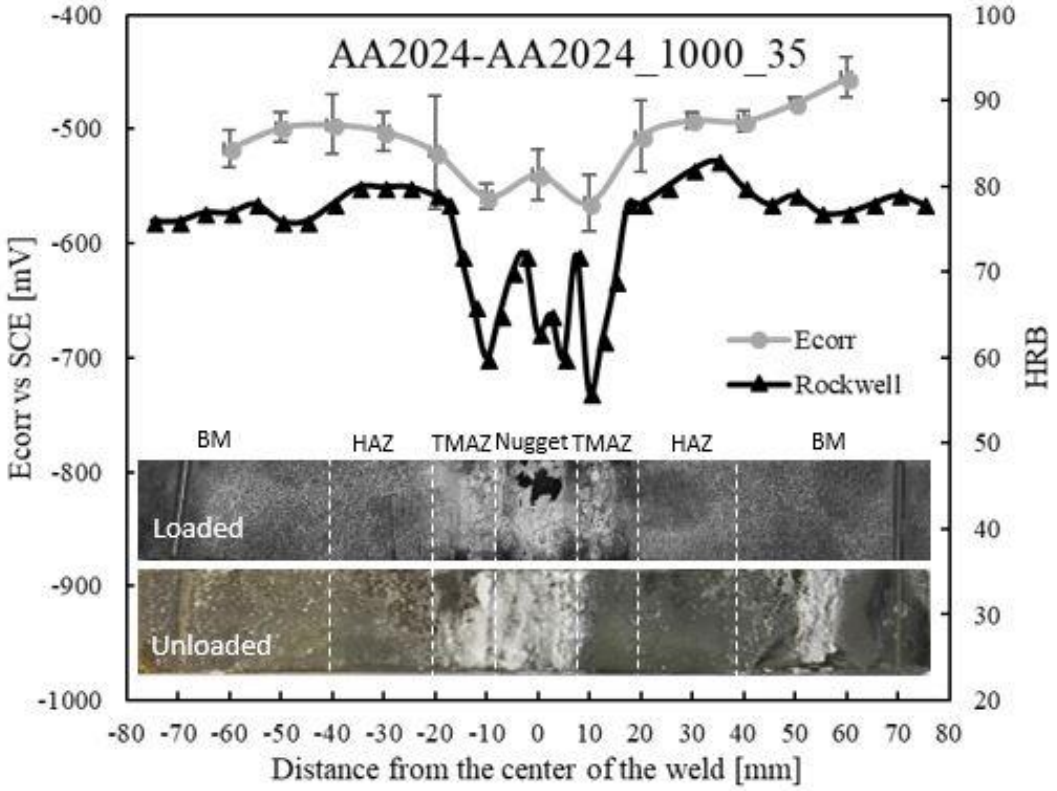

Figure 87: Profile of local corrosion potential for the AA2024-AA2024 unloaded specimen welded with speed=1000 rpm and feed=35 mm/min.

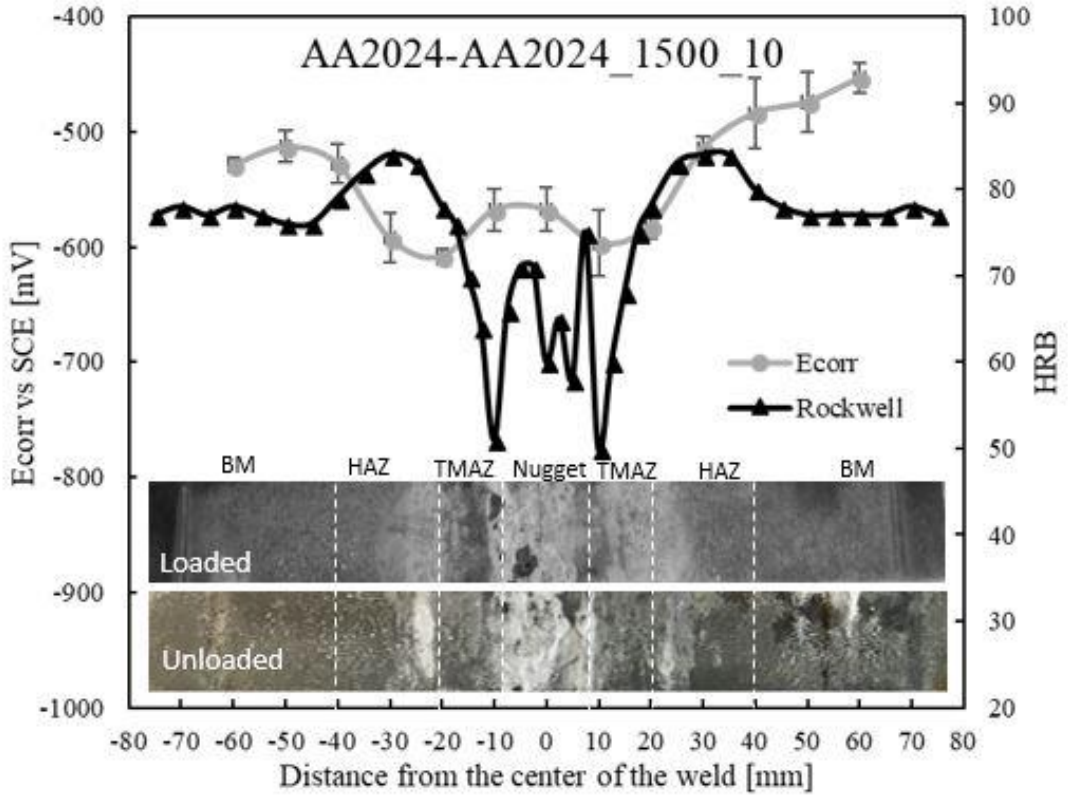

Figure 98: Profile of local corrosion potential for the AA2024-AA2024 unloaded specimen welded with speed=1500 rpm and feed=10 mm/min.

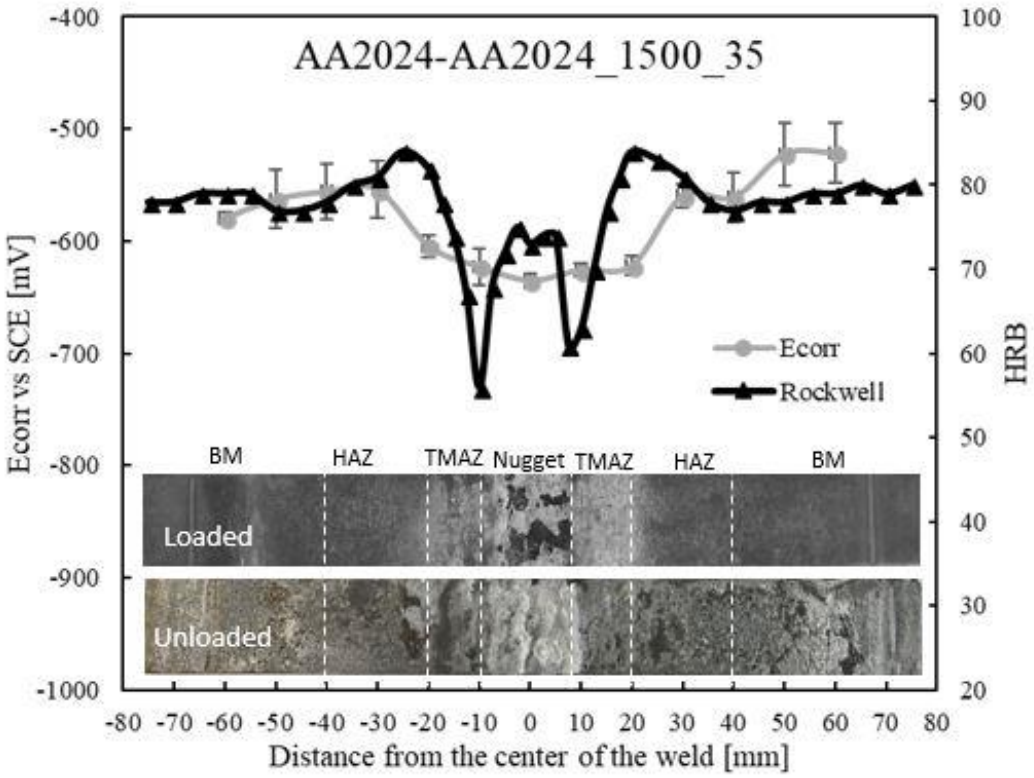

Figure 19: Profile of local corrosion potential for the AA2024-AA2024 unloaded specimen welded with speed=1500 rpm and feed=35 mm/min.

The distribution and the size of the second phases also affect the free corrosion potential. The joint is less noble than the base metal. In this works, no significant differences in open circuit potential values depending on the welding parameters have been noticed. In general, corrosion of AA2024 aluminum alloys initiates at micrometric second phases. In fact, the corrosion potential distribution is due to the presence of sub-micrometric precipitate. In the correspondence of the nugget, copper rich precipitates at grain boundaries and free precipitates zones inside the grain can be noticed. The free precipitate zones are less noble than the base material, unaffected by the welding process. The precipitation of copper-rich second phases causes the depletion of copper in the aluminum matrix; as a consequence, the corrosion potential decreases. In addition, it is well known that copper and iron rich phases are more efficient cathodes, which promote a local increase of pH and passive film destabilization occurs.

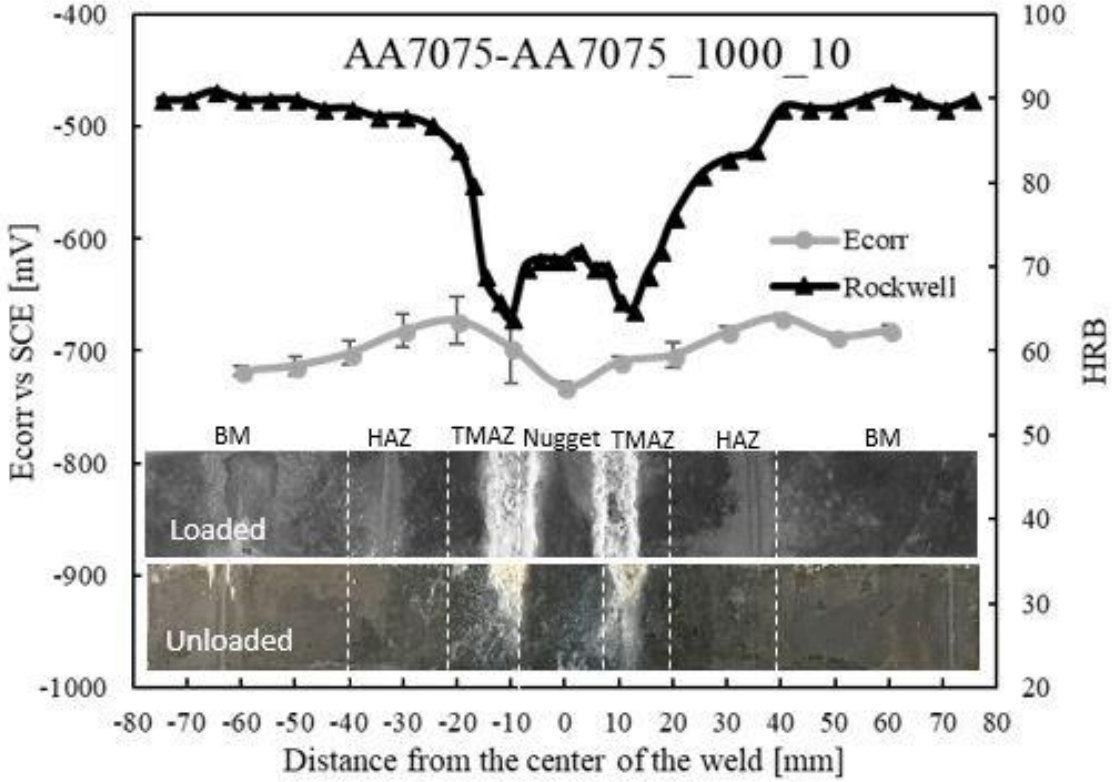

Figure 20: Profile of local corrosion potential for the AA7075-AA7075 unloaded specimen welded with speed=1000 rpm and feed=10 mm/min.

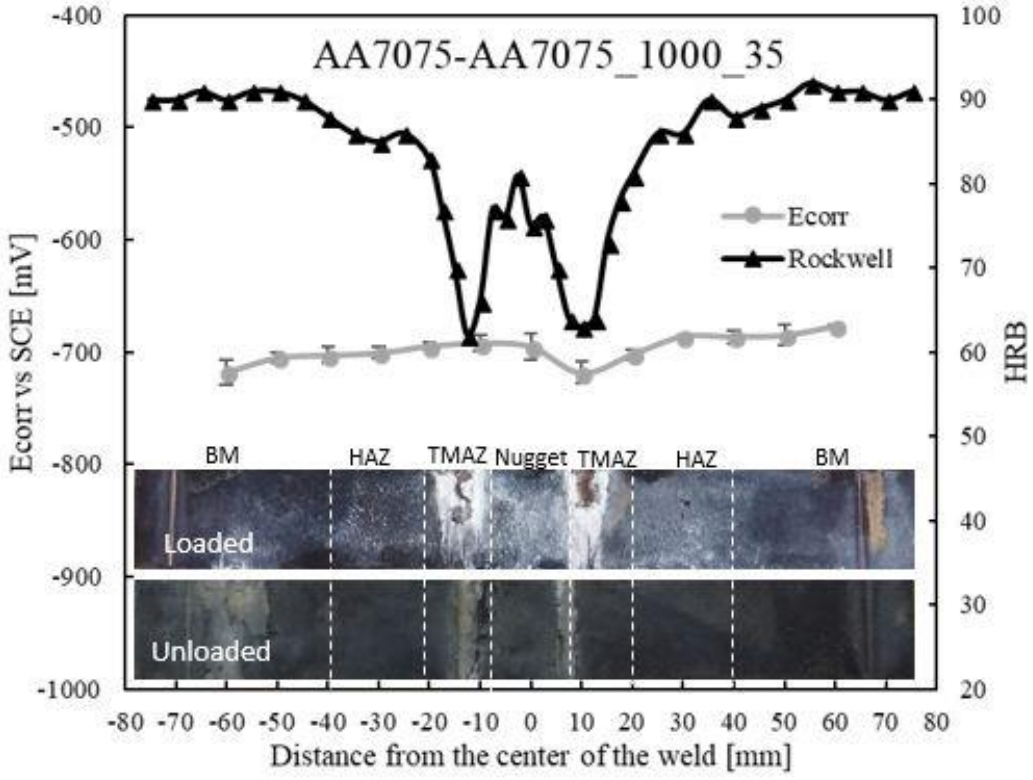

Figure 21: Profile of local corrosion potential for the AA7075-AA7075 unloaded specimen welded with speed=1000 rpm and feed=35 mm/min.

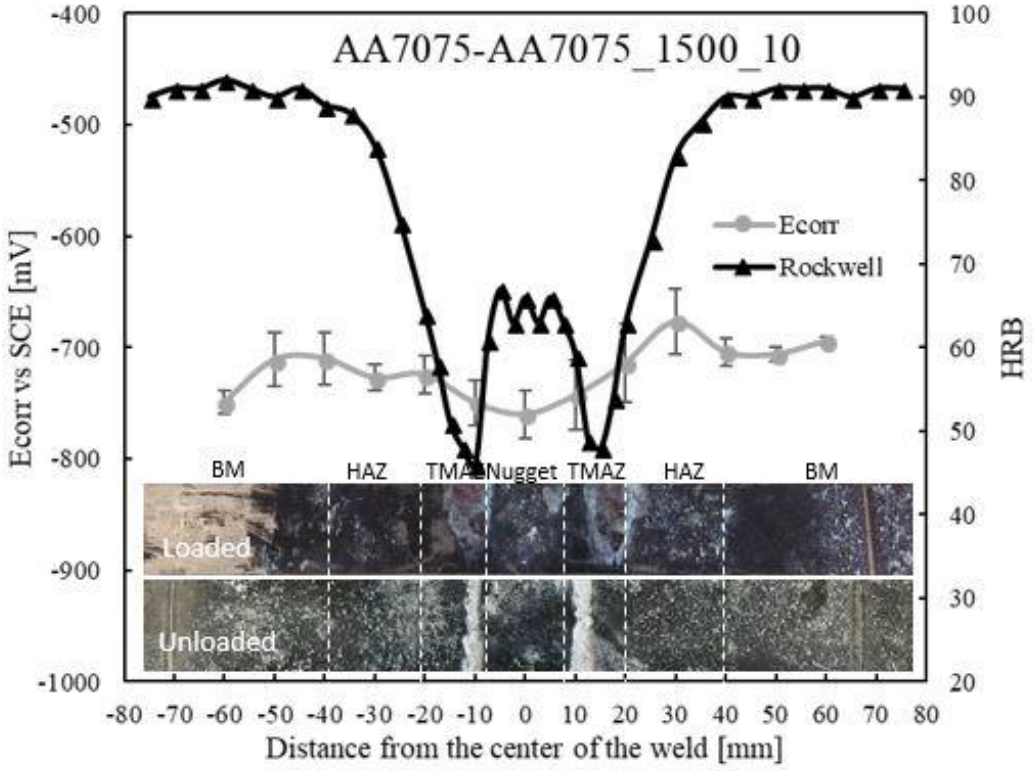

Figure 22: Profile of local corrosion potential for the AA7075-AA7075 unloaded specimen welded with speed=1500 rpm and feed=10 mm/min.

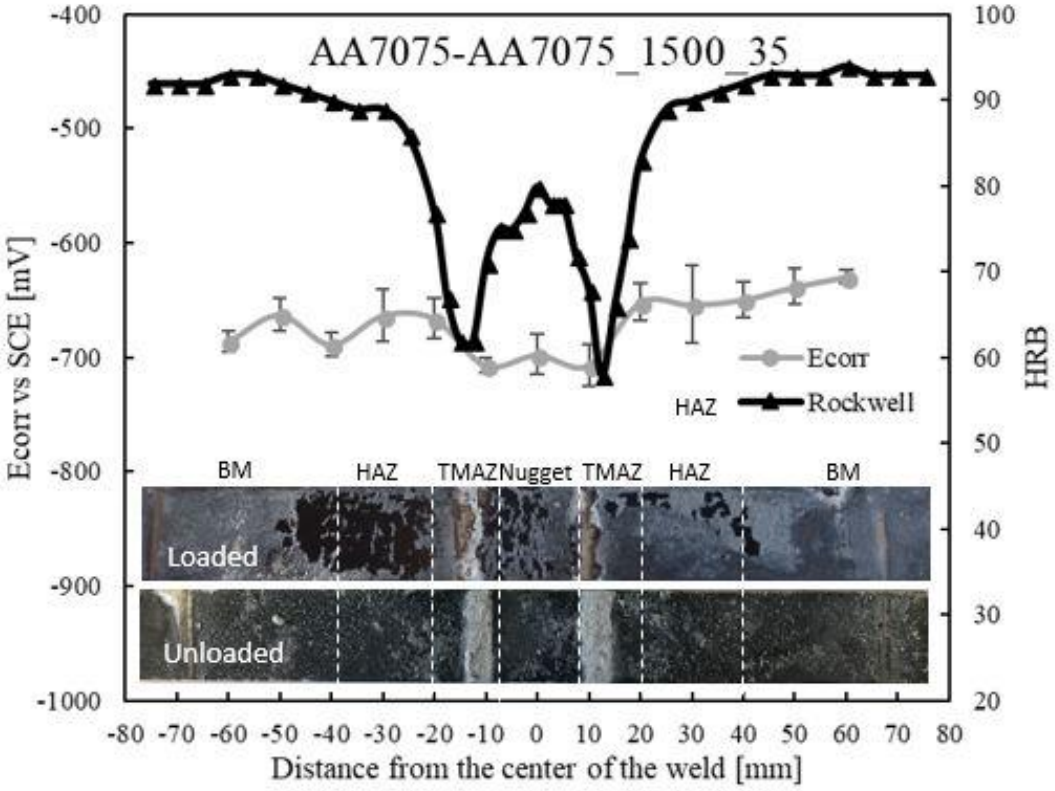

Figure 23: Profile of local corrosion potential for the AA7075-AA7075 unloaded specimen welded with speed=1500 rpm and feed=35 mm/min.

The corrosion potential of the AA7075-AA7075 alloy does not seem to be influenced neither by the feed rate nor by the rotational speed. Moreover, the trend of the potential varies slightly along the longitudinal direction of the specimen. Moreover, no clear separation between the potentials of base metal, HAZ and nugget was observed. In the case of AA7075 alloy, the precipitates of $MgZn_2$, which assure the strength of the matrix, are anodic with respect to the same matrix. As described by Andreatta et al [28], these precipitates are particularly reactive and, as a result of heating, they coalesce to the grain edge. This situation occurs, for example, in over-aging conditions leading to intense intergranular corrosion. These conditions occur mainly in the HAZ, that is particularly affected by the phenomenon because the grains retain the original size and orientation; therefore, there is an elongated grain edge in the rolling direction, which offers a preferred path to the corrosive attachment. For this reason, the aluminum matrix is fully active in this area.

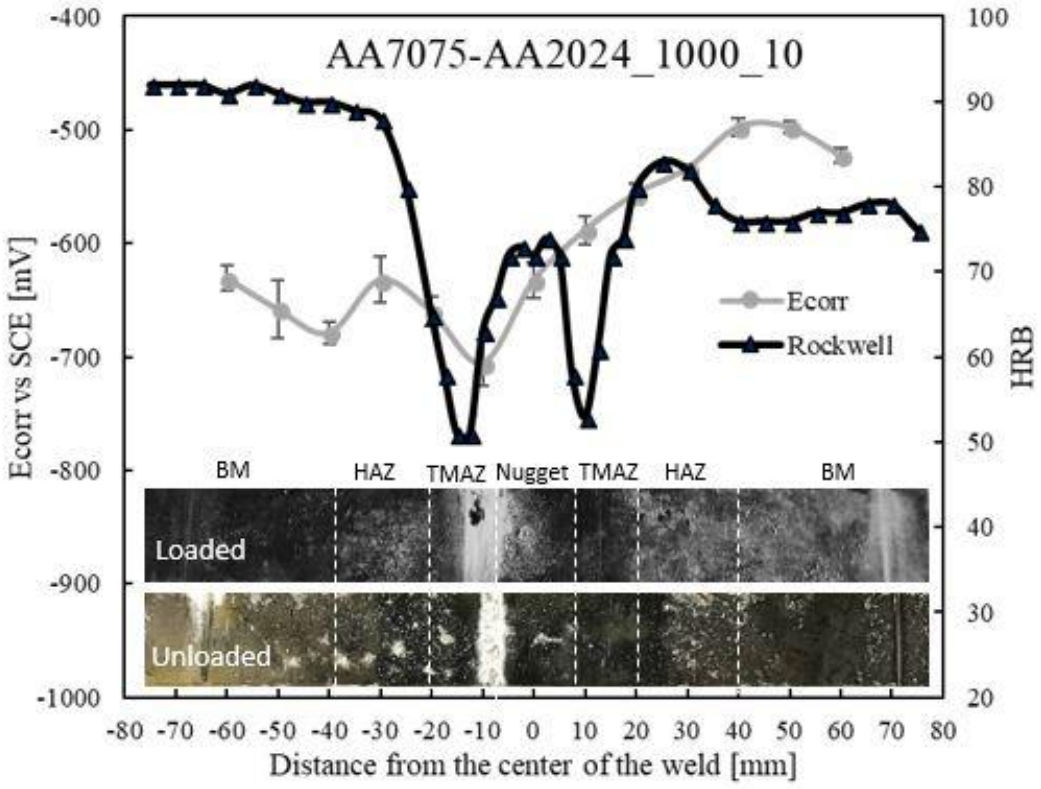

Figure 24: Profile of local corrosion potential for the AA7075-AA2024 unloaded specimen welded with speed=1000 rpm and feed=10 mm/min.

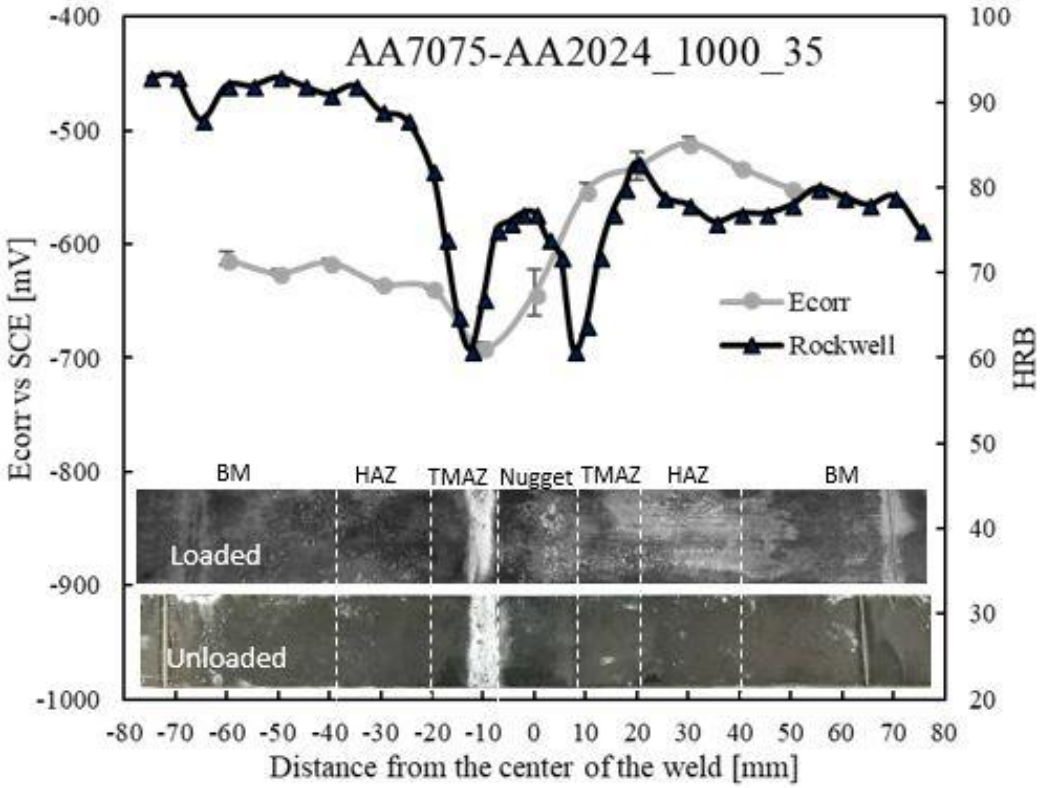

Figure 25: Profile of local corrosion potential for the AA7075-AA2024 unloaded specimen welded with speed=1000 rpm and feed=35 mm/min.

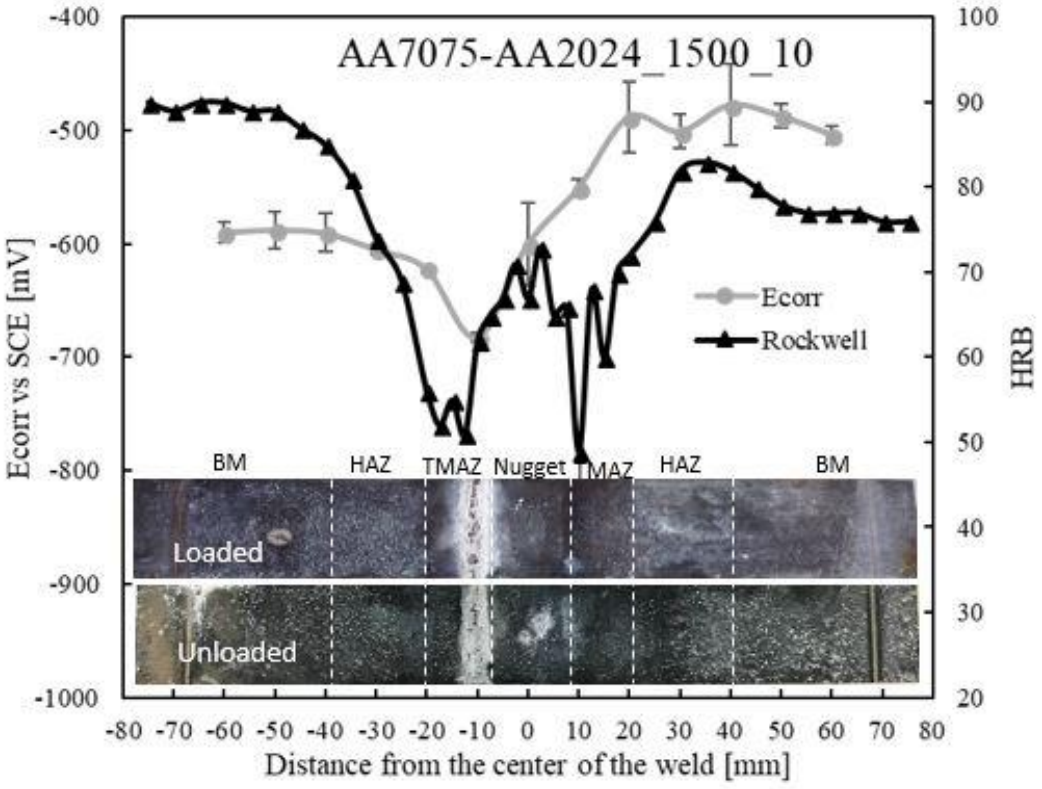

Figure 26: Profile of local corrosion potential for the AA7075-AA2024 unloaded specimen welded with speed=1500 rpm and feed=10 mm/min.

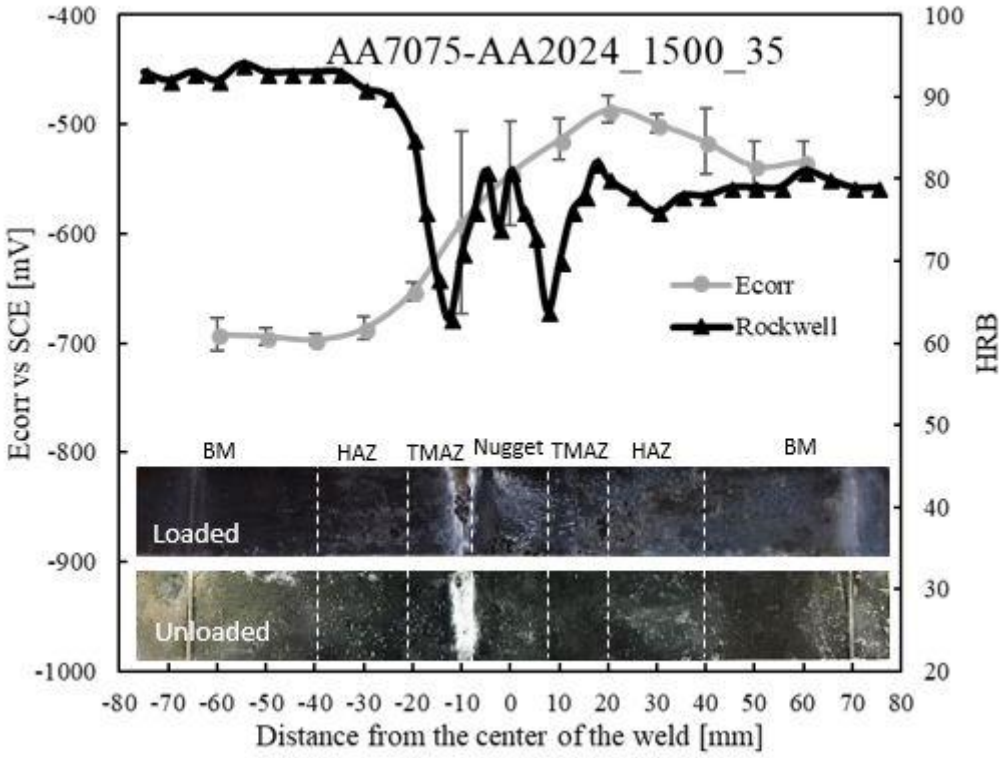

Figure 27: Profile of local corrosion potential for the AA7075-AA2024 unloaded specimen welded with speed=1500 rpm and feed=35 mm/min.

The potential trends are always well defined and much higher for the AA2024 alloy, since it is more noble than the AA7075 alloy. Mixed welding allows to identify the AA7075 alloy as an anode part, having a lower copper concentration and a high concentration of zinc. In this case, the difference of nobility between the two alloys can be considered the source of corrosion phenomena by galvanic coupling. However, the high resistivity of aluminum oxide inhibits the localized galvanic corrosion only in the mixed area, protecting the AA2024 alloy from the corrosion observed in the AA2024-AA2024 joints.

In all cases the welding parameters affect the thermal input and therefore may modify the size and distribution of the precipitates and the extension of nugget, TMAZ and HAZ. However, there are no systematic effects of the parameters on the corrosion potential.

3.5 Corrosion morphology

The metallographic section of the AA2024-AA2024 specimens showed an intense intergranular attack on the loaded specimens, in correspondence of the nugget, that grows perpendicularly to the direction of load application, both on the tensioned and compressed sides. This attack is not present on the un-loaded specimens (Figure 28). It is possible to assert that the presence of intergranular attack in friction stir welded Al-Cu alloy is due to the precipitation of Cu-rich intermetallic particles at grain boundaries in the nugget (Figure 29), which results in the formation of anodically-active Cu-depleted regions adjacent to the boundaries.

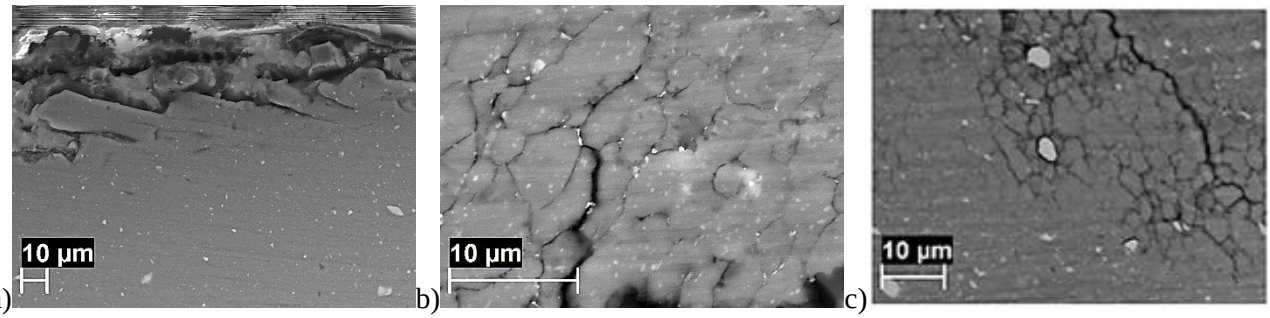

Figure 28: Metallographic section of un-loaded (a) and loaded (b-c) AA2024-AA2024 joint after 1400 hours of immersion in aerated 0.6M NaCl solution (a and b specimen welded with S=1000 rpm and f=10 mm/min, c specimen welded with S=1500 rpm and f=10 mm/min).

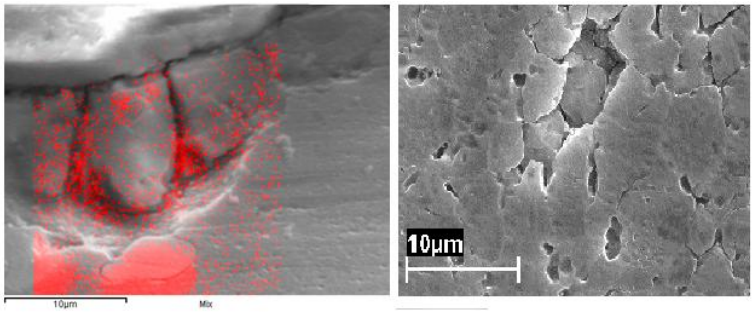

Figure 29: Chemical analysis and SEM image of the precipitates in the AA2024-AA2024 nugget welded with S=1000 rpm and f=10 mm/min (red dots underline the presence of copper).

In the absence of macroscopic cracks, the morphology of corrosion can be considered not properly stress corrosion cracking, but rather a Stress Enhanced Intergranular Corrosion, due to the microstructural modifications of the alloy [36].

AA7075 welded joints, regardless of the adopted welding parameters, showed an attack concentrated towards the limits of the TMAZ, that propagates becoming exfoliating at the rolling bands of the sheet, even though with a different intensity (Figure 30). Contrary to the results observed for the alloy AA2024, the nugget is not corroded. The attack is more affected by the microstructure than by the applied stress and grows in the direction of the precipitates coarsened by the thermal action of the welding.

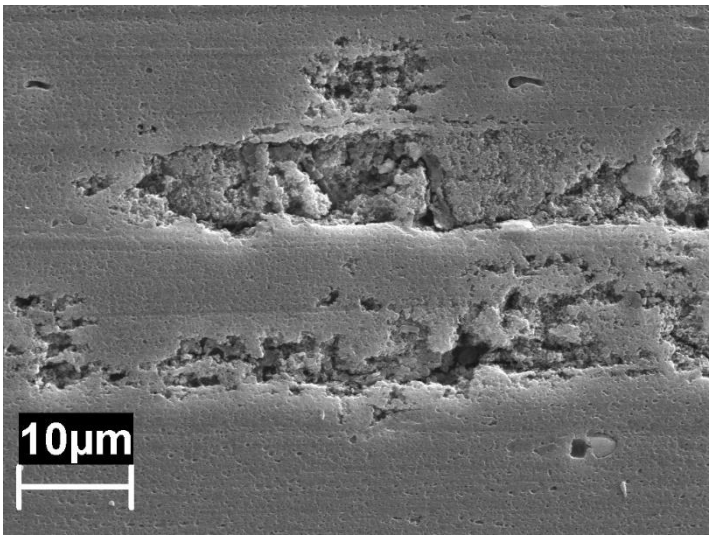

Figure 30: Corrosion morphology of an AA7075-AA7075 joint welded with S=1000 rpm and f=10 mm/min.

Corrosion is more severe in the mixed joints and it is limited in the TMAZ of AA7075, whilst only localized attack in correspondence of larger precipitates of AA2024 can be observed. $MgZn_2$ precipitates of alloy 7075 are anodic with respect to the aluminum matrix, they are very reactive and prone to grow preferentially at the grain boundaries. Aluminum matrix is active in such areas, as demonstrated by low corrosion potentials. Metallographic alloy texture, with elongated grains in the direction of plastic deformation, prevails on the external stress, leading to an attack moving from the welding to the base metal.

4. Conclusions

The paper investigates the effect of the process parameters on the mechanical properties and the corrosion behavior of butt joints obtained by friction stir welding (FSW). In almost all cases, the best conditions, in terms of mechanical resistance, were obtained for intermediate values of rotational speed and feed rate.

FSW process modify the microstructure of the alloy and, as consequence, the hardness, the corrosion potential and the corrosion morphology in the presence of external loading. Different behaviors were observed for the AA2024 and the AA7075 joints: the first showed lowest values of hardness in the TMAZ, and more anodic potential in the nugget. Such effect was attributed to the precipitation of copper rich second phases at the recrystallized grain boundaries that depletes the aluminum matrix and stimulates corrosion in these zones. As a consequence of the microstructural modification, in the presence of applied stress, intense Stress Enhanced Intergranular Corrosion occurred in the AA2024-AA2024 joints.

In the AA7075 both the lowest value of hardness and the more anodic corrosion potentials are located in the TMAZ; this alloy unlike the AA2024, is artificially aged and the FSW causes solubilization of the anodic precipitates of $MgZn_2$ in the recrystallized areas of the nugget and coarsening of these precipitates at the grain border in the TMAZ. Severe localized attack occurs in the TMAZ of these joints, growing in the rolling direction, because the preferential path created by the oriented grains prevails on the effect of the external applied load. In the mixed joints, corrosion is more severe and it is limited in the TMAZ of the AA7075 alloy with a similar mechanism. Within the limits of the present investigation, no systematic relationship between the process parameters and the corrosion behavior can be observed. Based on this consideration, the selection of the process parameters can be only done through the UTS optimization.

References

[1] Thomas W, Nicholas E, Needham J, Murch M, Templesmith P, Dawes C. Improvements Relating to Friction Welding: International Patent. WO 1993010935, 10 June 1993.

[2] Thomas W, Nicholas E, Needham J, Murch M, Templesmith P, Dawes C. Friction Welding: US Patent. US 5460317 A, 24 October 1995.

[3] Sonne M, Tutum C, Hattel J, Simar A, De Meester B. The effect of hardening laws and thermal softening on modeling residual stresses in FSW of aluminum alloy 2024-T3. Journal of Materials Processing and Technologies 2013; 213: 477–486.

[4] El-Danaf E, El-Rayes M. Microstructure and mechanical properties of friction stir welded 6082 AA in as welded and post weld heat treated conditions. Materials and Design 2013; 46: 561–572.

[5] Gangwar K, Ramulu M. Friction stir welding of titanium alloys: A review. Materials & Design 2018; 141: 230–255.

[6] Cao X, Jahazi M. Effect of tool rotational speed and probe length on lap joint quality of a friction stir welded magnesium alloy. Materials and Design 2011; 32: 1–11.

[7] Martinsen K, Hu S, Carlson B. Joining of dissimilar materials. CIRP Annals - Manufacturing Technology 2015; 64: 679-699.

[8] Madhavarao S, Rama Bhadri Raju Ch, Seshu kumar GSV. Investigation of Friction Stir Welding of Metal Matrix Composites Using a Coated Tool. Materials Today: Proceedings 2018; 5, 2, part 2: 7735–7742.

[9] Johnson R, Threadgill P. Progress in friction stir welding of aluminium and steel for marine applications. RINA Conference: Advanced Marine Materials: Technology and Applications 2003.

[10] Heinz A, Haszler A, Keide C, Moldenhauer S, Benedictus R, Miller W. Recent development in aluminum alloys for aerospace applications. Material Science and Engineering A 2000; 280, n. 1: 102-107.

[11] Thomas W, Nicholas E. Friction stir welding for the transportation industries. Materials & Design 1997; 18, n. 4-6: 269-273.

[12] Mishra R, Ma Z. Friction stir welding and processing. Materials Science and Engineering: R: Reports 2005; 50, n. 1-2: 1-78.

[13] Nandan R, DebRoy T, Bhadeshia H. Recent advances in friction-stir welding – Process, weldment structure and properties. Progress in Materials Science. 2008; 53, n. 6: 980-1023.

[14] Yuan W, Mishraa R, Webba S, Chenb Y, Carlsonb B, Herlinge D, Grante G. Effect of tool design and process parameters on properties of Al alloy 6016 friction stir spot welds. J. Mat. proc. Tech. 2011; 972-977.

[15] Patel AR, Kotadiya DJ, Kapopara JM, Dalwadi CG, Patel NP, Rana HG. Investigation of Mechanical Properties for Hybrid Joint of Aluminium to Polymer using Friction Stir Welding (FSW). Materials

Today: Proceedings 2018; 5: 4242-4249.

[16] Fanelli P, Vivio F, Vullo V. Experimental and numerical characterization of FSSW joints. Eng. Fract. Mech. 2012; 81: 17-25.

[17] Khodir SA, Shibayanagi T. FSW of dissimilar AA2024 and AA7075 aluminum alloys. Mat. Sci. and Eng. B 2008; 148: 82-87.

[18] Avinash P. Friction stir welded butt joints of AA2024 T3 and AA7075 T6 aluminum alloys. Procedia Engineering 2014; 75: 98-102.

[19] D'Urso G, Giardini C, Lorenzi S, Pastore T. Fatigue crack growth in the welding nugget of FSW joints of a 6060 aluminum alloy. J. of Mat. Proc. 2014; 214: 2075-2084.

[20] Aissani M, Gachi S, Boubenider F, Benkedda Y. Design and optimization of friction stir welding tool. Mat. Man. Proc. 2010; 25: 1199-1205.

[21] Ghosh M, Kumar K, Kailas SV, Ray AK. Optimization of friction stir welding parameters for dissimilar aluminum alloys. Mat. & Des. 2010; 31, n. 6: 3033-3037.

[22] Koilraja M, Vijayanc S, Sundareswaranb V, Koteswara SR. Friction stir welding of dissimilar aluminum alloys AA2219 to AA5083 – Optimization of process parameters using Taguchi technique. Mat. & Des. 2012; 42: 1-7.

[23] Rajakumar S, Balasubramanian V. Establishing relationships between mechanical properties of aluminium alloys and optimised friction stir welding process parameters. Mat. & Des. 2012; 40: 117-135.

[24] Bousquet E, Poulon-Quintin A, Puiggali P, Devos O, Touzet M. Relationship between microstructure, microhardness and corrosion sensitivity of an AA 2024-T3 friction stir welded joint. Corrosion Science 2011; 53, n. 9: 3026-3034.

[25] Jariyaboon M, Davenport AJ, Ambat R, Connolly BJ, Williams SW, Prince DA. The effect of welding parameters on the corrosion behaviour of friction stir welded AA2024–T351. Corrosion Science 2007; 49, n. 2: 877-909.

[26] Proton V, Alexis J, Andrieu E, Delfosse J, Lafont MC, Blanc B. Characterisation and understanding of the corrosion behaviour of the nugget in a 2050 aluminium alloy Friction Stir Welding joint. Corrosion Science 2013; 73: 130-142.

[27] Andreatta F, Terryn H, de Wit JHW. Corrosion behaviour of different tempers of AA7075 aluminium alloy. Elctrochimica Acta 2004; 49: 2851-2862.

[28] Lumsden JB, Mahoney MW, Pollock G, Rhodes CG. Intergranular corrosion following Friction Stir Welding of aluminim alloy 7075-T651. Corrosion Science 1999; 55, n. 12: 1127-1135.

[29] Navaser M, Atapour M. Effect of Friction Stir processing on pitting corrosion and intergranular attack of 7075 aluminium alloy. Journal of Material Science & Technology 2015.

[30] Yasakau KA, Tedim J, Montemor MF, Salak AN, Zheludkevich ML, Ferreira MGS. Mechanisms of localized corrosion inhibition of AA2024 by ceriummolybdate nanowires. J. Phys. Chem. 2013; 117: 5811-5823.

[31] Birbilis N, Buchheit RG. Electrochemical characteristics of intermetallicphases in aluminum alloys-an experimental survey and discussion. J.Electrochem. Soc. 2005; 152: B140-B151.

[32] Ralston KD, Brunner J, e et al. Effect of Processing on Grain Size and Corrosion of AA2024-T3. Corrosion. 67: 10.

[33] Pang JJ, Liu FC, Liu J, Tan M, Blackwood DJ. Friction stir processing of aluminium alloy AA7075: microstructure, surface chemistry and corrosion resistance. Corrosion Science 2015; 106: 217-228.

[34] Zhang W, Frankel GS. Transitions between pitting and intergranular corrosion in AA2024. Electrochimica Acta 2003; 48, n. 9: 1193-1210.

[35] Gholami S, Emadoddin E, Tajally M, Borhani E. Friction Stir Processing of 7075 Al Alloy and subsequent aging treatment. Transaction of Nonferrous Metals Society of China 2015; 25, n. 9: 2847-2855.

[36] Cabrini M, Lorenzi S, Bocchi S, Pastore T, D'Urso G, Giardini C. Evaluation of corrosion behavior of AA2024 T3 welded. 20th International Corrosion Congress & Process Safety Congress 2017, Prague; 1-15.

Figure 1

Click here to download high resolution image

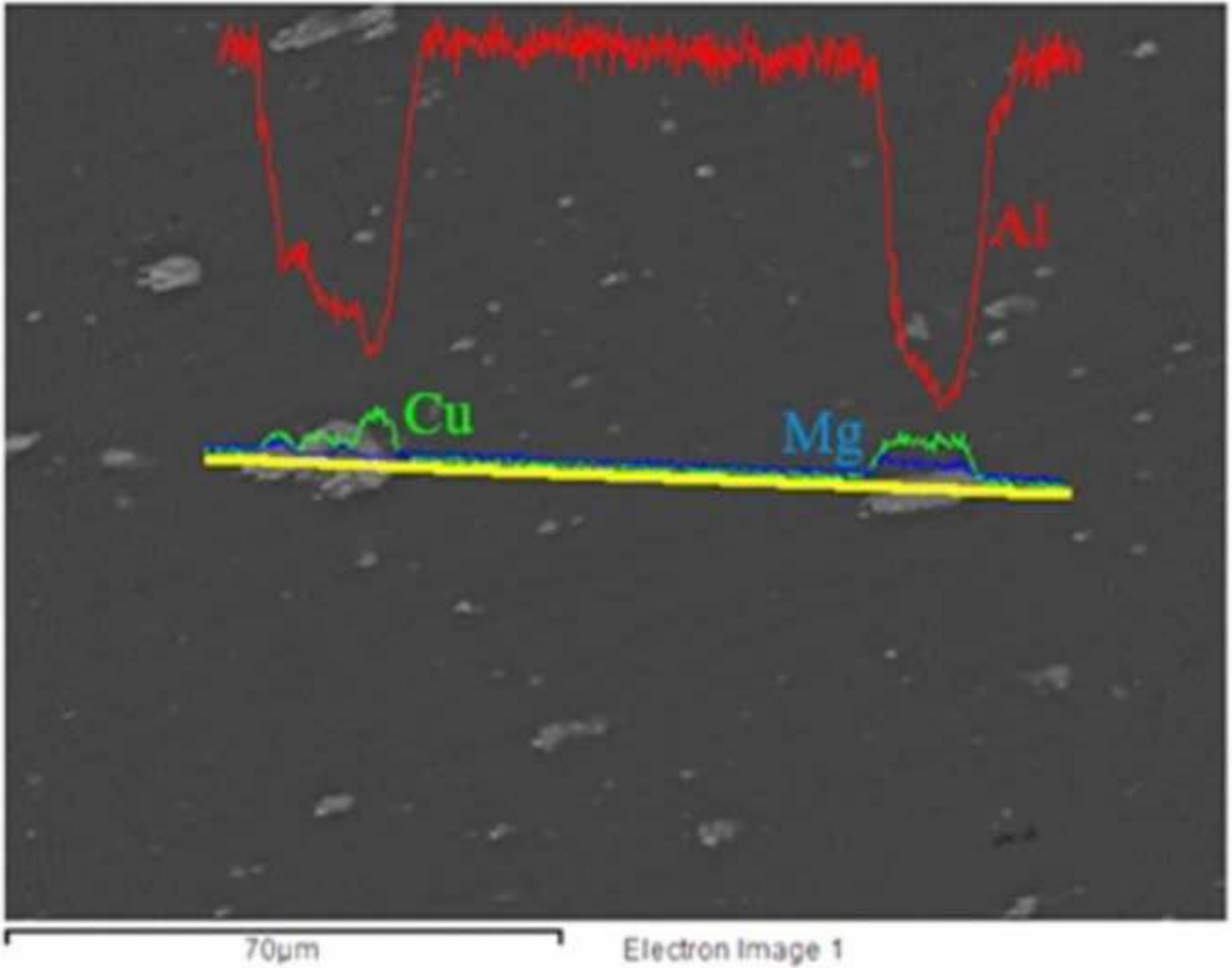

Figure 2

Click here to download high resolution image

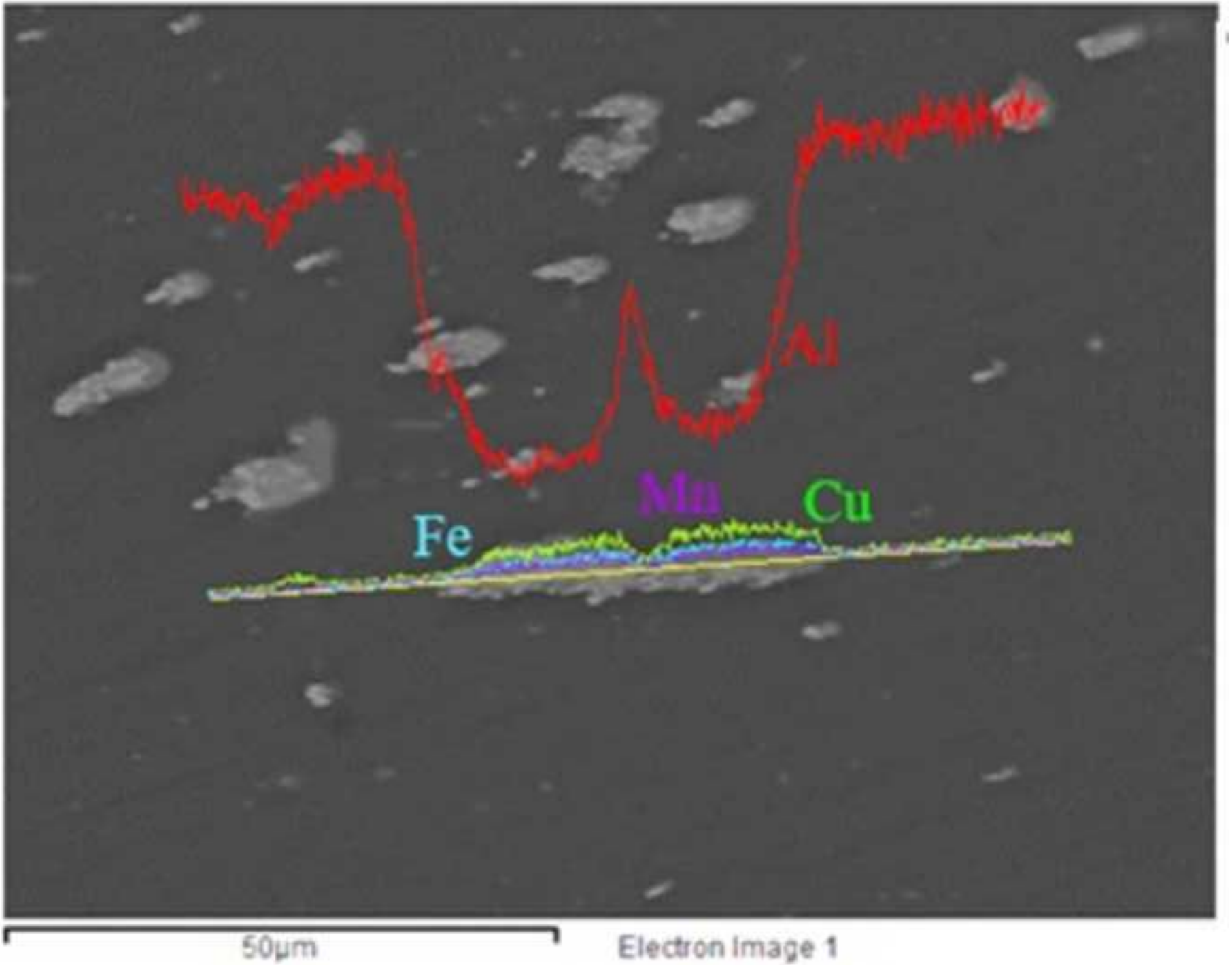

Figure 3

Click here to download high resolution image

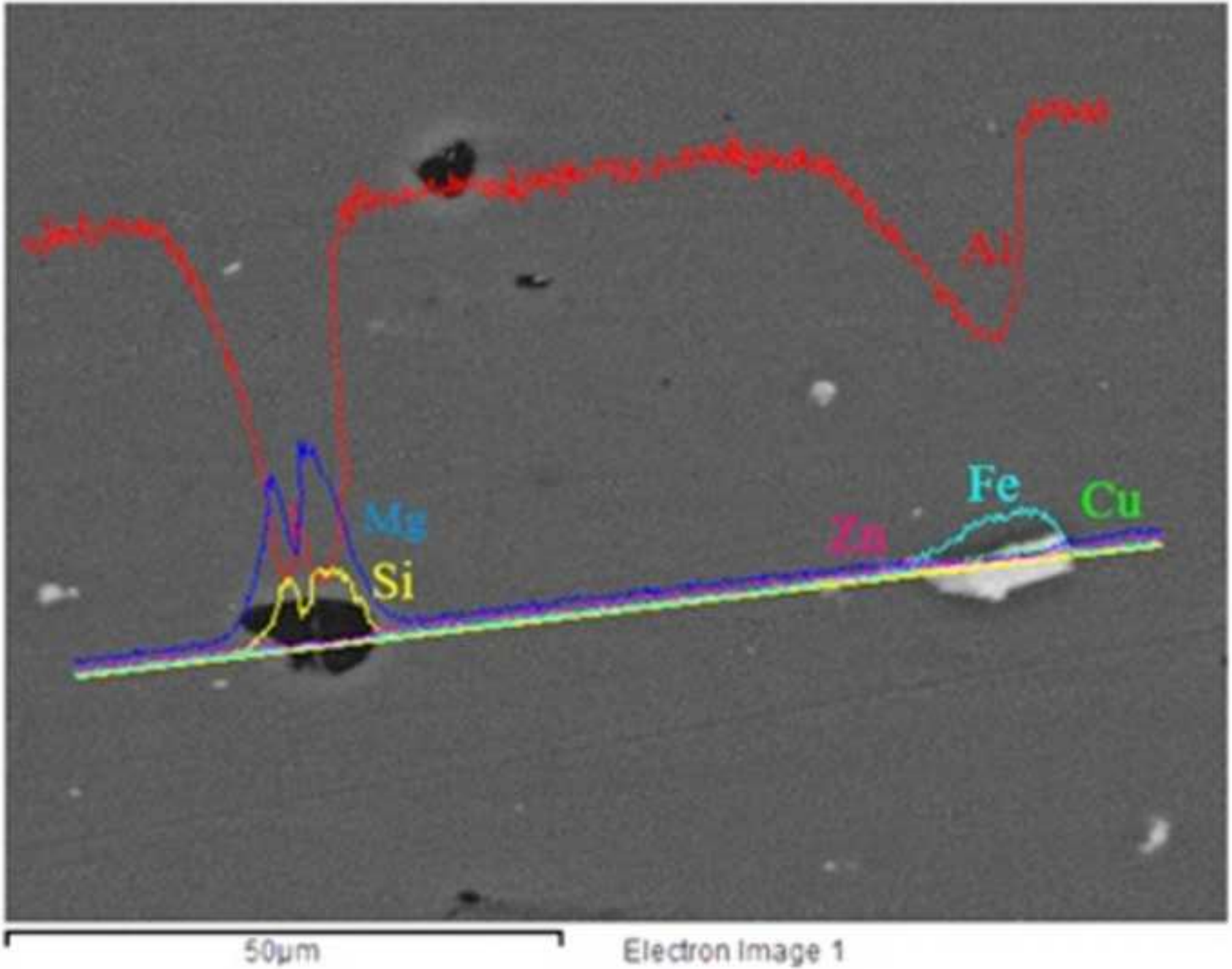

Figure 4

Click here to download high resolution image

Figure 5

Click here to download high resolution image

Figure 6a

Click here to download high resolution image

Figure 6b

Click here to download high resolution image

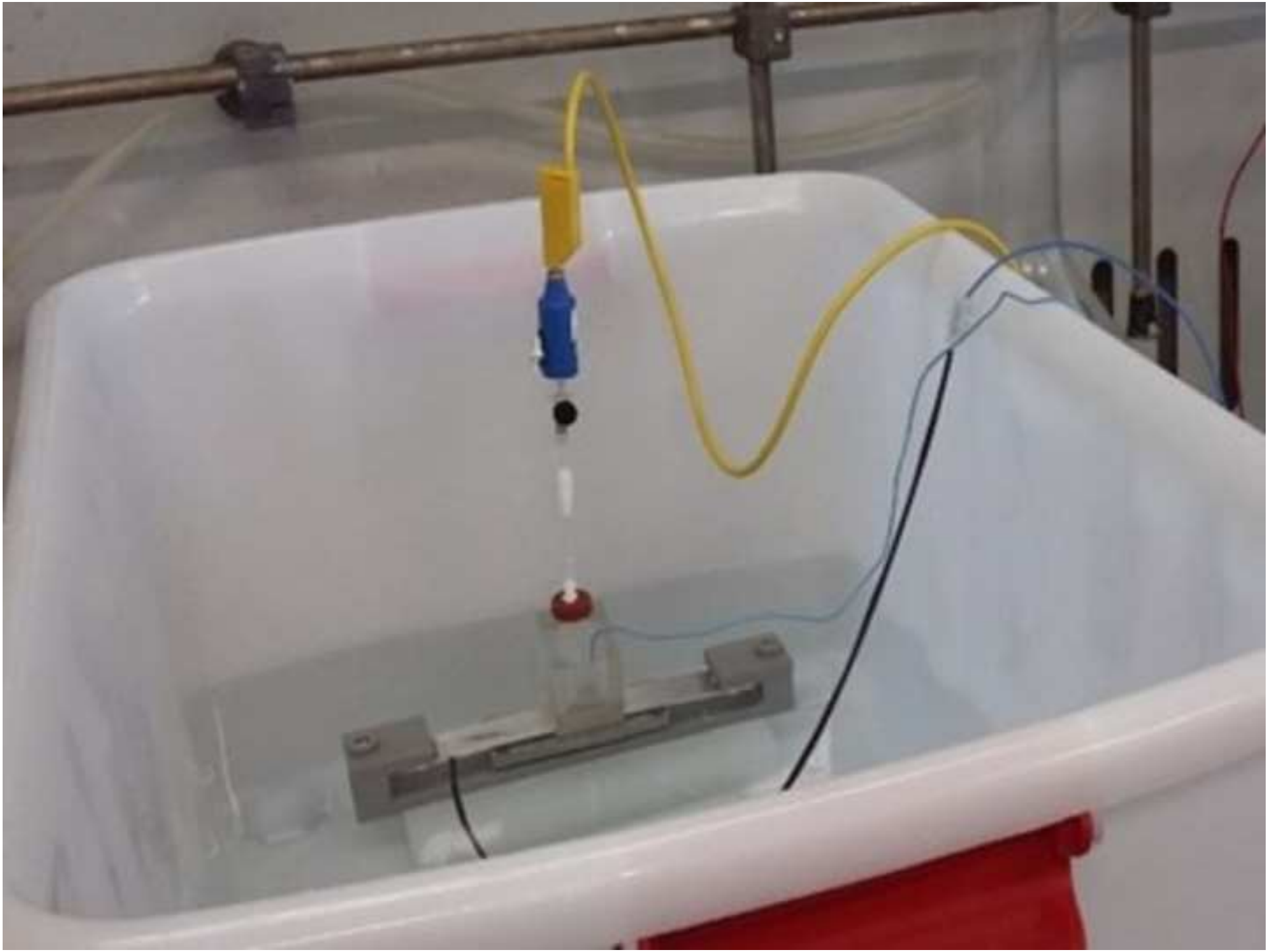

Figure 7a
Click here to download high resolution image

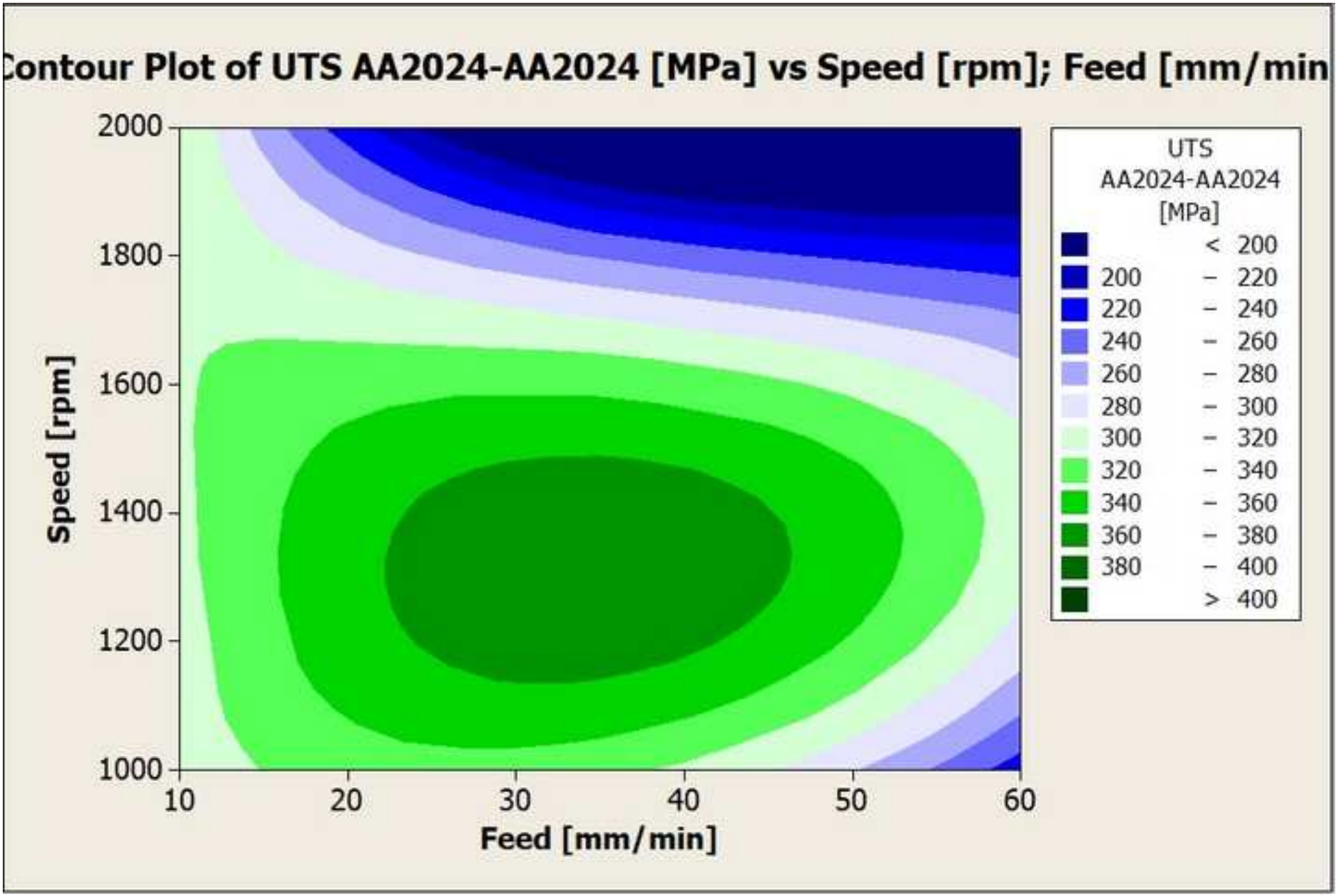

Figure 7b
Click here to download high resolution image

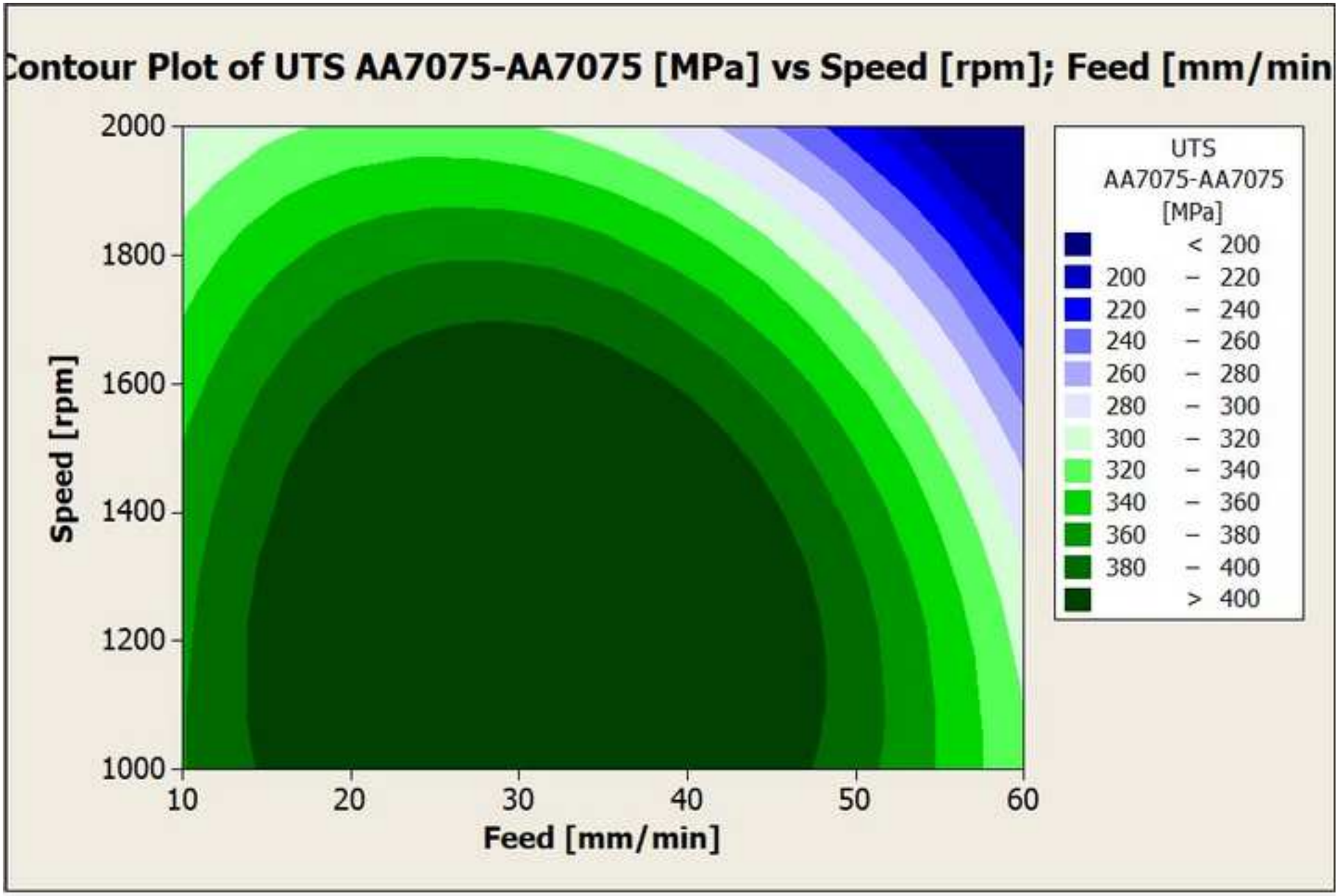

Figure 7c
Click here to download high resolution image

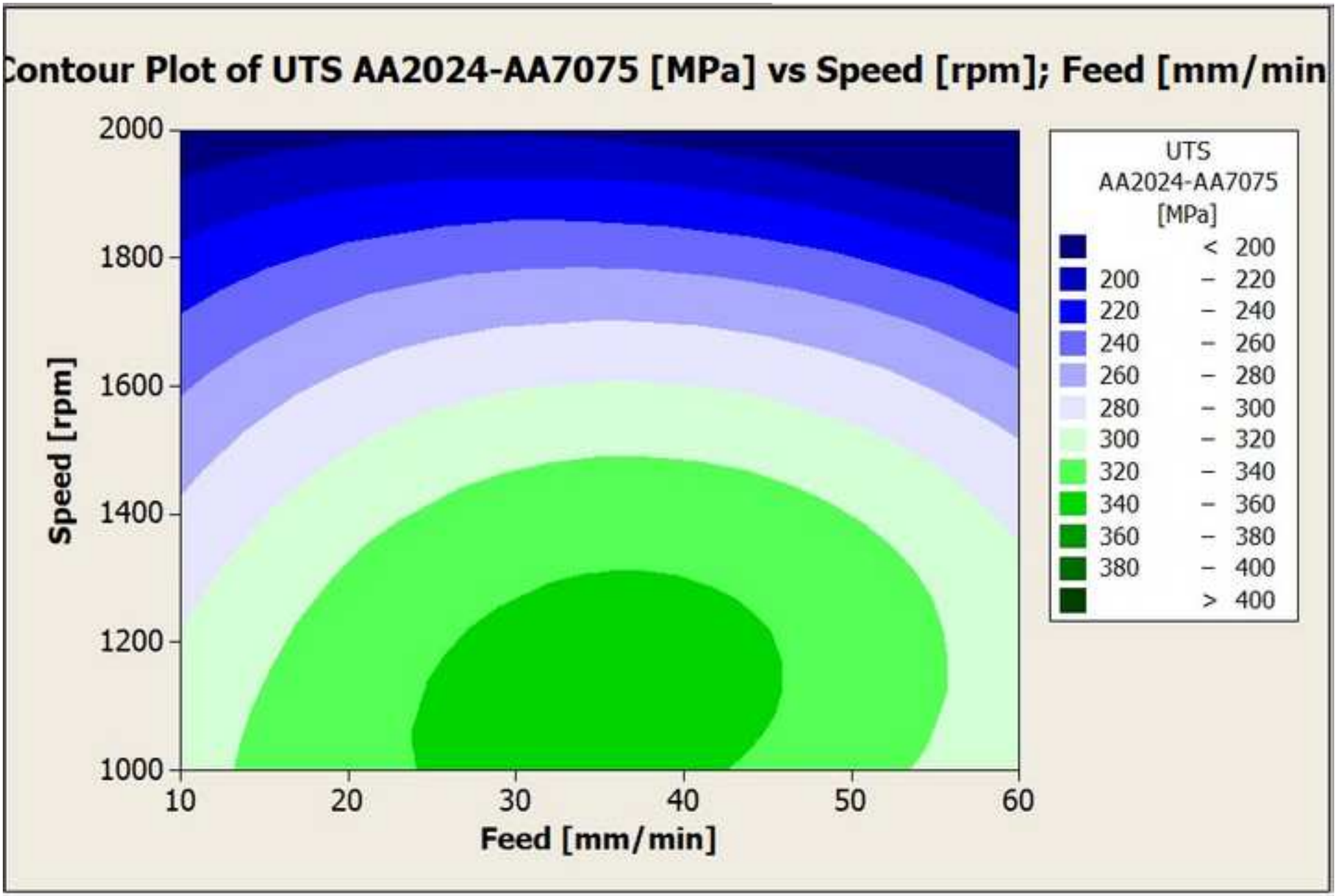

Figure 8a

Click here to download high resolution image

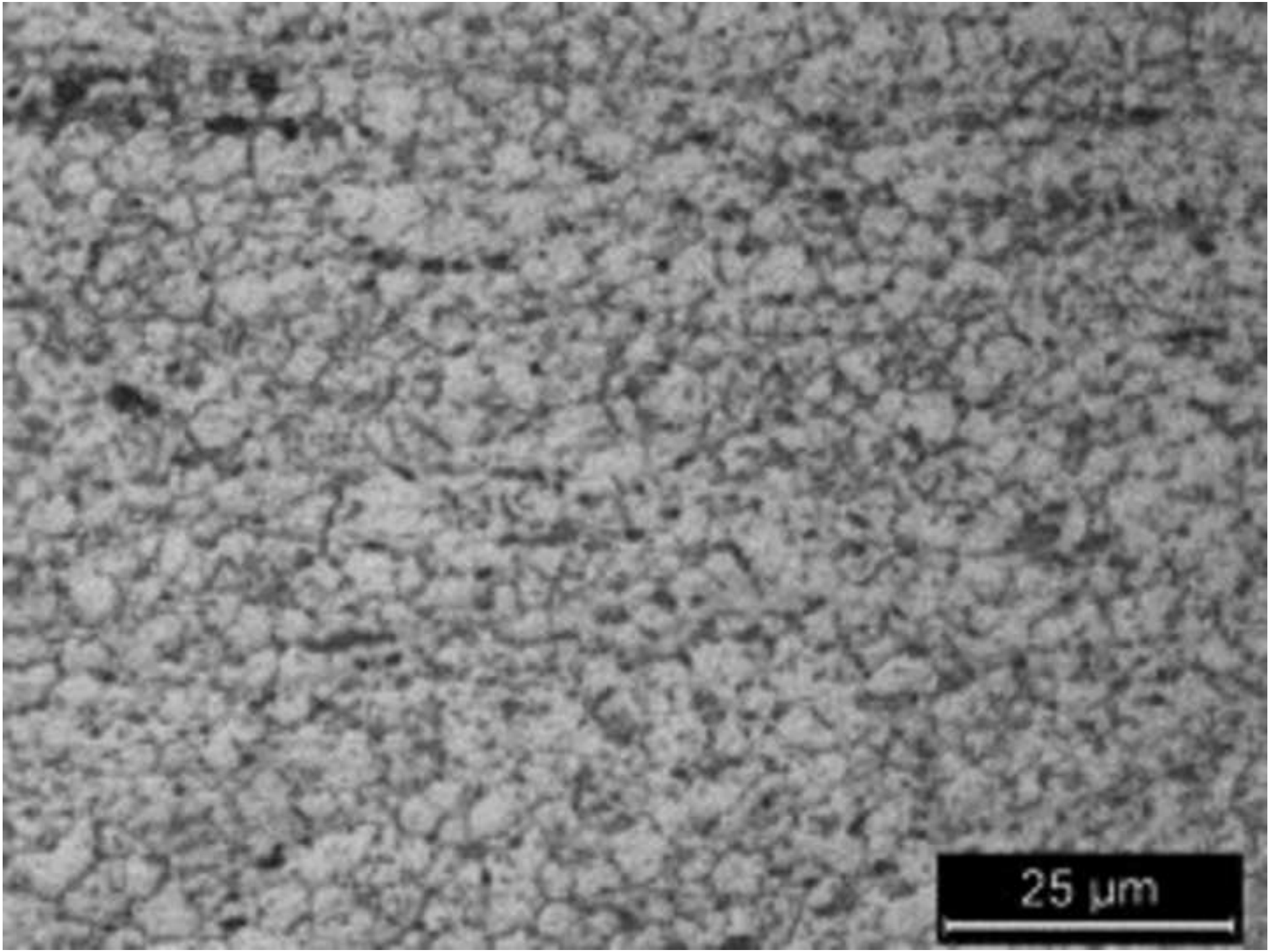

Figure 8a1

Click here to download high resolution image

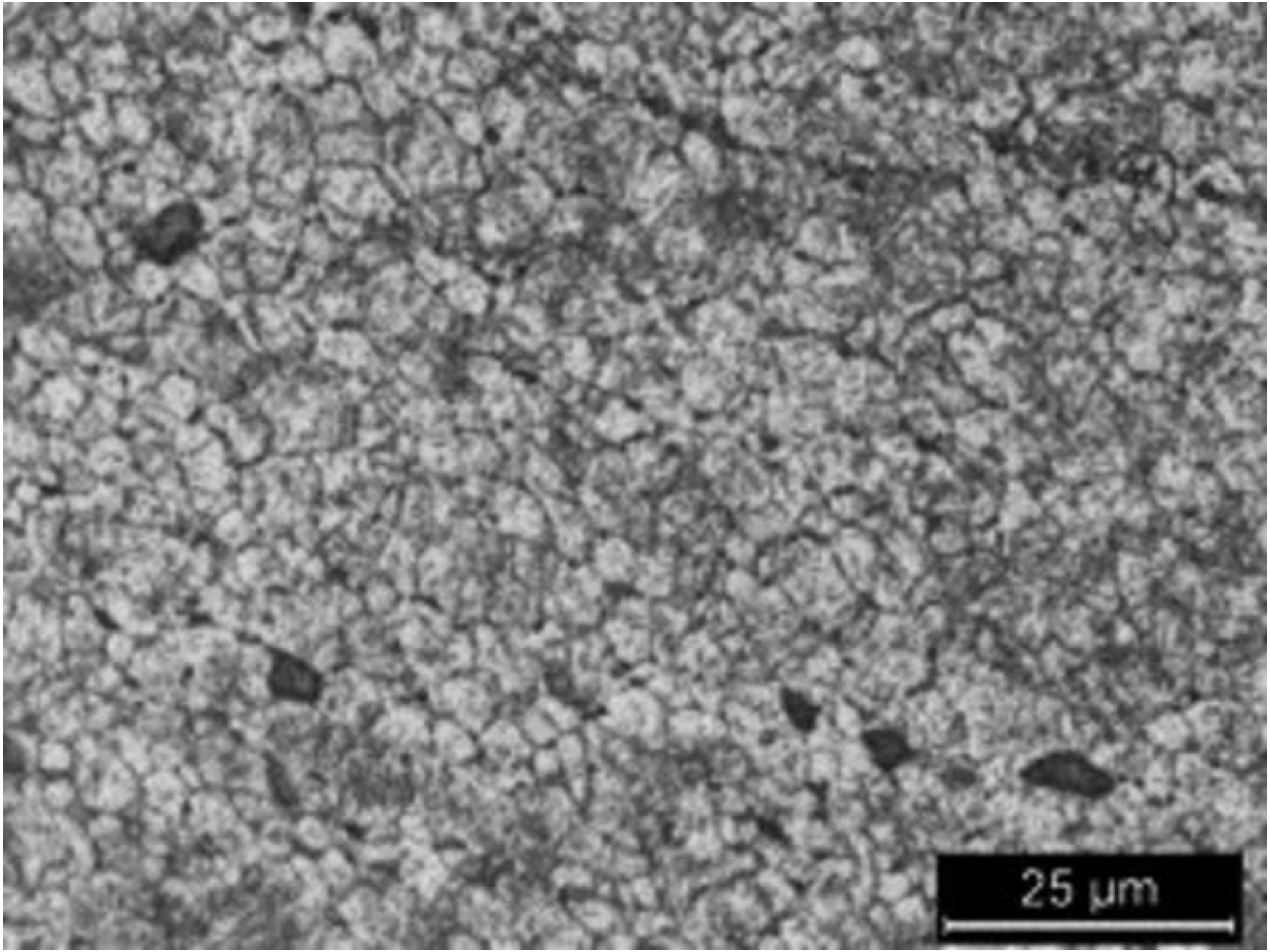

Figure 8b

Click here to download high resolution image

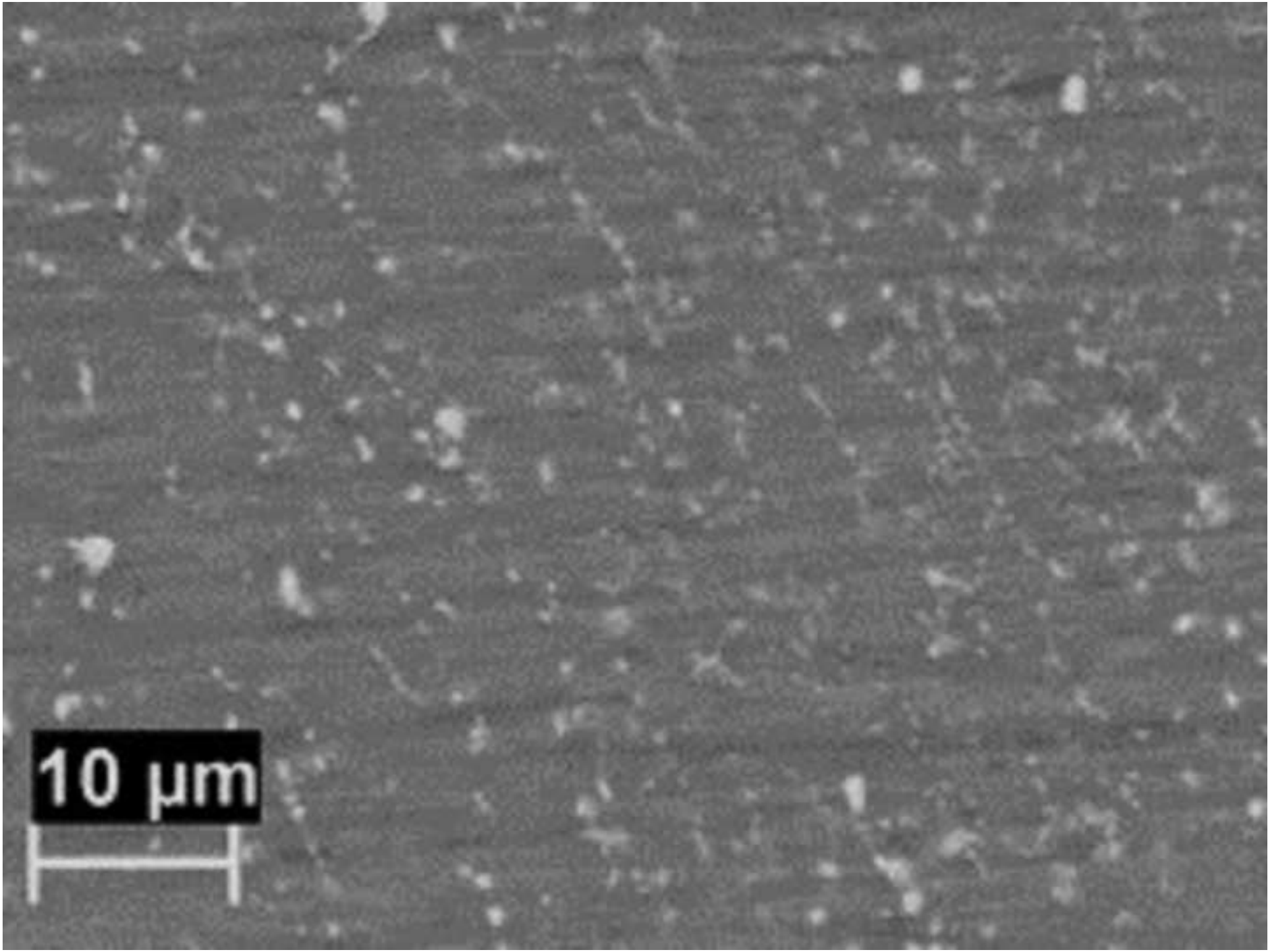

Figure 8b1

Click here to download high resolution image

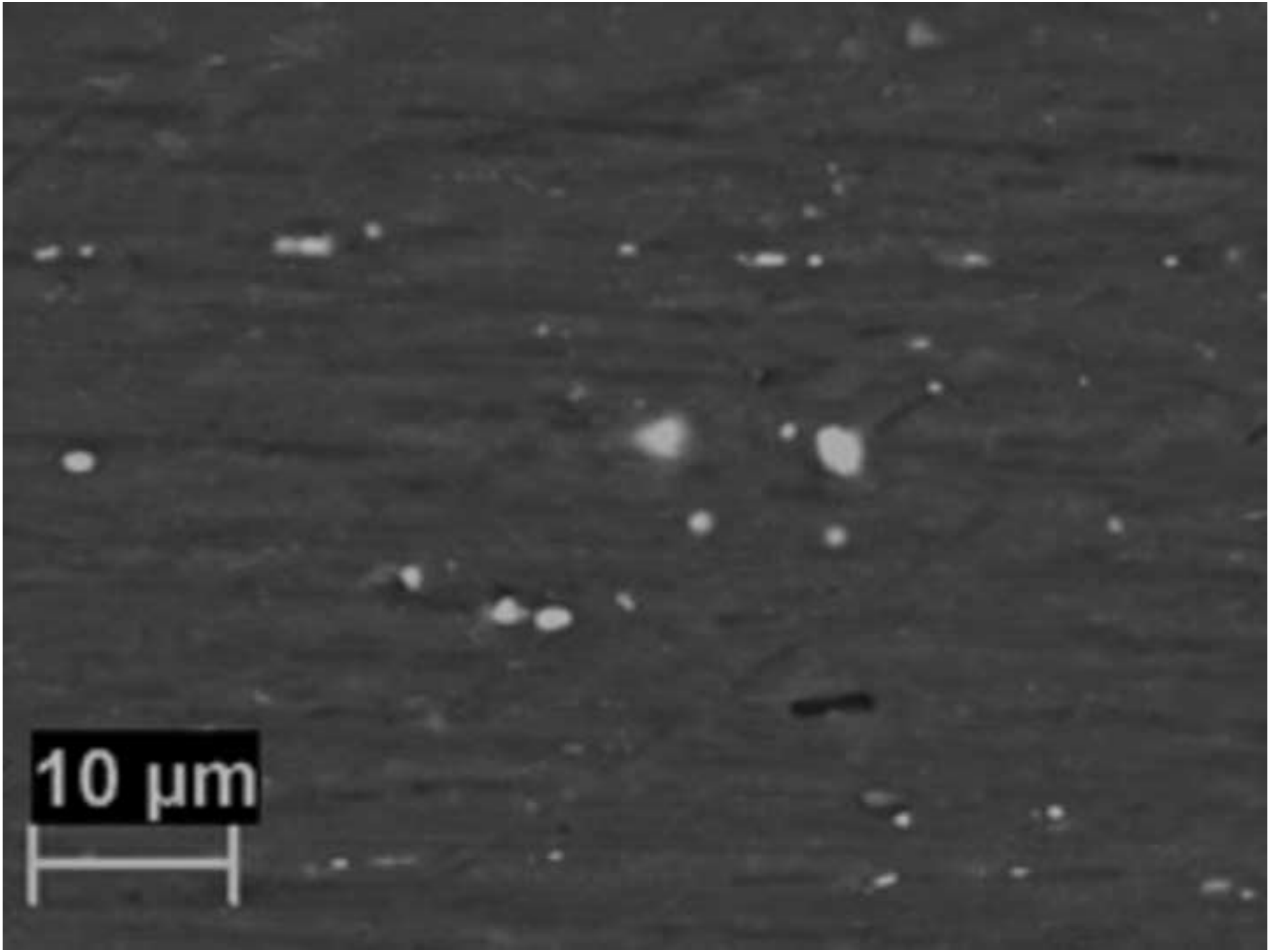

Figure 9a

Click here to download high resolution image

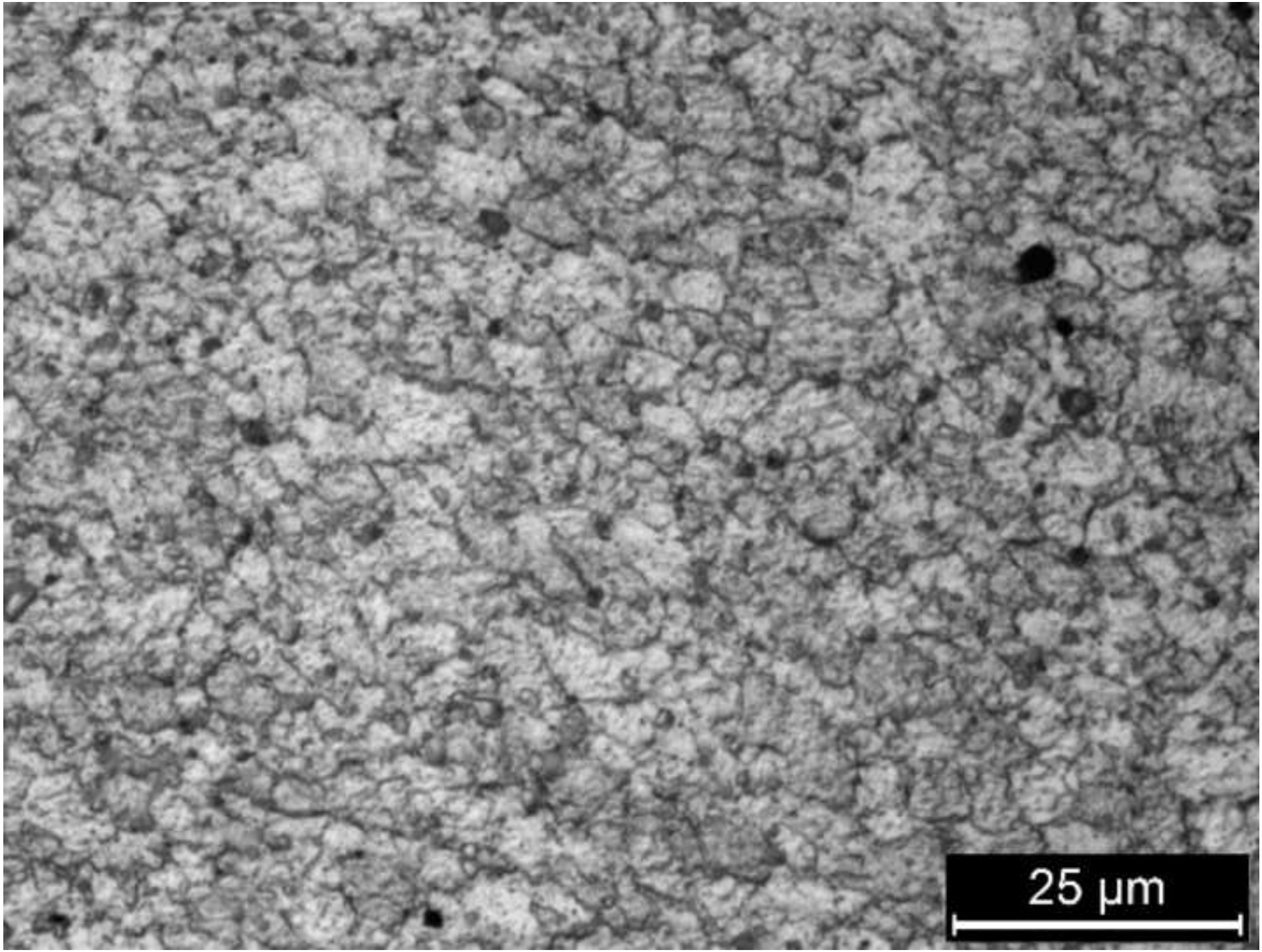

Figure 9a1
Click here to download high resolution image

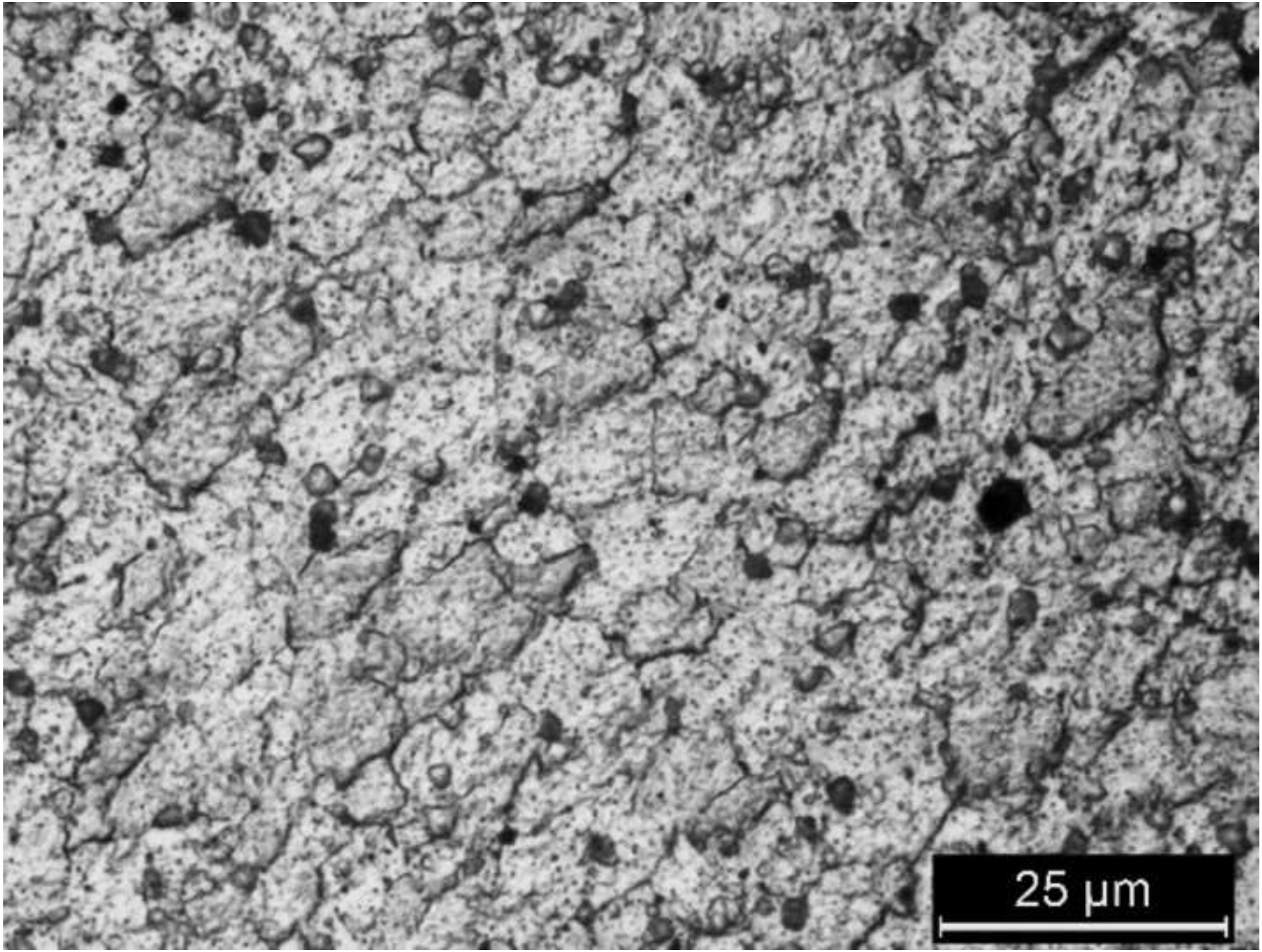

Figure 9b

Click here to download high resolution image

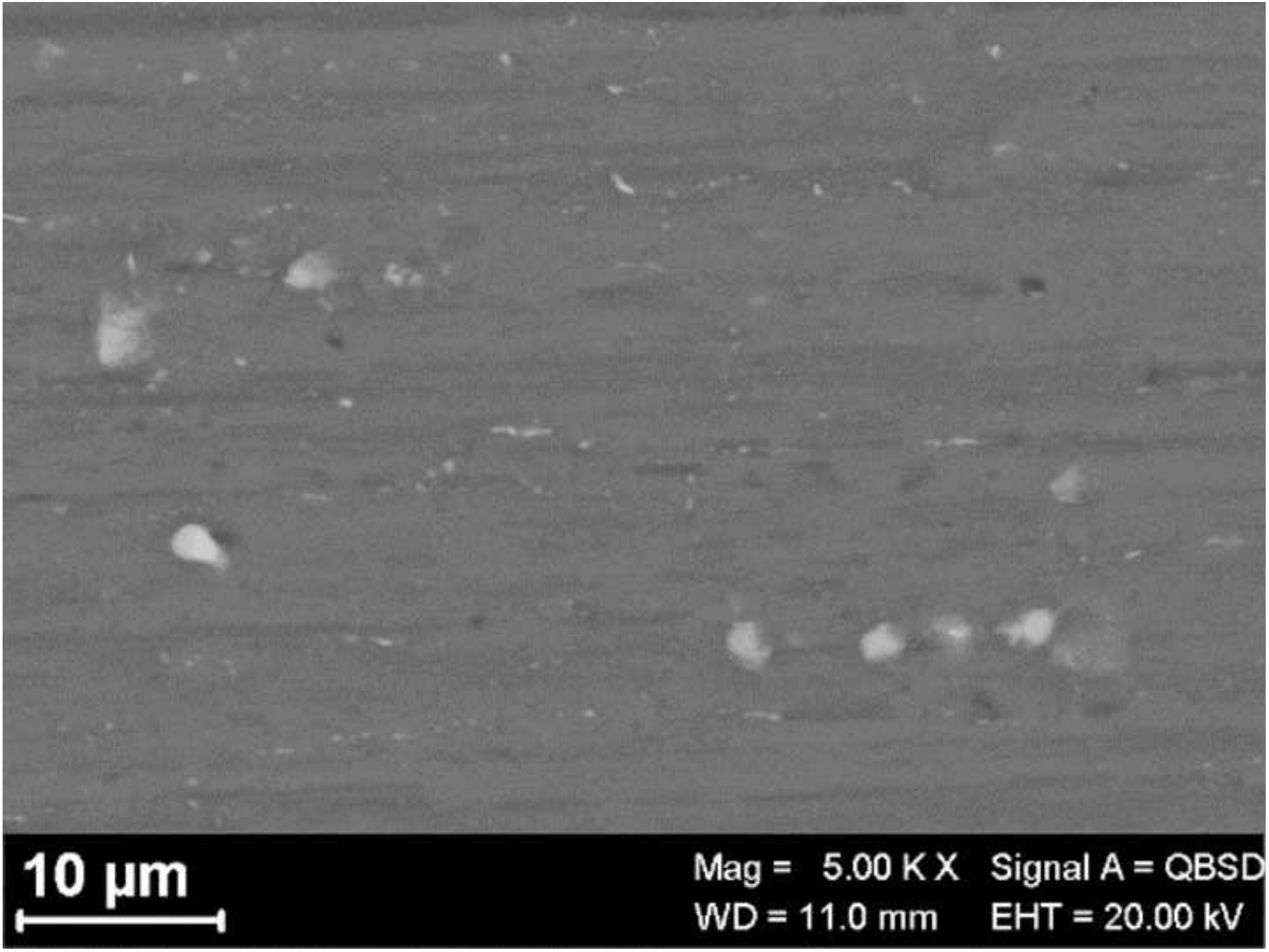

Figure 9b1

Click here to download high resolution image

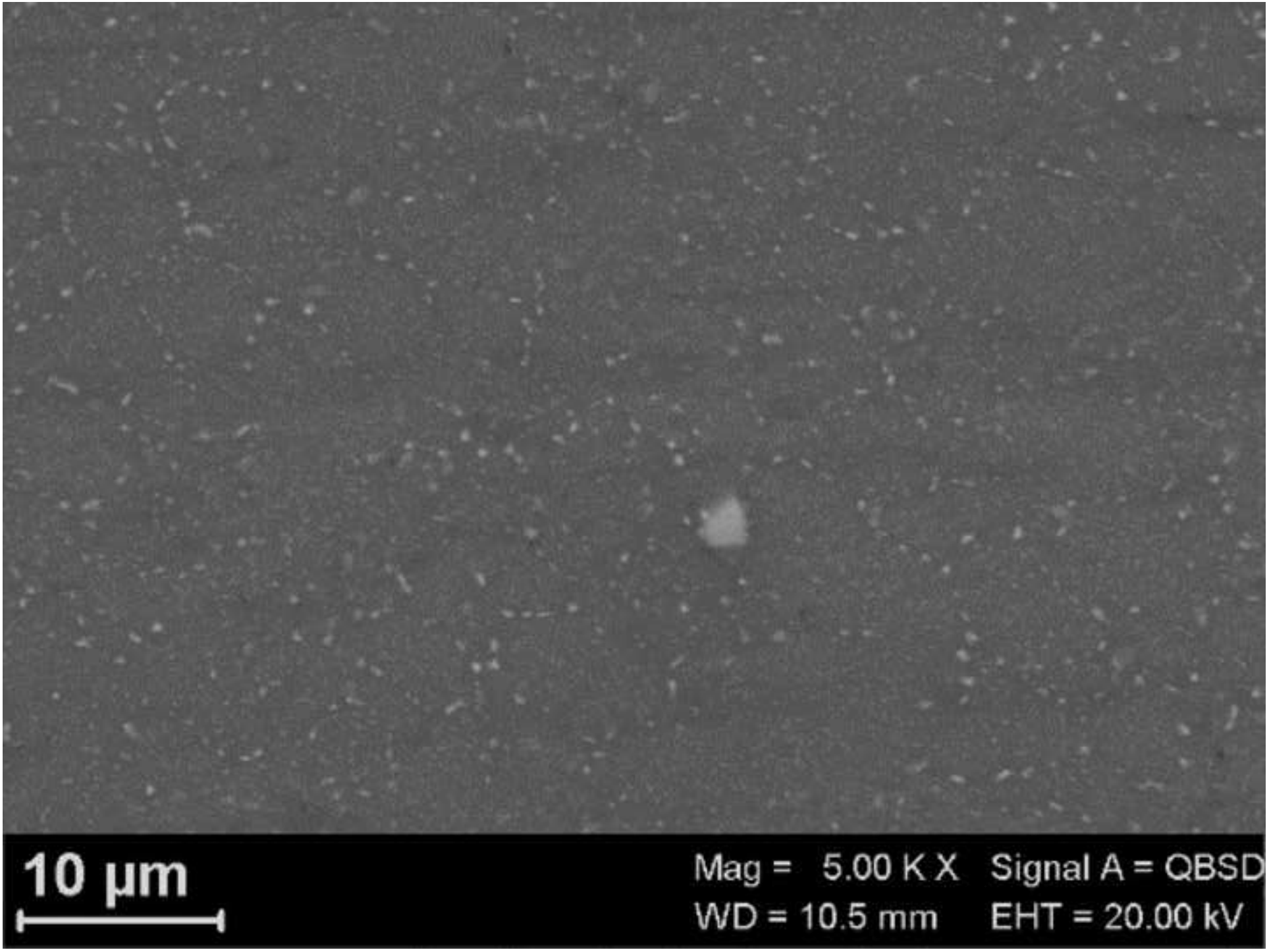

Figure 10a

Click here to download high resolution image

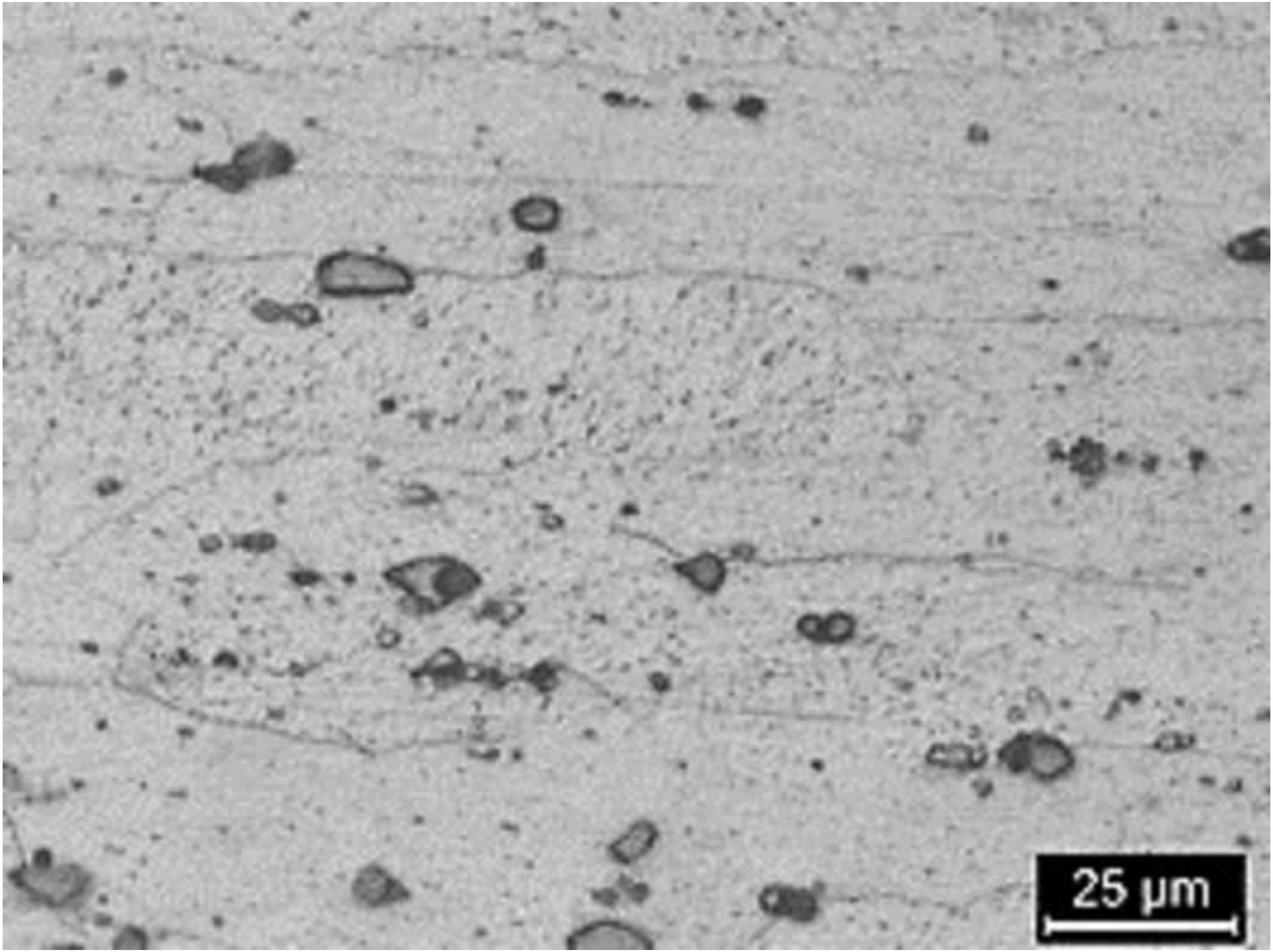

Figure 10b

Click here to download high resolution image

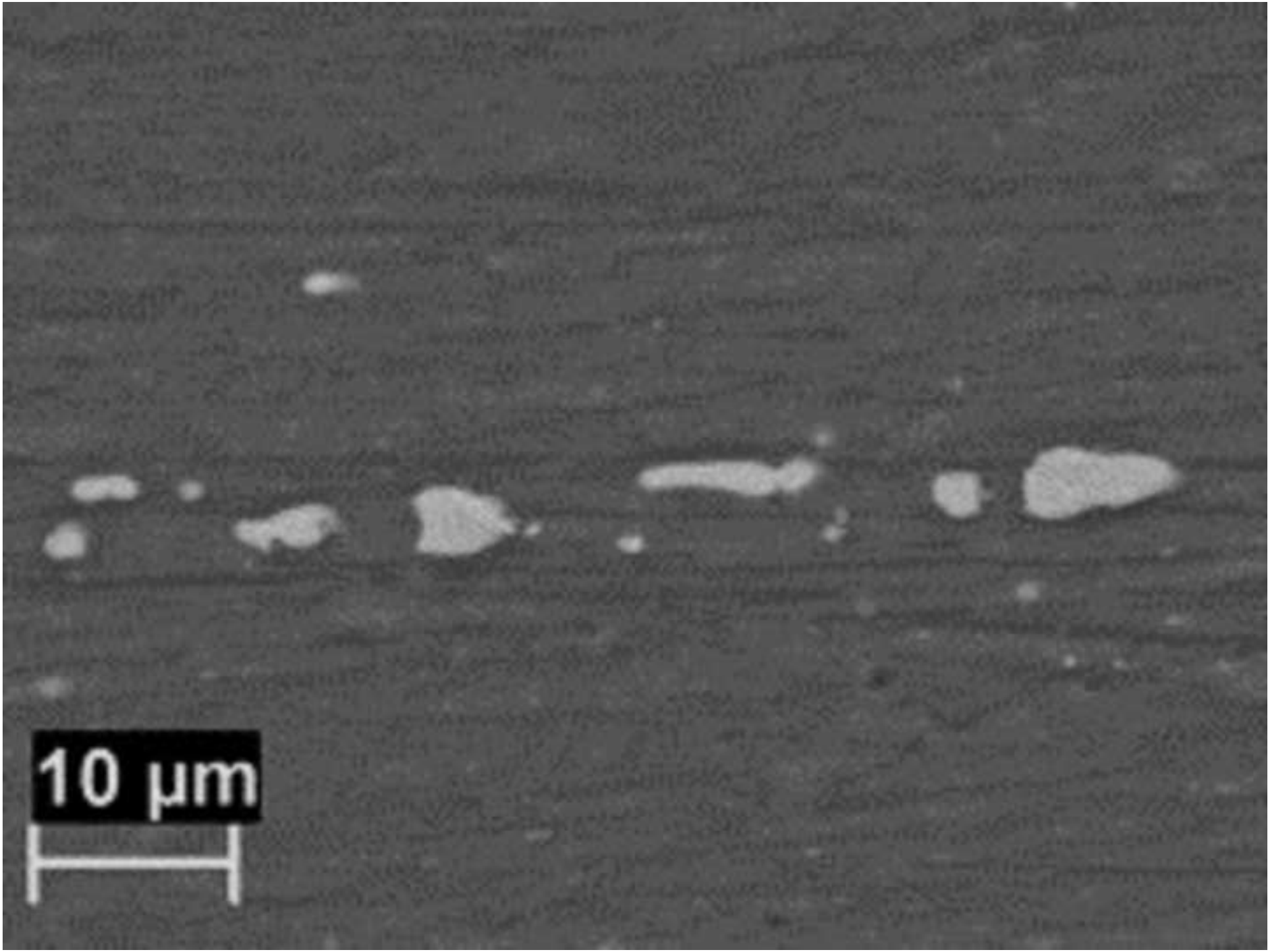

Figure 11a

Click here to download high resolution image

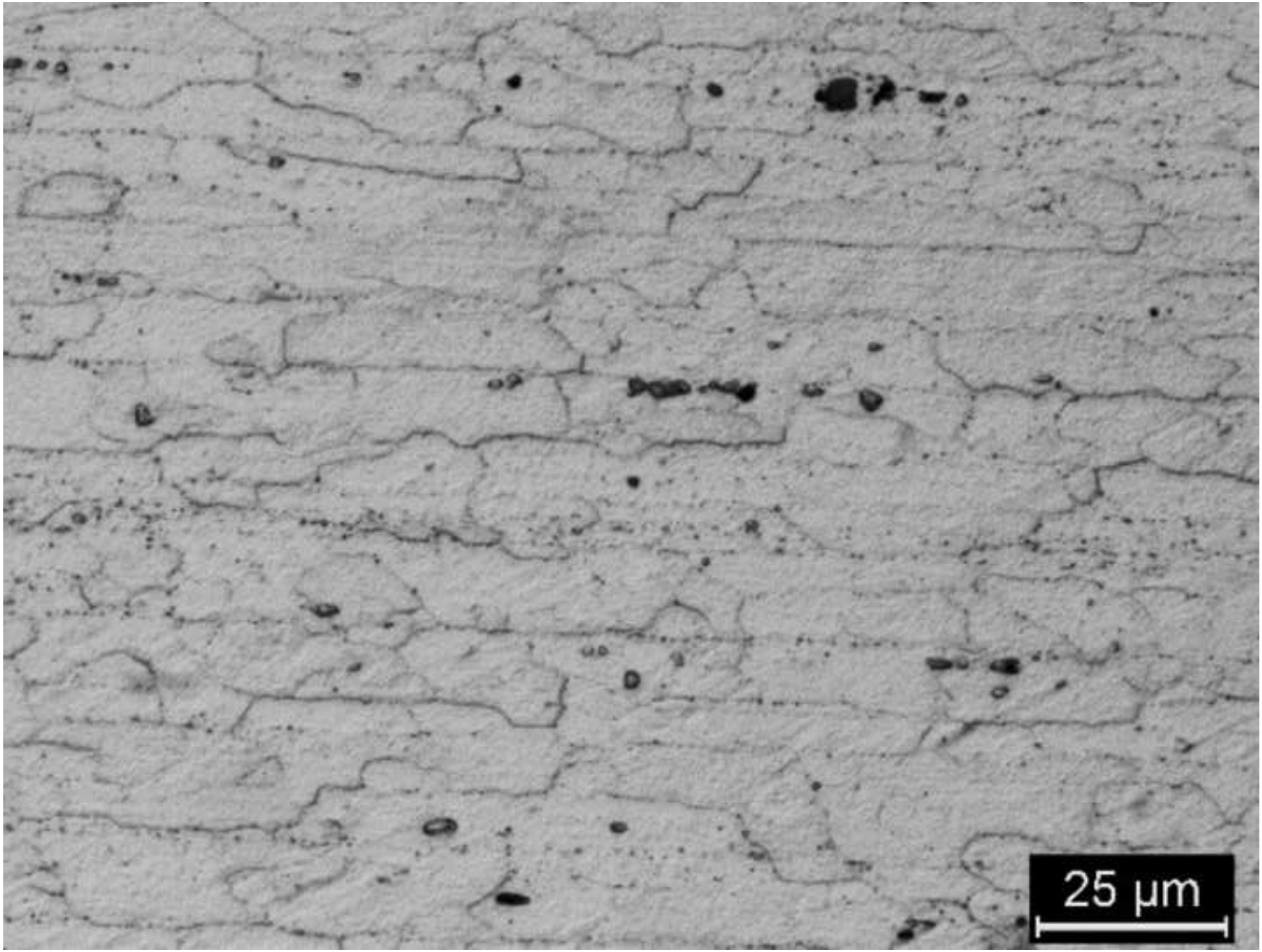

Figure 11b

Click here to download high resolution image

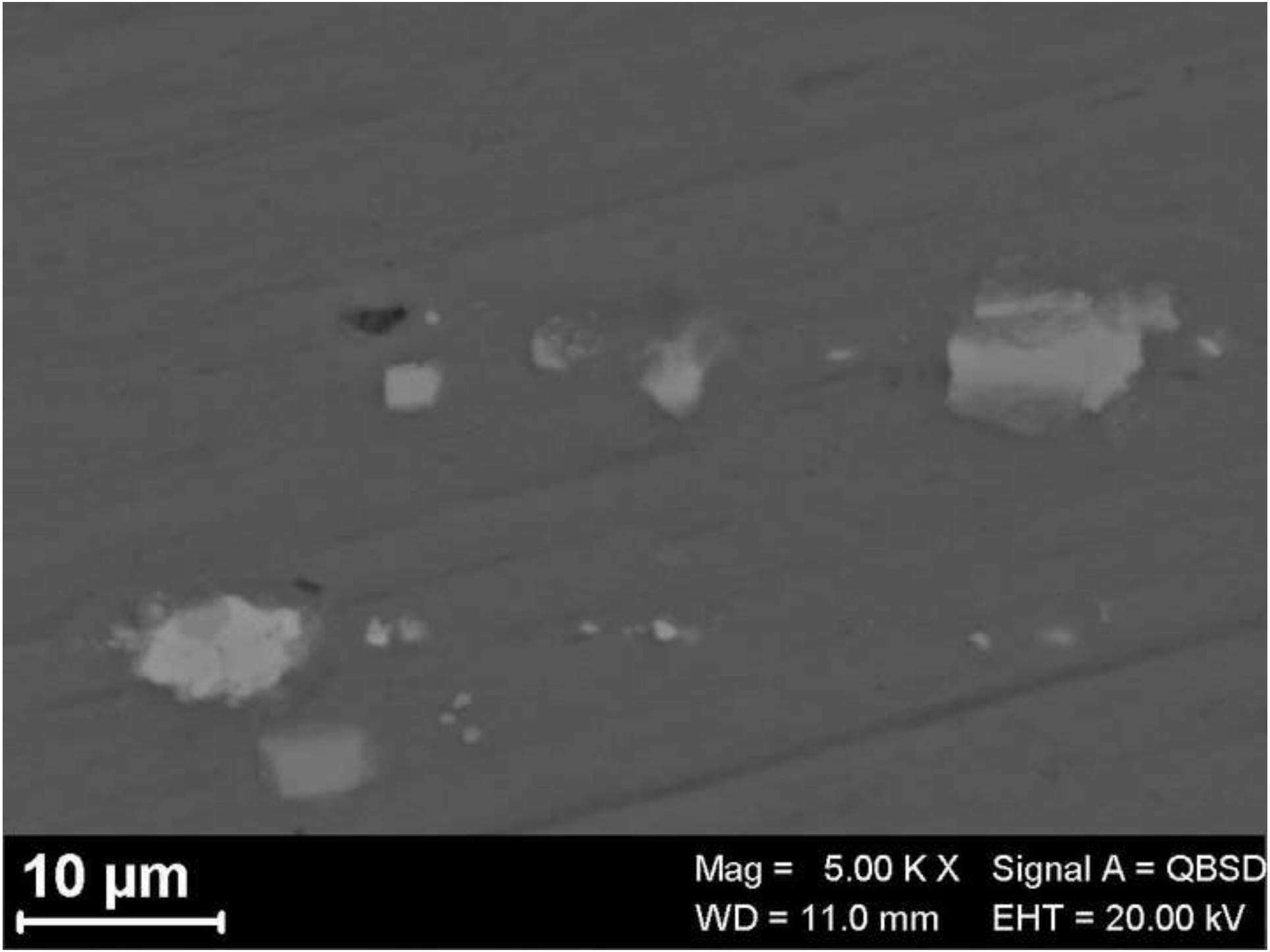

Figure 12

Click here to download high resolution image

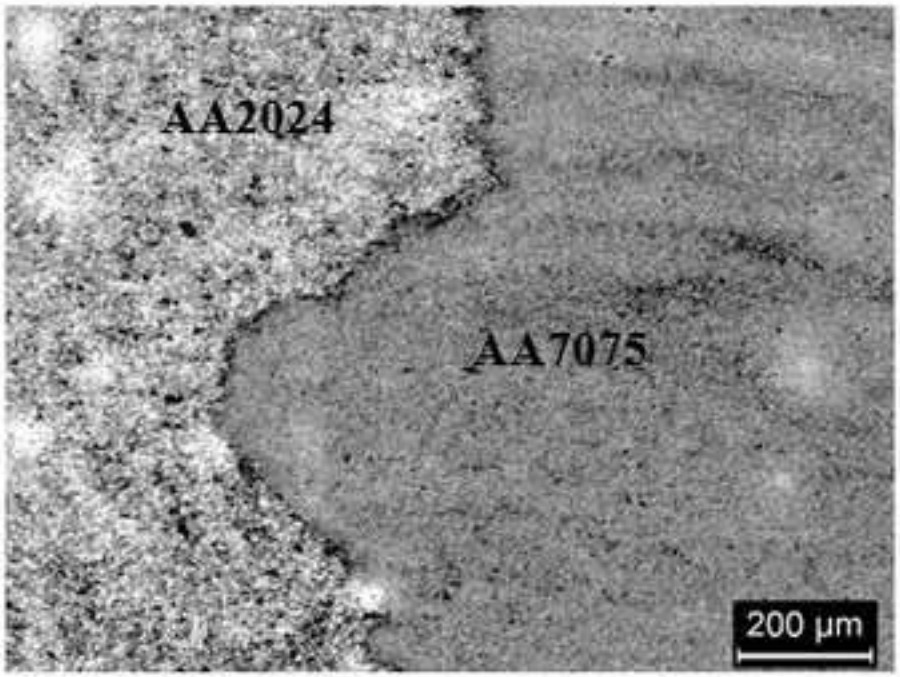

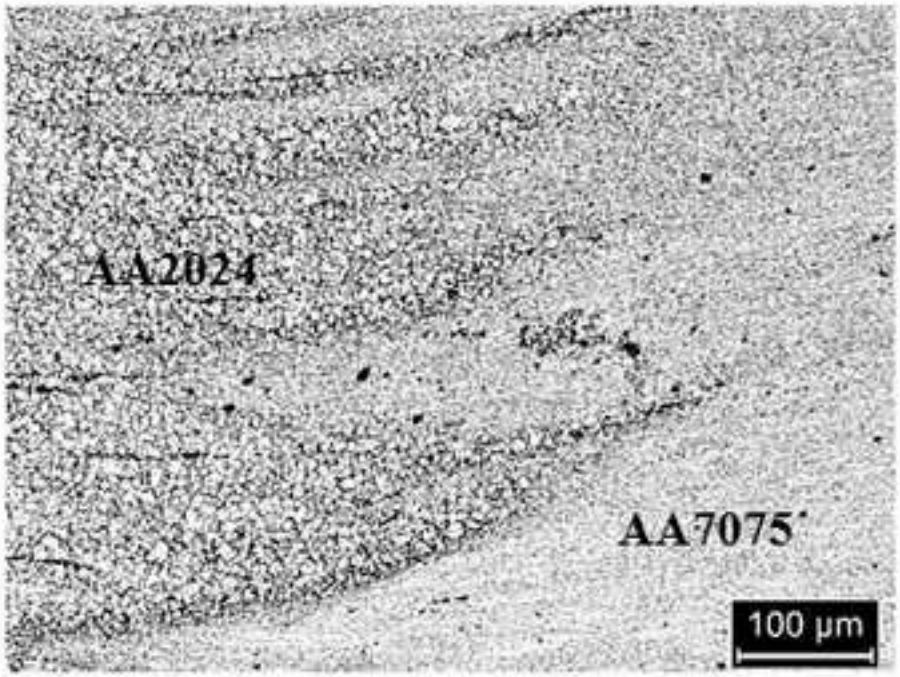

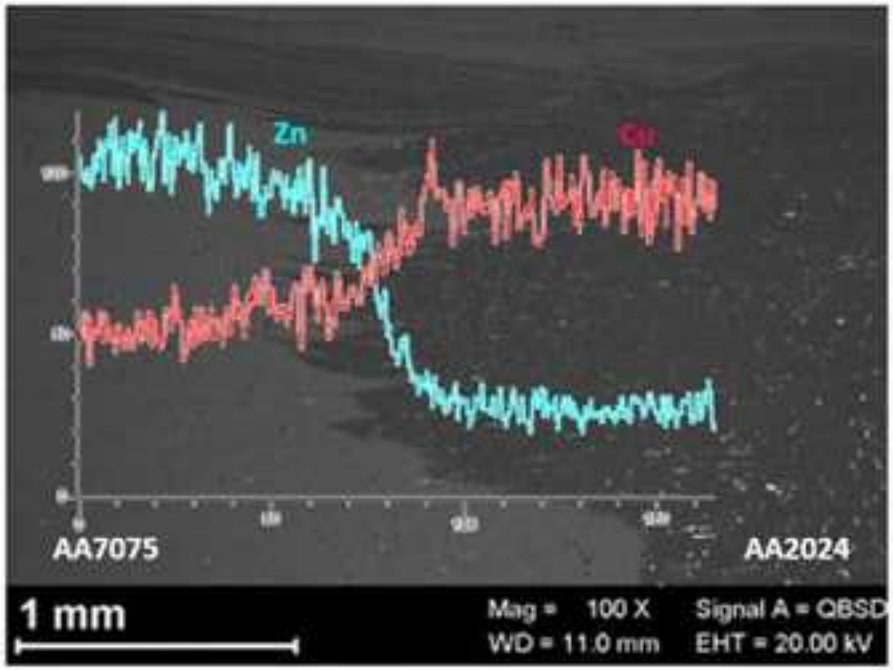

Figure 13

Click here to download high resolution image

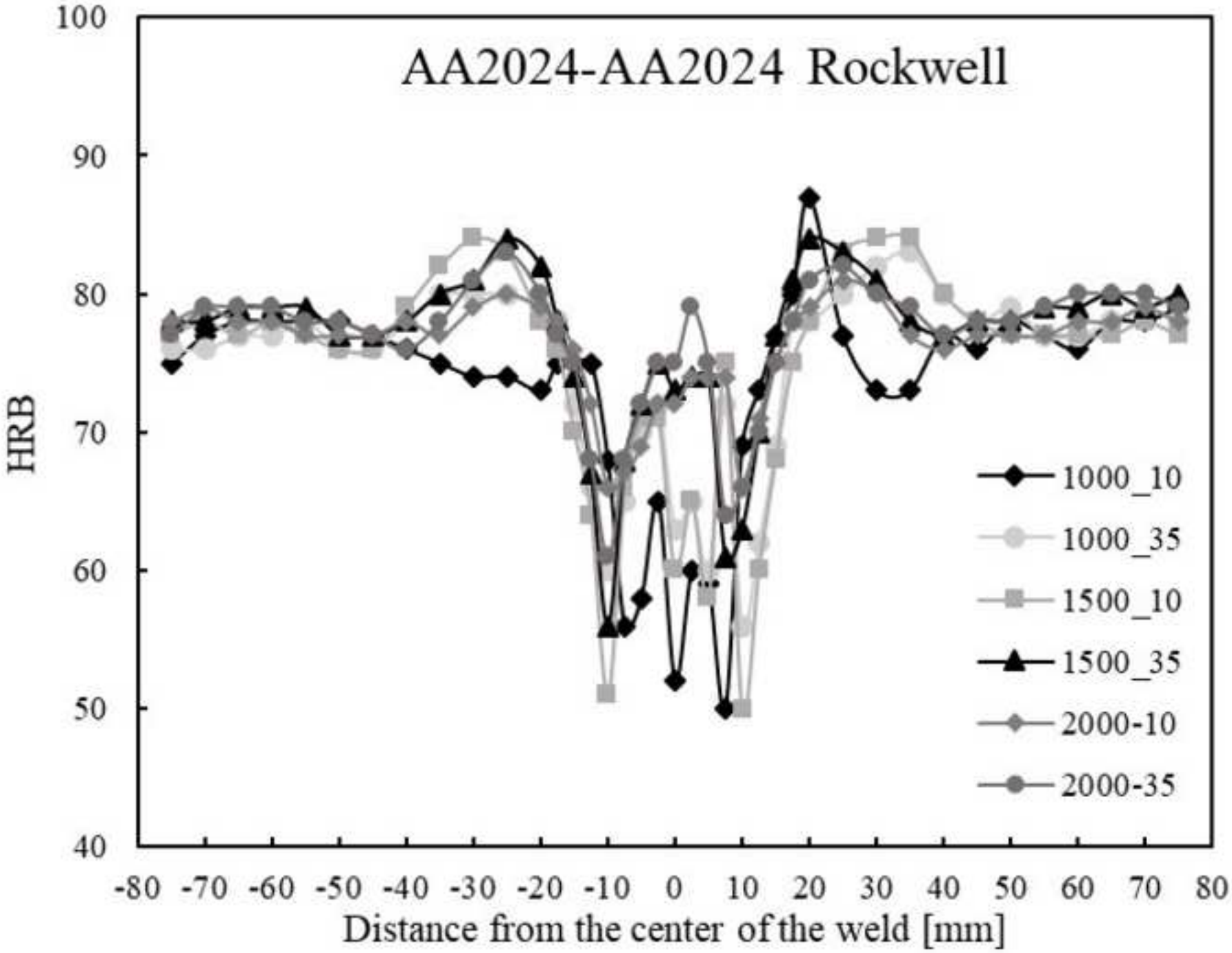

Figure 14

Click here to download high resolution image

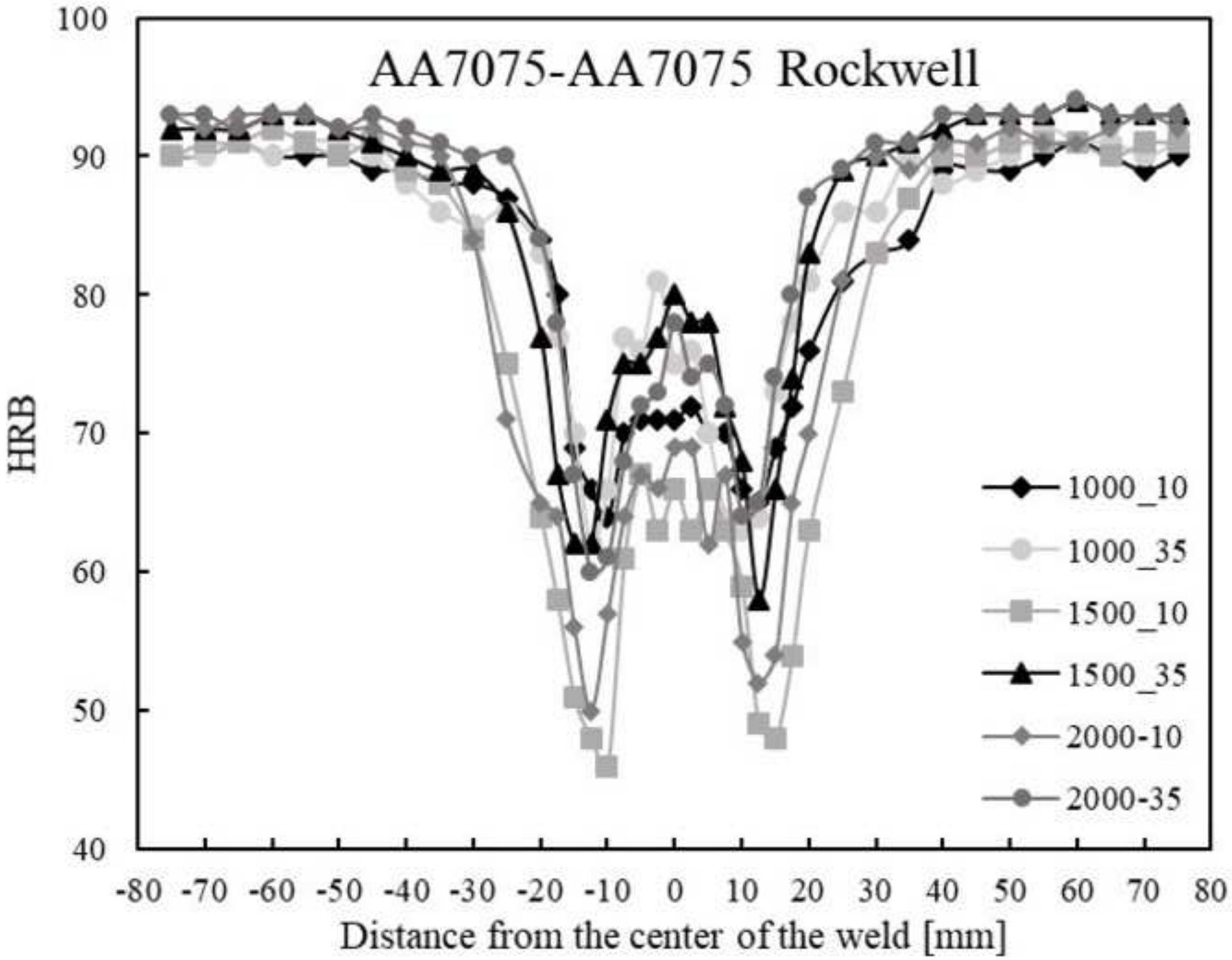

Figure 15

Click here to download high resolution image

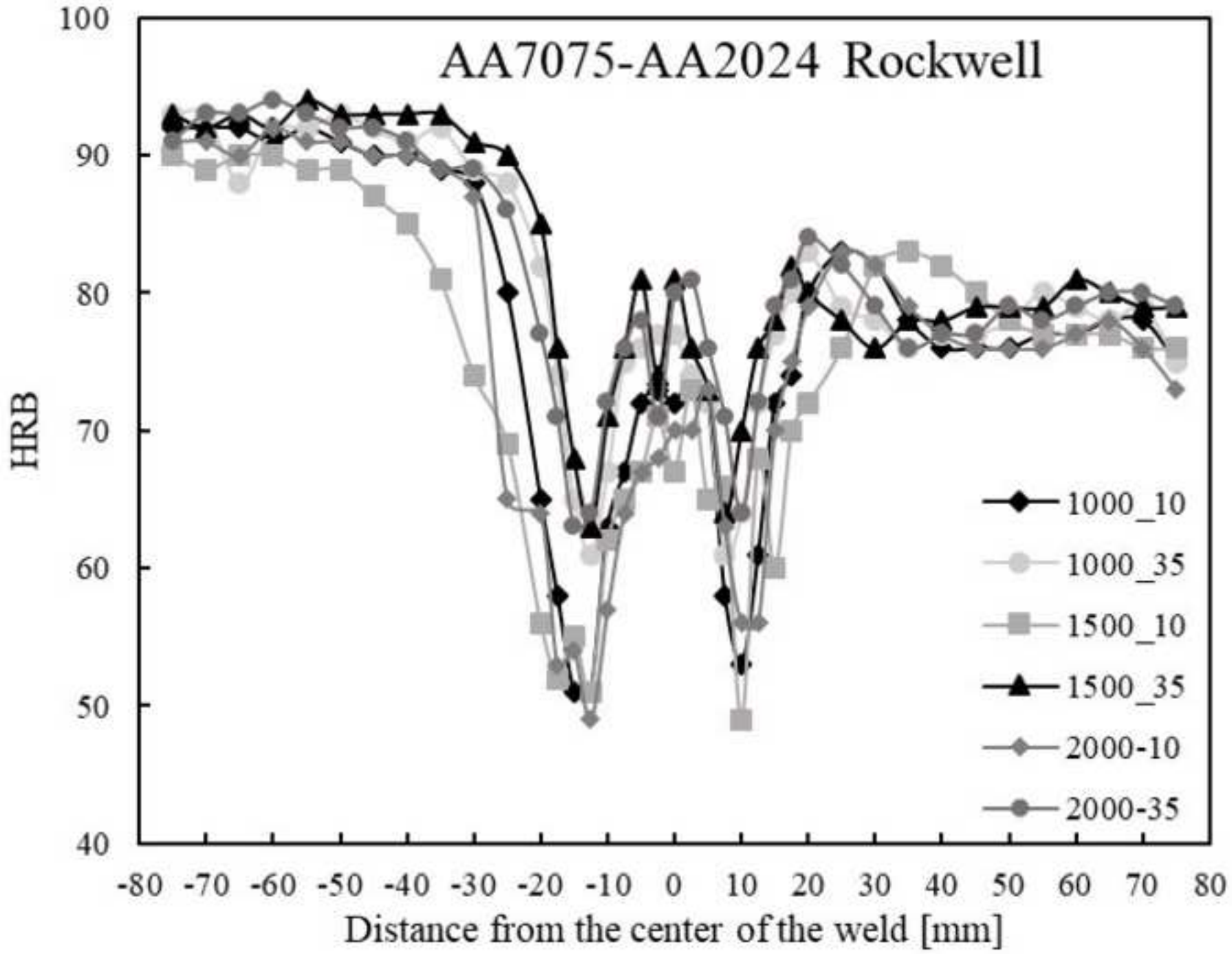

Figure 16

Click here to download high resolution image

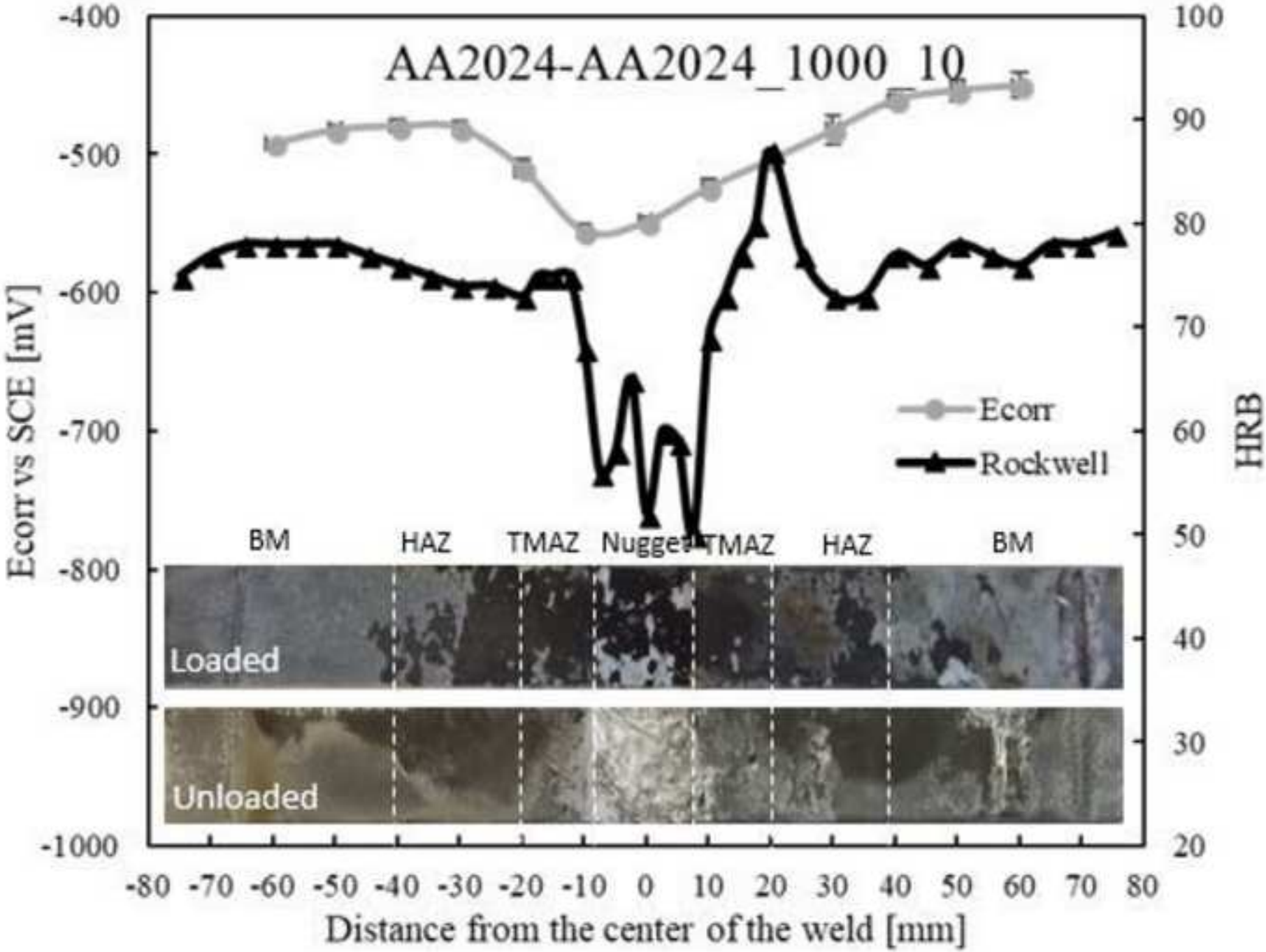

Figure 17

Click here to download high resolution image

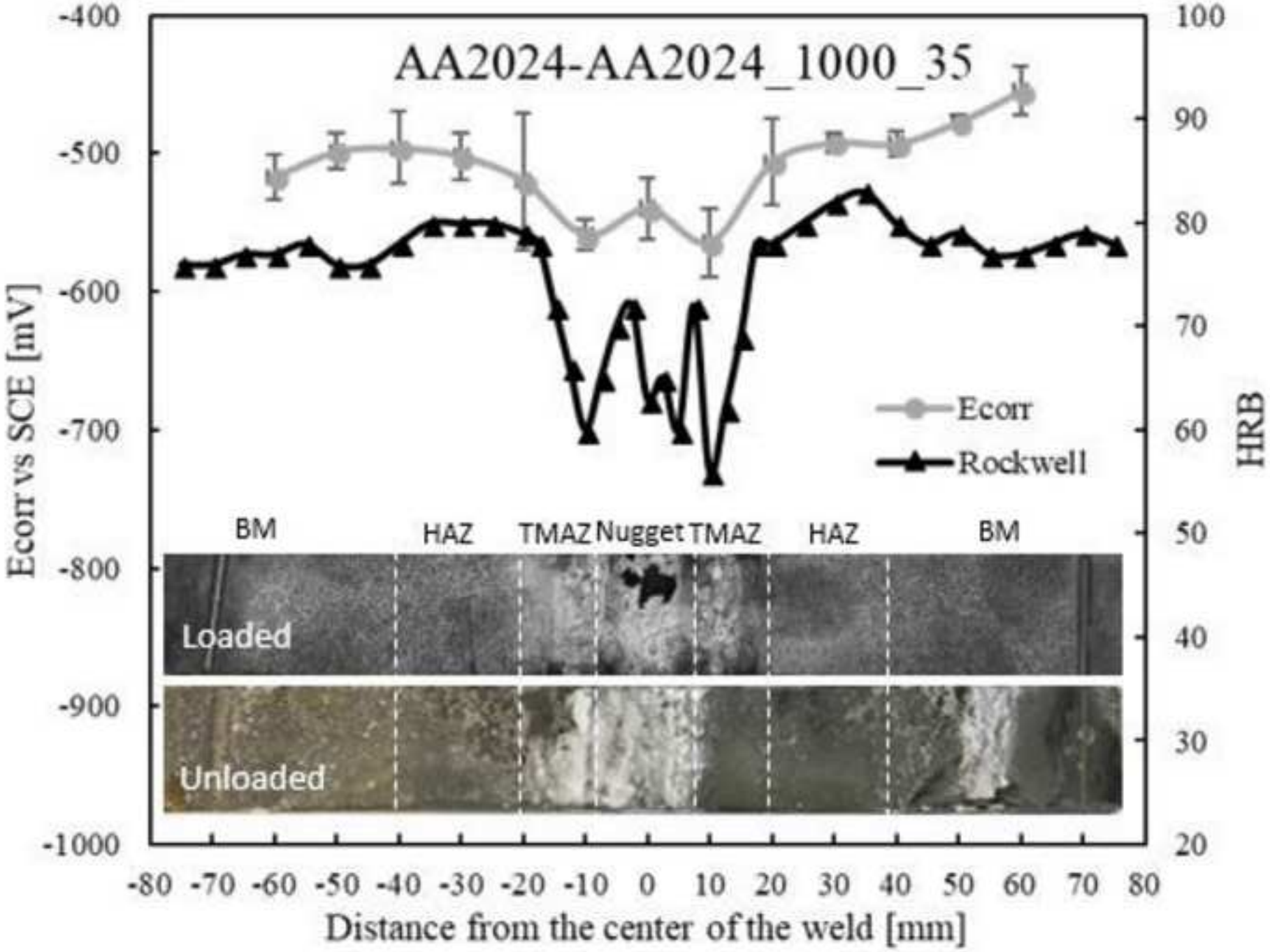

Figure 18

Click here to download high resolution image

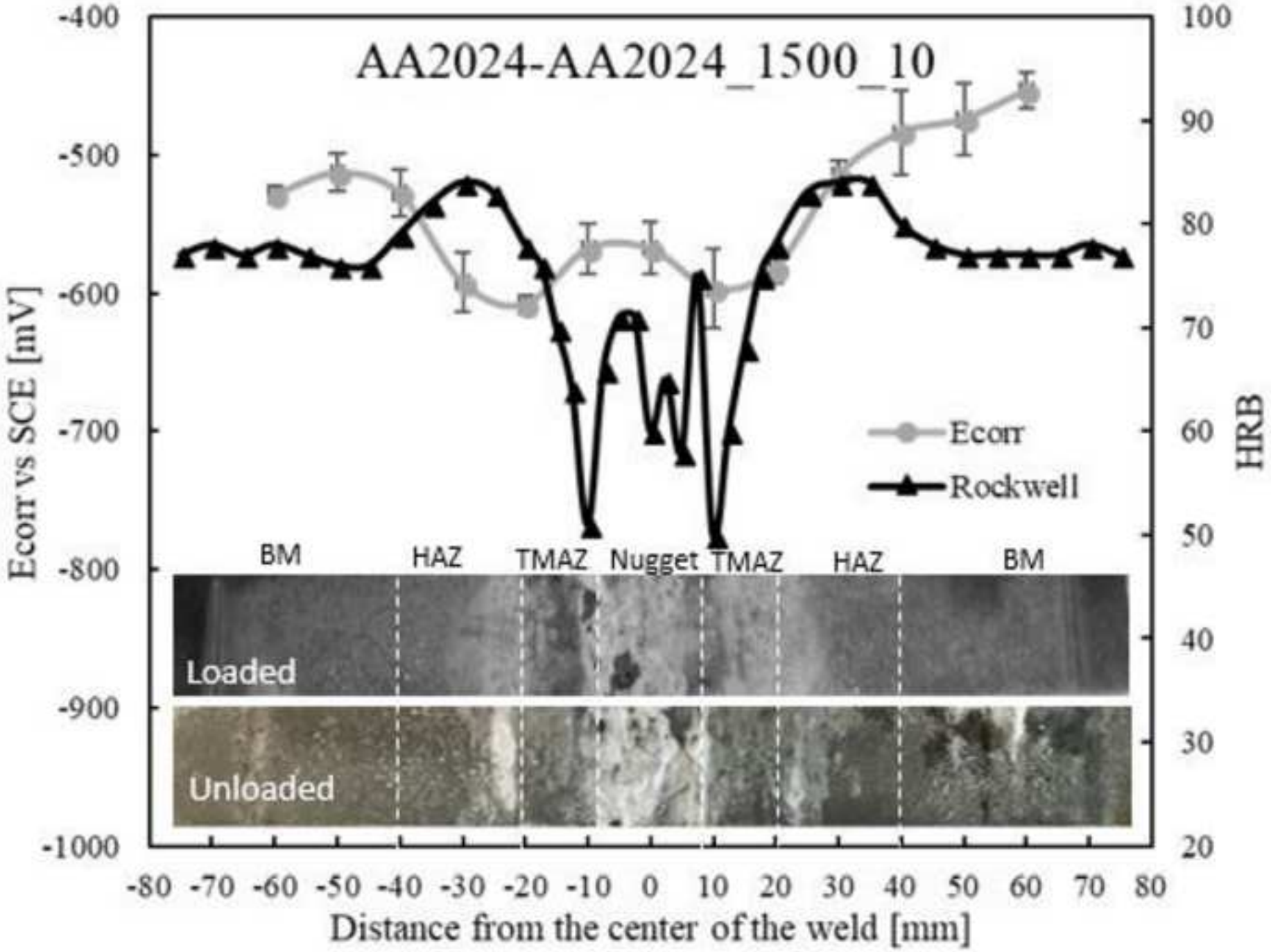

Figure 19

Click here to download high resolution image

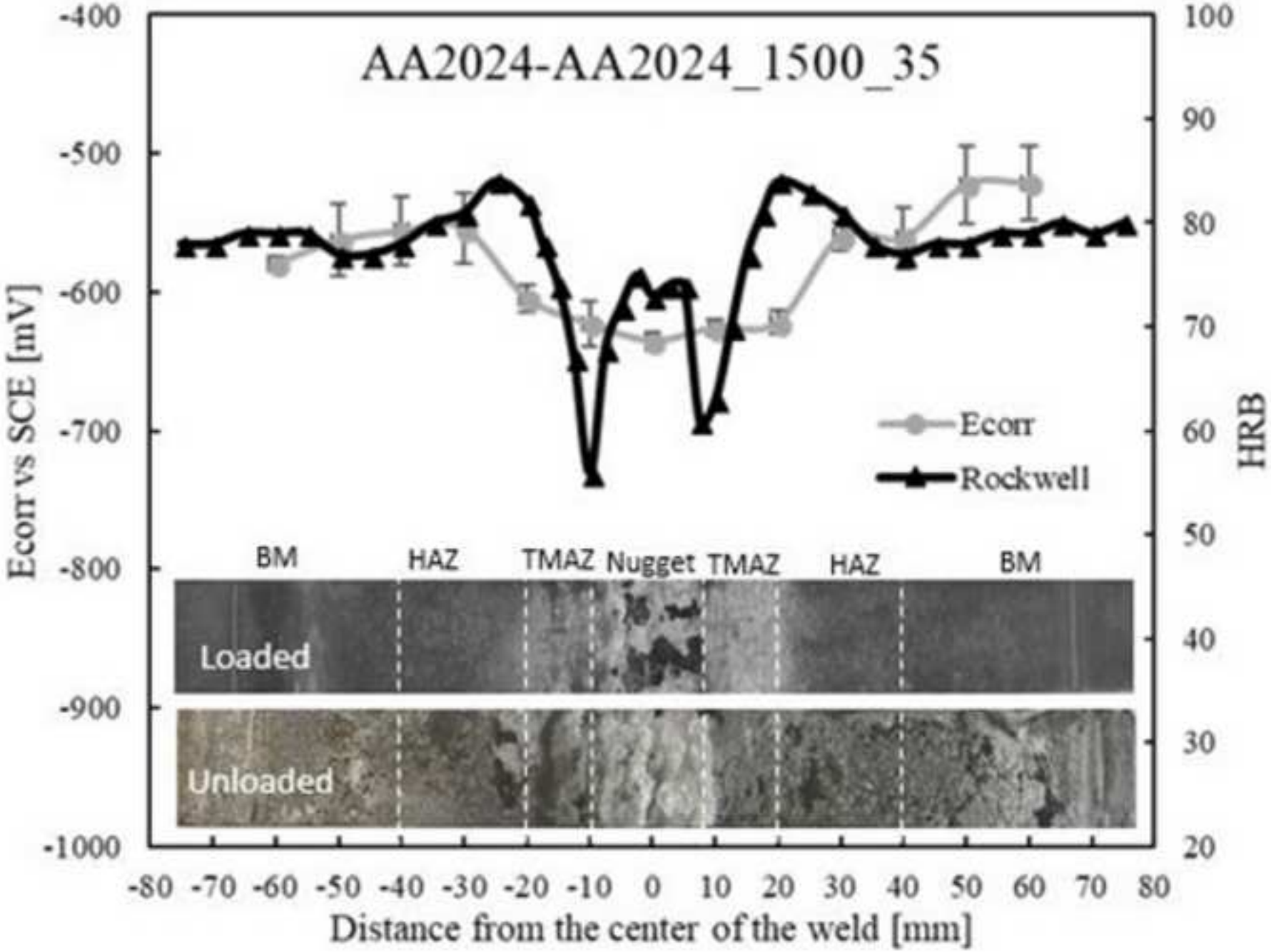

Figure 20

Click here to download high resolution image

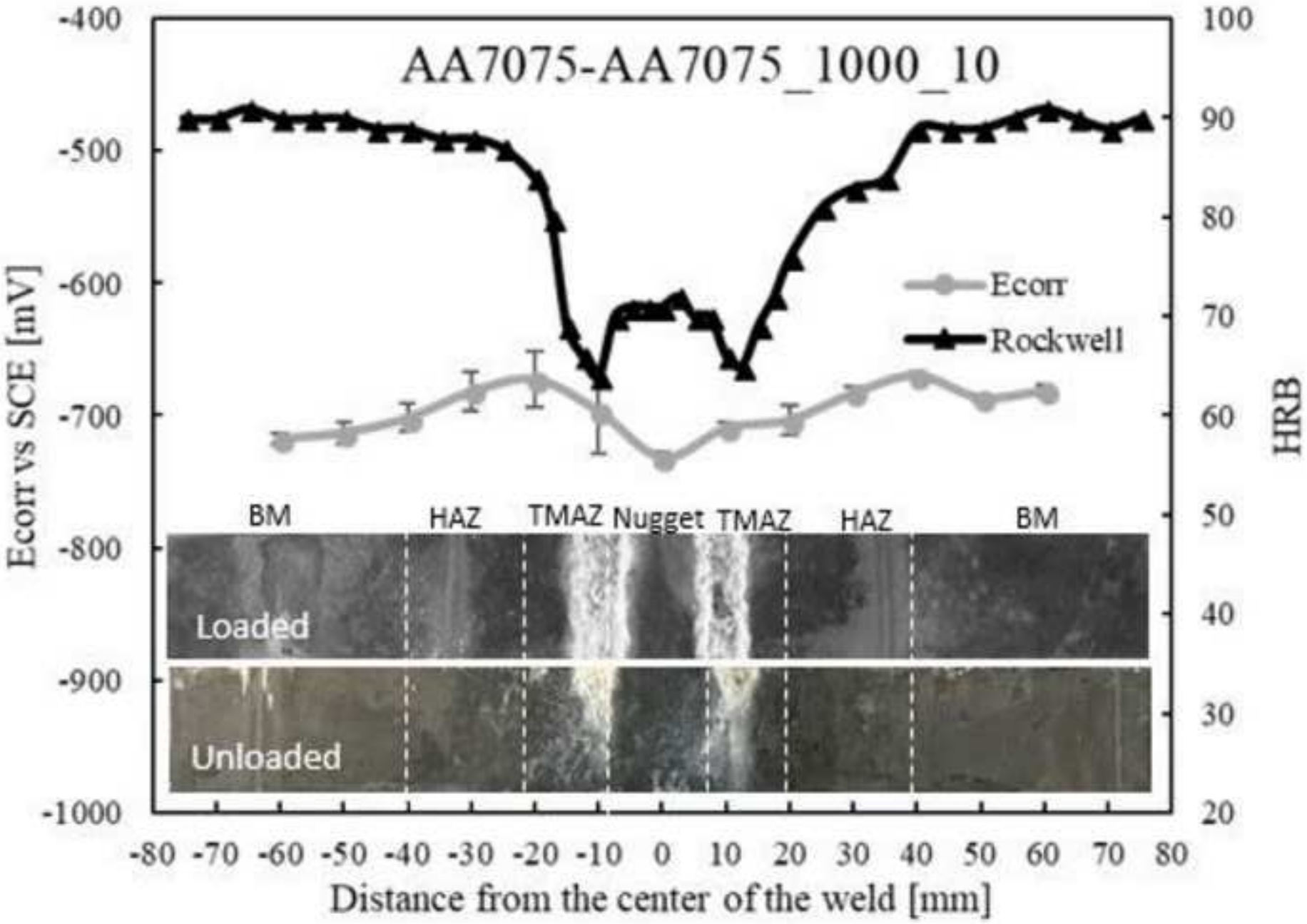

Figure 21

Click here to download high resolution image

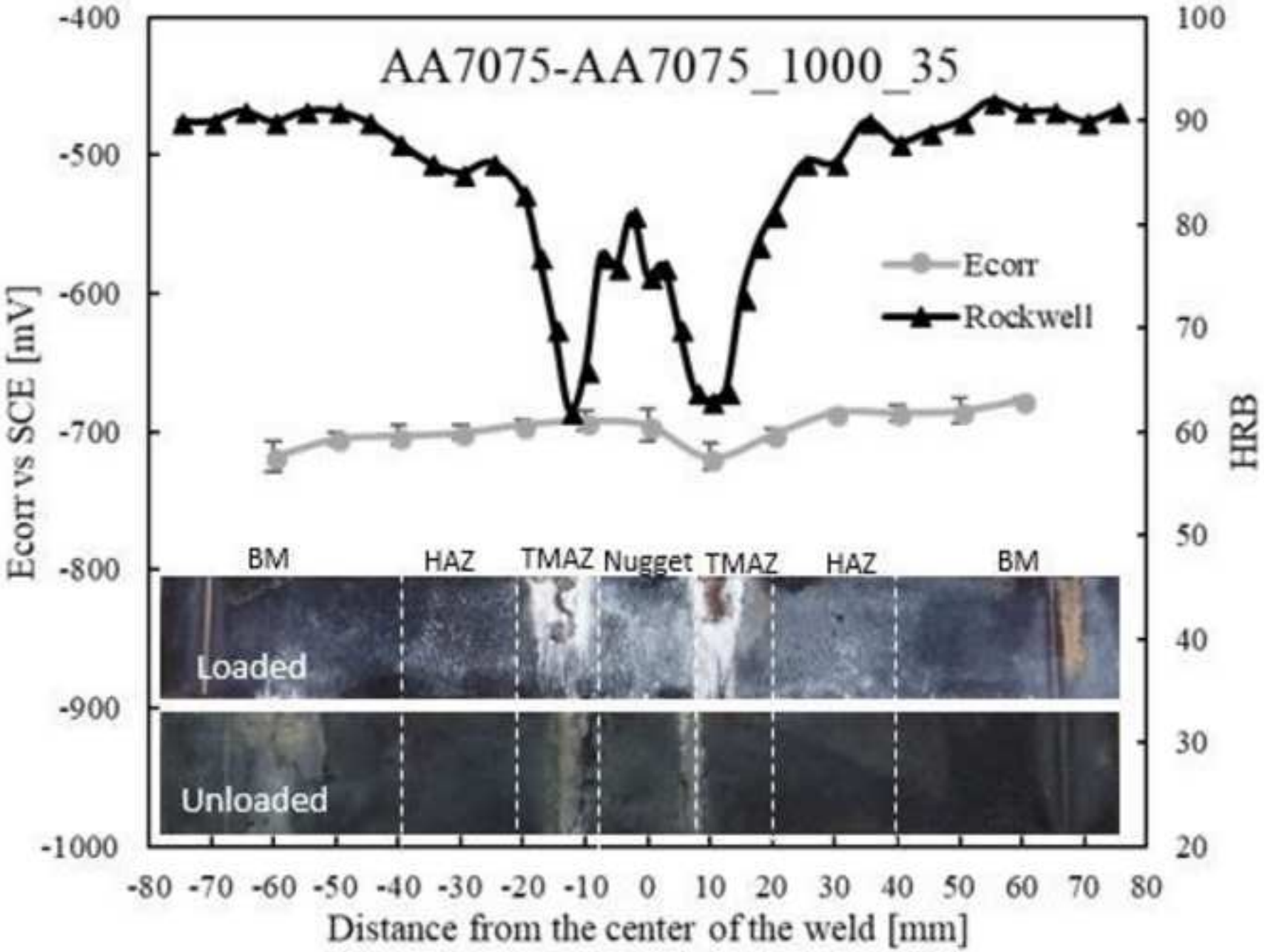

Figure 22

Click here to download high resolution image

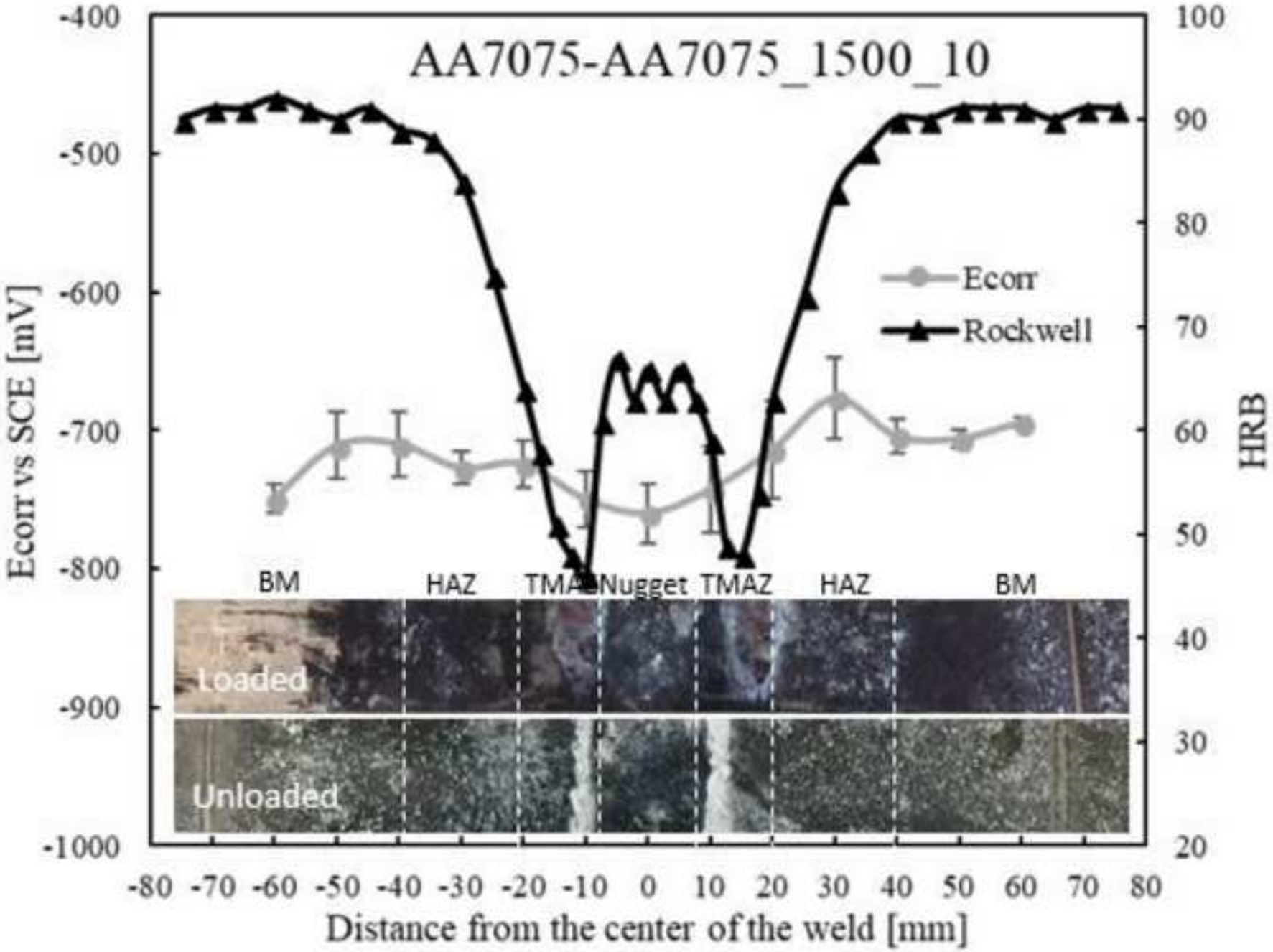

Figure 23

Click here to download high resolution image

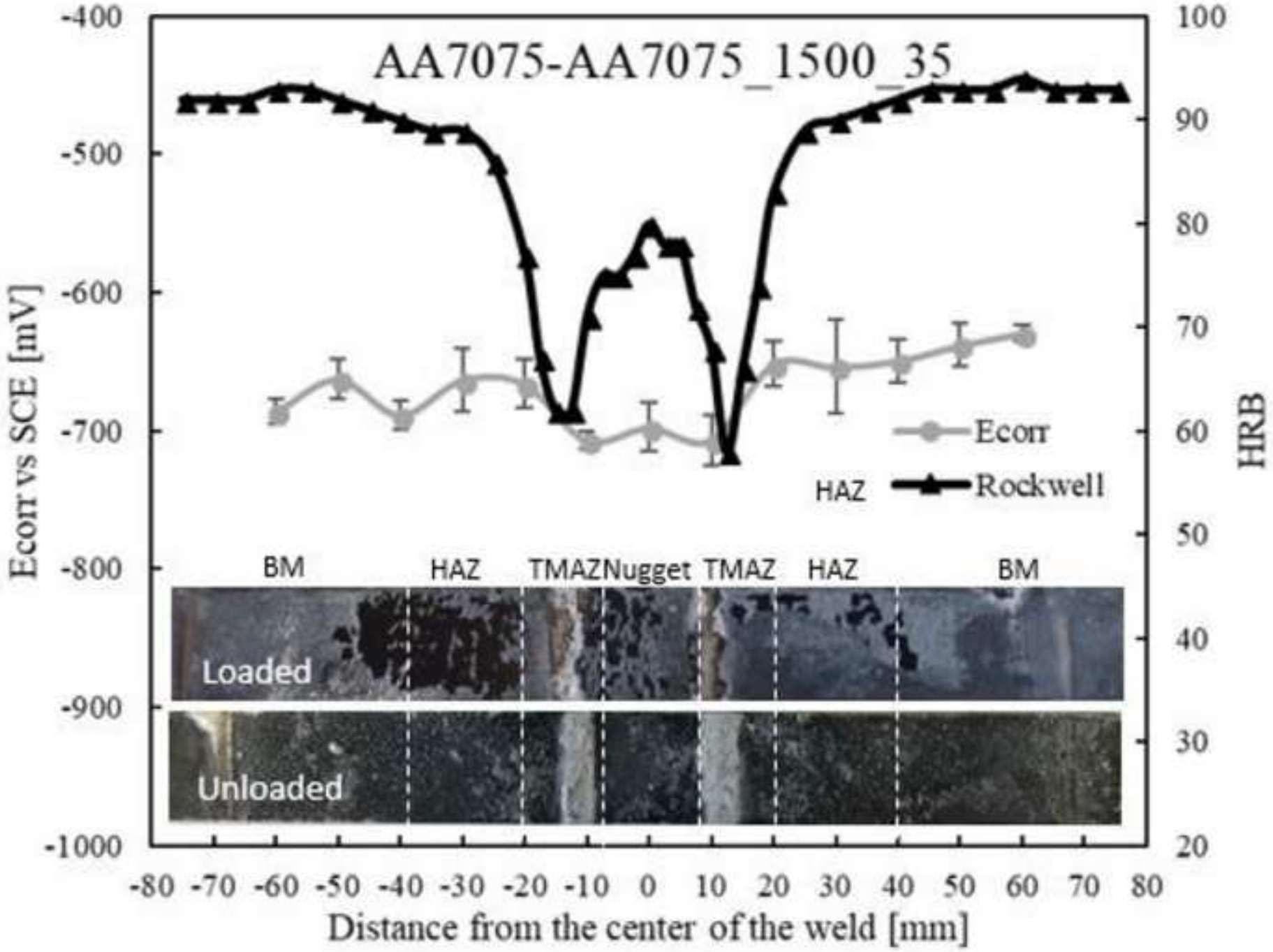

Figure 24

Click here to download high resolution image

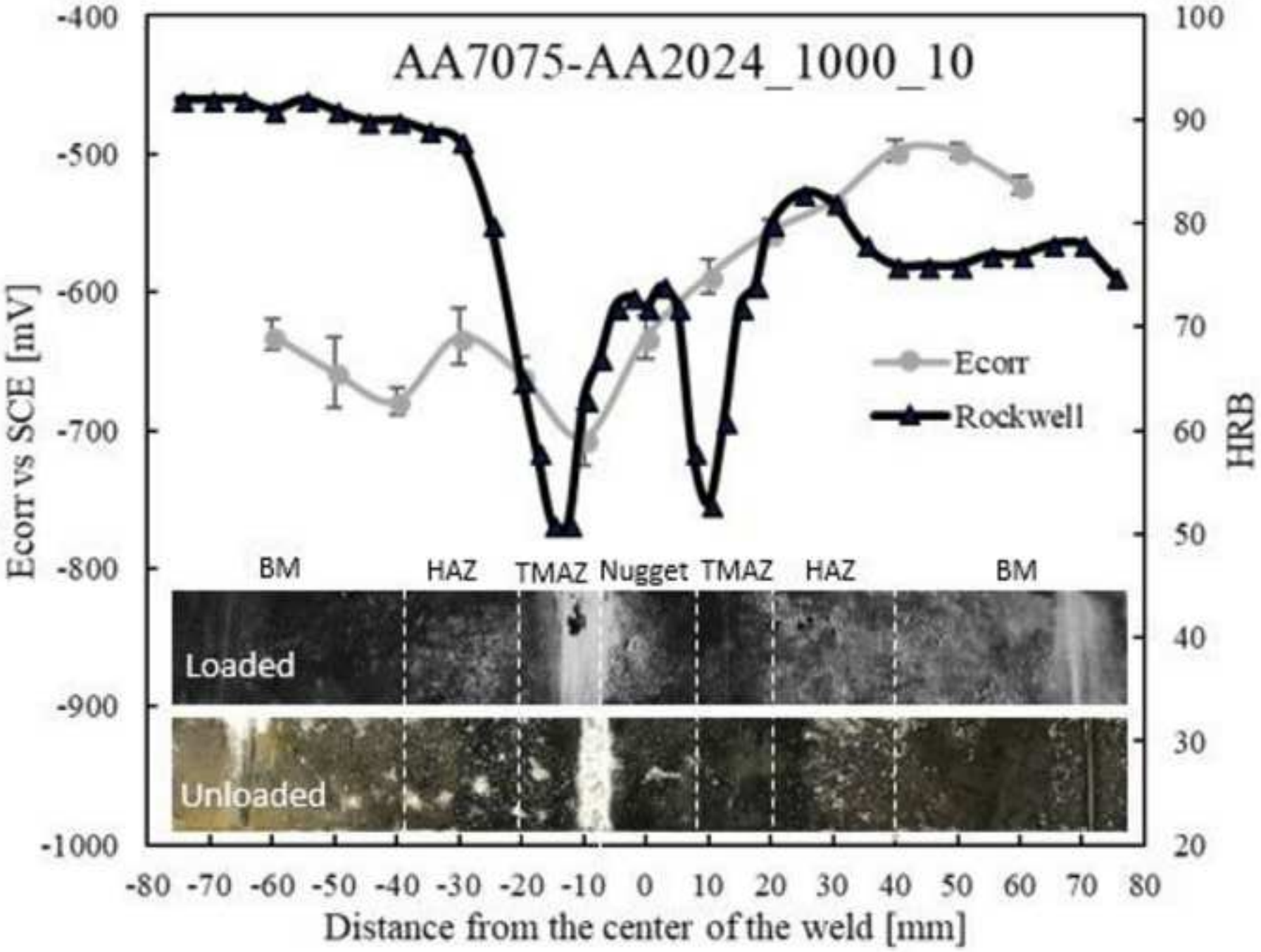

Figure 25

Click here to download high resolution image

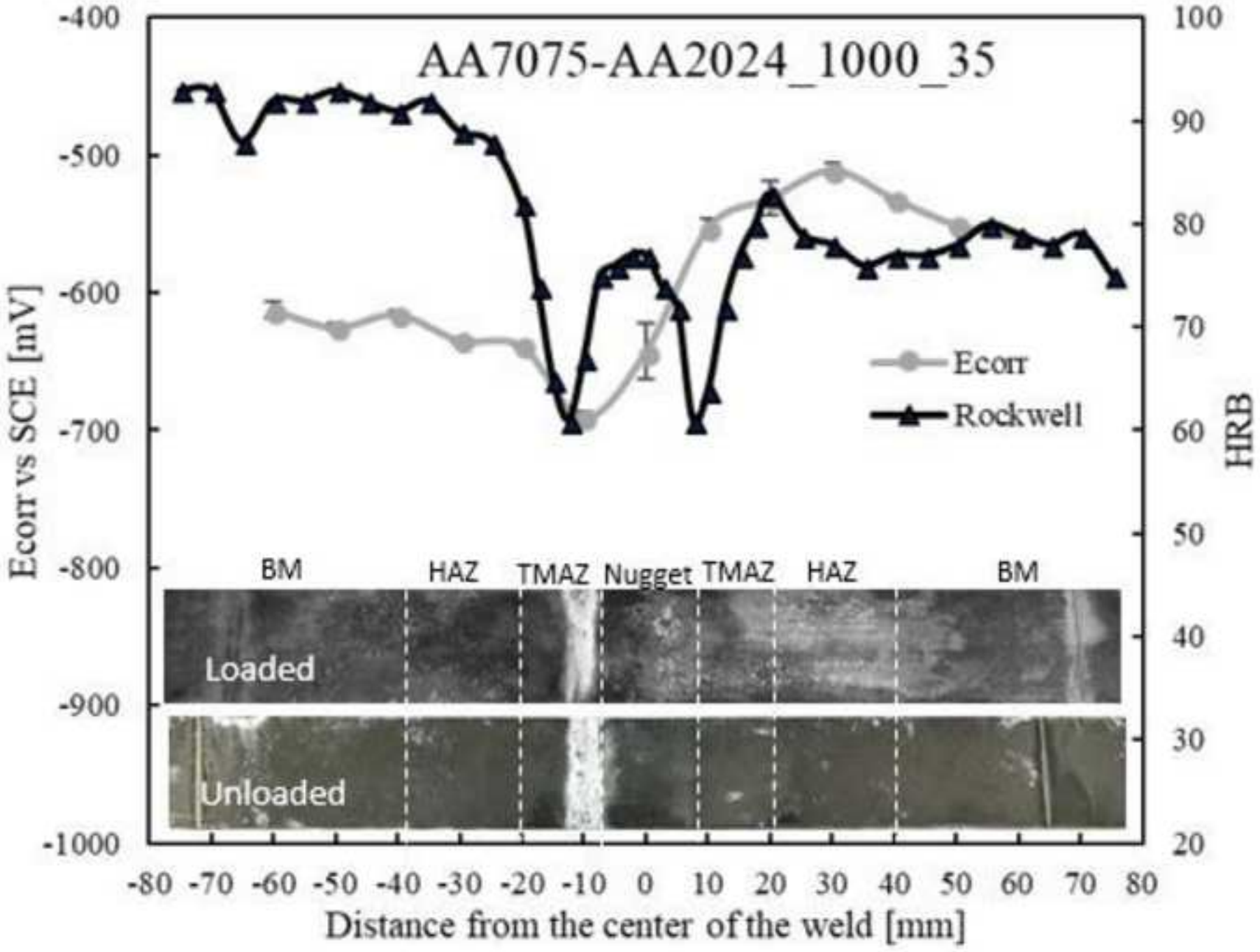

Figure 26

Click here to download high resolution image

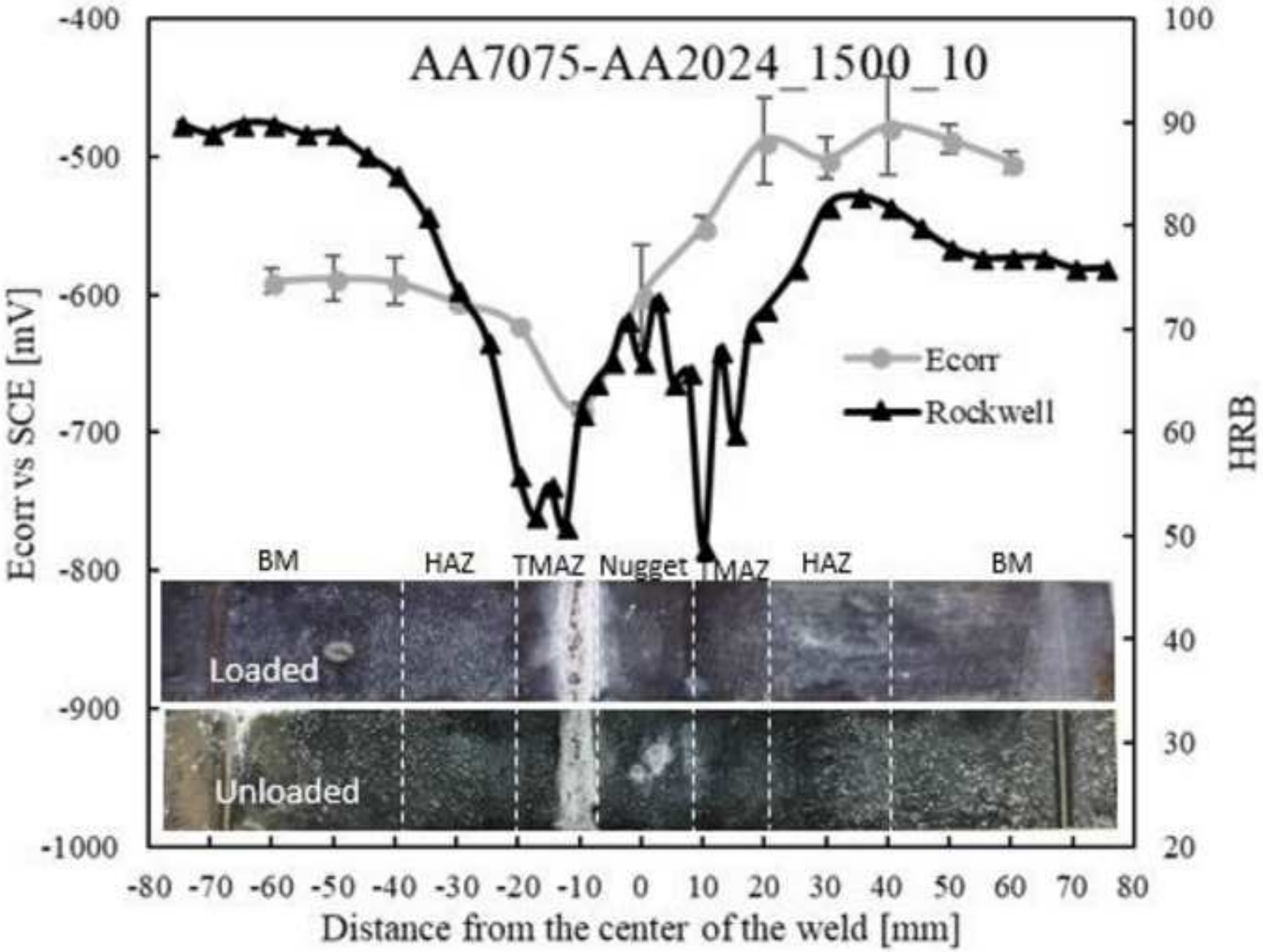

Figure 27
Click here to download high resolution image

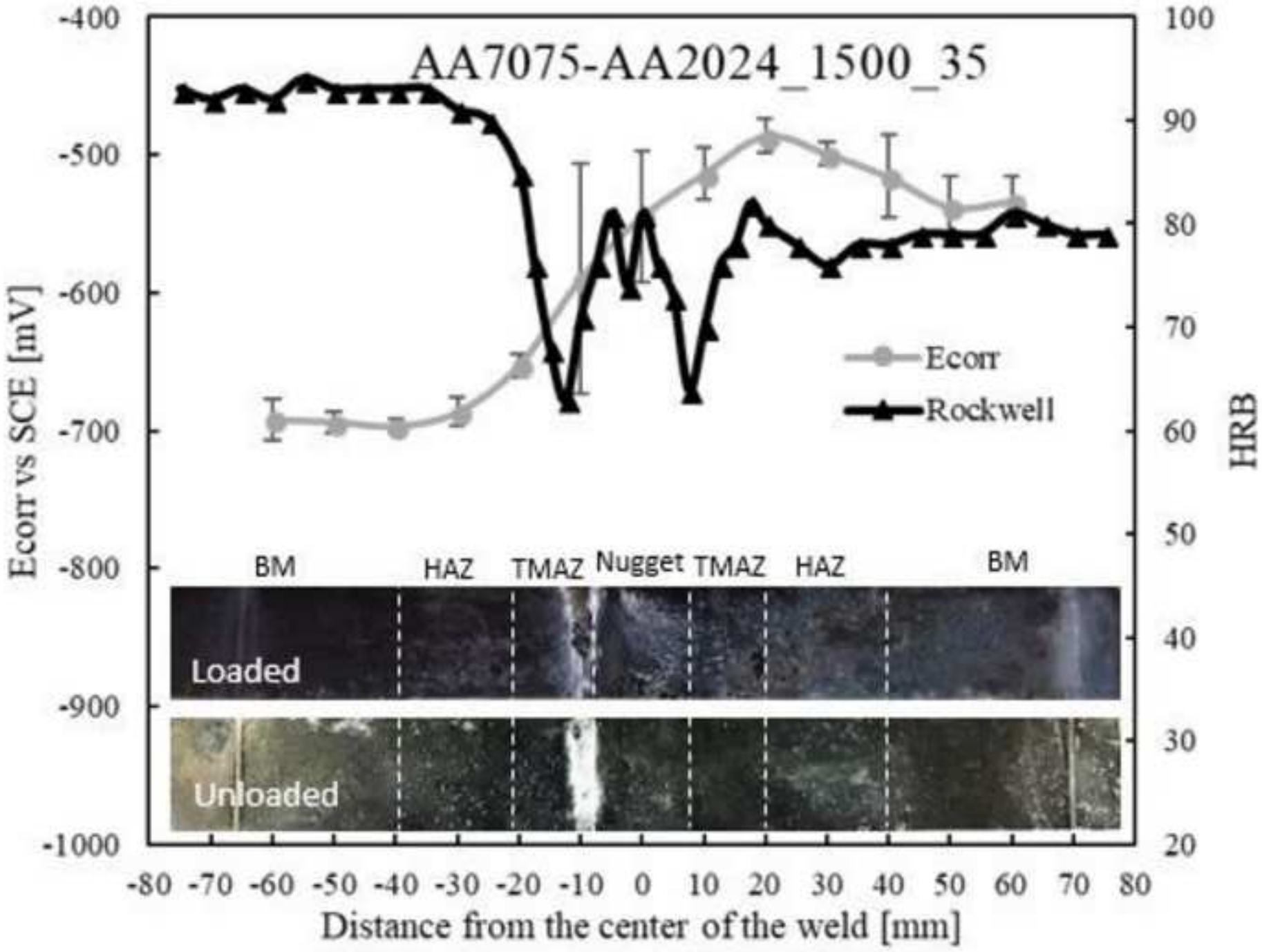

Figure 28

Click here to download high resolution image

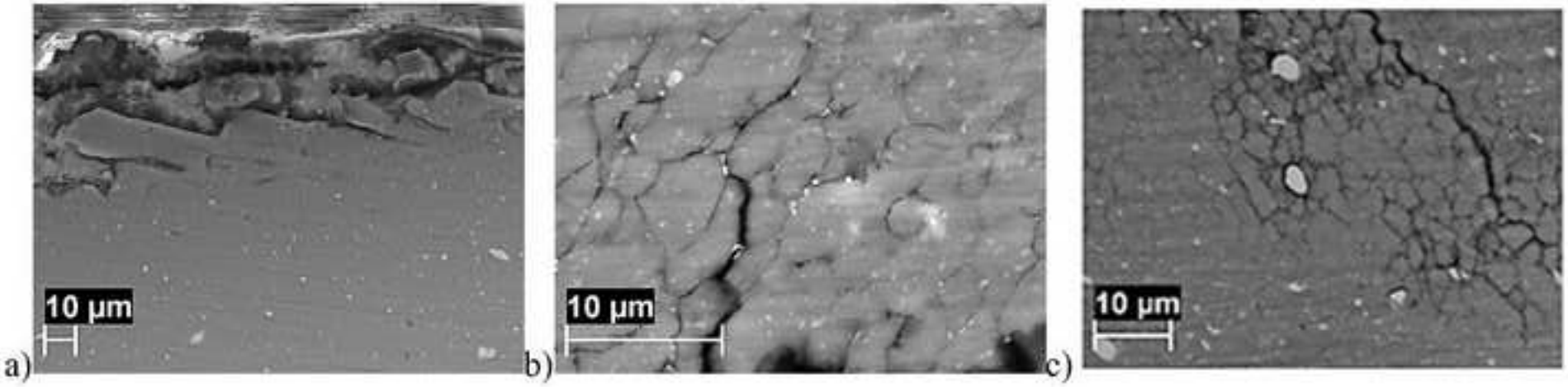

Figure 29

Click here to download high resolution image

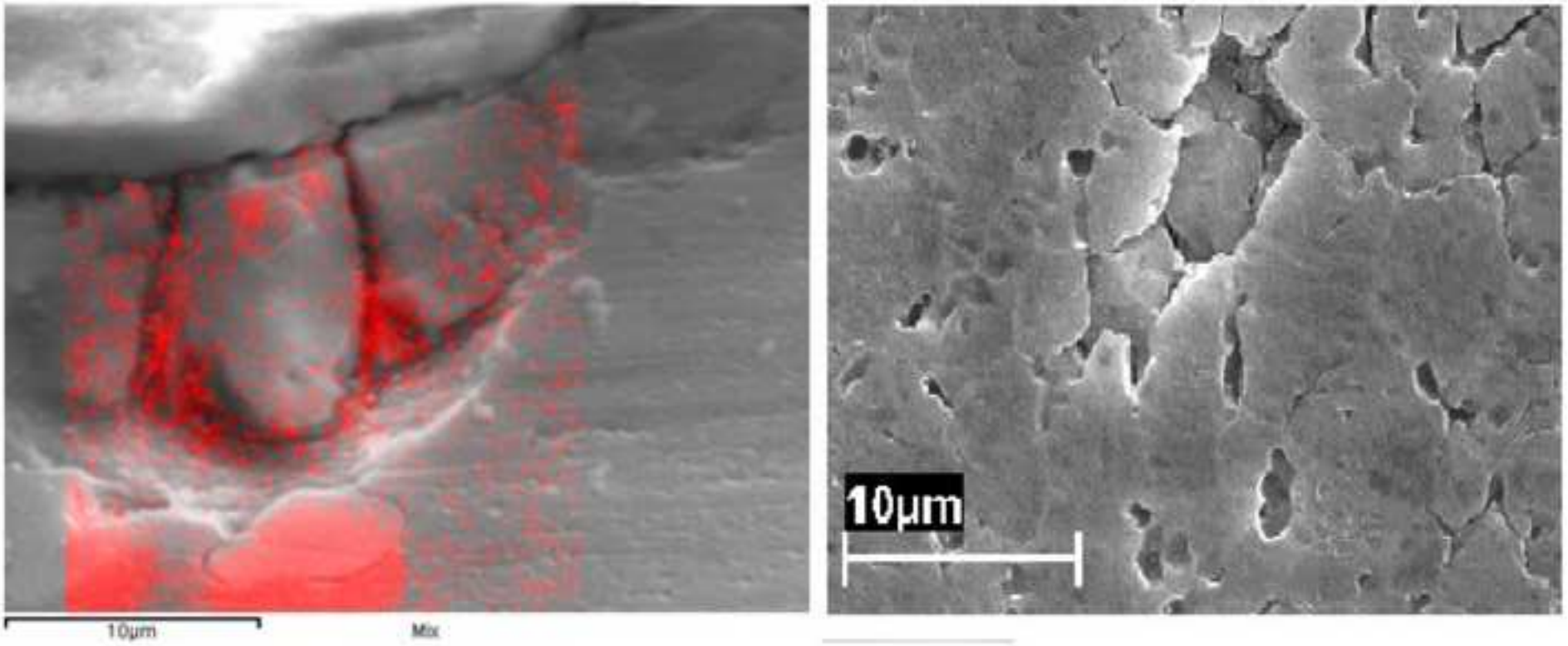

Figure 30

Click here to download high resolution image

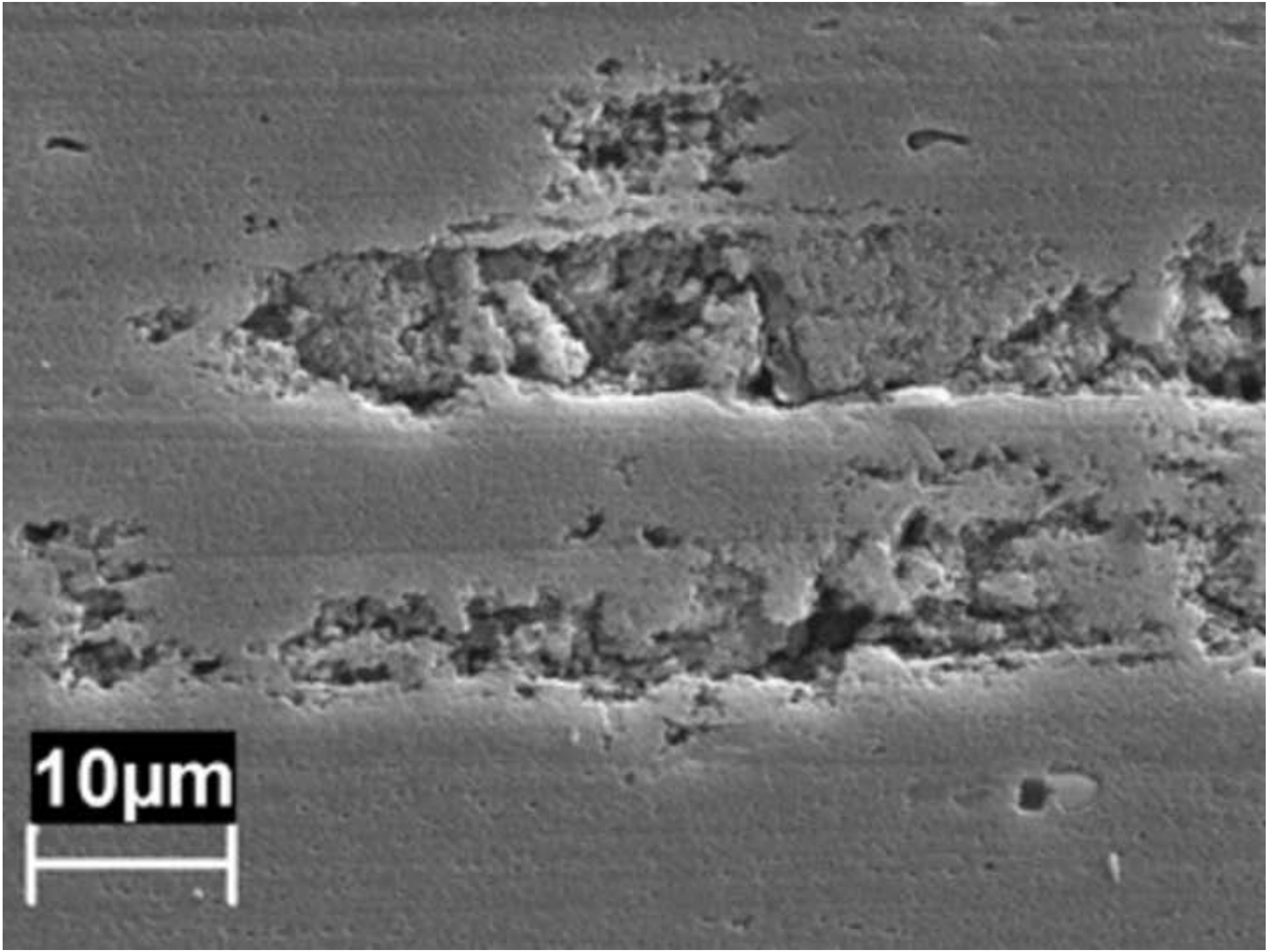

Table 1

Click here to download high resolution image

Cu	Mg	Si	Fe	Mn	Zn	Ti	Yield Strength (MPa)	UTS base material (MPa)	Elongation %
4.4	1.6	0.08	0.10	0.48	0.1	0.04	345	459	17

Table 2

Click here to download high resolution image

Zn	Mg	Cu	Fe	Mn	Si	Cr	Ti	Yield StrengthYS (MPa)	UTS base material (MPa)	Elongation %
5.9	2.7	1.5	0.12	0.02	0.06	0.19	0.05	511	578	11

Table 3

Click here to download high resolution image

AA2024-AA2024					AA7075-AA7075					AA2024-AA7075				
S	f	UTS	St. Dev.	E %	S	f	UTS	St. Dev.	E %	S	f	UTS	St. Dev.	E %
1000	10	307.7	10.4	7.4	1000	10	378.3	8.8	15.0	1000	10	311.4	7.1	14.1
1000	35	325.8	33.4	5.3	1000	35	434.7	15.9	2.2	1000	35	345.2	12.4	2.0
1000	60	229.0	27.6	3.5	1000	60	322.1	28.8	6.0	1000	60	301.0	10.3	12.4
1500	10	317.0	3.0	10.7	1500	10	360.8	14.6	15.4	1500	10	271.3	20.0	12.8
1500	35	358.0	24.3	10.3	1500	35	426.0	10.6	13.6	1500	35	318.5	27.9	10.5
1500	60	304.9	4.5	5.1	1500	60	272.8	15.7	4.9	1500	60	282.5	34.0	4.7
2000	10	320.0	15.1	10.3	2000	10	296.4	13.3	13.2	2000	10	184.3	8.5	4.9
2000	35	142.3	18.3	1.8	2000	35	309.8	29.2	6.7	2000	35	195.1	10.7	5.8
2000	60	123.5	13.7	2.7	2000	60	133.5	28.8	2.4	2000	60	150.2	4.7	3.1

Table 4

Click here to download high resolution image

	AA2024-AA2024		AA7075-AA7075		AA2024-AA7075	
	F	**P**	**F**	**P**	**F**	**P**
Speed	28.05	0.000	5.02	0.019	2.92	0.080
Feed	22.05	0.000	6.21	0.009	0.30	0.747
Speed * Feed	10.76	0.000	2.63	0.069	2.96	0.048